



KIT SCIENTIFIC REPORTS 7707

# Annual Report 2014

Institute for Pulsed Power and Microwave Technology  
Institut für Hochleistungsimpuls- und Mikrowellentechnik

John Jelonnek (ed.)



John Jelonnek (ed.)

**Annual Report 2014**

Institute for Pulsed Power and Microwave Technology  
Institut für Hochleistungsimpuls- und Mikrowellentechnik

**Karlsruhe Institute of Technology**  
**KIT SCIENTIFIC REPORTS 7707**

# Annual Report 2014

Institute for Pulsed Power and Microwave Technology  
Institut für Hochleistungsimpuls- und Mikrowellentechnik

edited by  
John Jelonnek

## Report-Nr. KIT-SR 7707

Part of this work was supported by ITER Organization under the service contract No. ITER/CT/12/4300000720. The views and opinions expressed herein reflect only the author's views. The ITER Organization is not liable for any use that may be made of the information contained therein.

Part of this work, supported by the European Communities under the contract of association between EURATOM and KIT, was carried out within the framework of the European Fusion Development Agreement. Part of this work is supported by EFDA under Task WP13-IPH-A07-P1-01/KIT/PS, Task WP13-IPH-A11-P1-01/KIT/PS and Task WP13-PEX-P01+02+03b/KIT/PS.

Part of this work, supported by the European Communities under the contract of association between EURATOM and KIT, was carried out within the framework of the European Fusion Development Agreement. Part of this work is supported by Fusion for Energy under Grants F4E-GRT-432, GRT-315 and OPE-458 and within the European Gyrotron Consortium (EGYC). EGYC is a collaboration among CRPP, Switzerland; KIT, Germany; HELLAS, Greece; IFP-CNR, Italy. The views expressed in this publication do not necessarily reflect the views of the European Commission.

### Impressum



Karlsruher Institut für Technologie (KIT)  
KIT Scientific Publishing  
Straße am Forum 2  
D-76131 Karlsruhe

KIT Scientific Publishing is a registered trademark of Karlsruhe Institute of Technology. Reprint using the book cover is not allowed.

[www.ksp.kit.edu](http://www.ksp.kit.edu)



*This document – excluding the cover, pictures and graphs – is licensed under the Creative Commons Attribution-Share Alike 3.0 DE License (CC BY-SA 3.0 DE): <http://creativecommons.org/licenses/by-sa/3.0/de/>*



*The cover page is licensed under the Creative Commons Attribution-No Derivatives 3.0 DE License (CC BY-ND 3.0 DE): <http://creativecommons.org/licenses/by-nd/3.0/de/>*

Print on Demand 2015

ISSN 1869-9669

DOI: 10.5445/KSP/1000049502

# **Institute for Pulsed Power and Microwave Technology**

## **Institut für Hochleistungsimpuls- und Mikrowellentechnik (IHM)**

### **Director: Prof. Dr.-Ing. John Jelonnek**

The Institute for Pulsed Power and Microwave Technology (Institut für Hochleistungsimpuls- und Mikrowellentechnik (IHM)) is doing research in the areas of pulsed power and high power microwave technologies. Both, research and development of high power sources as well as related applications are in the focus. Applications for pulsed power technologies are ranging from material processing to bioelectrics. High power microwave technologies are focusing on RF sources (gyrotrons) for electron cyclotron resonance heating of magnetically confined plasmas and on applications for material processing at microwave frequencies.

IHM is doing research, development, academic education, and, in collaboration with the KIT Division IMA and industrial partners, the technology transfer. IHM is part of the Helmholtz Association (HGF). During ongoing HGF POF2 period (2009 – 2014), projects are running within following six HGF programs: Renewable Energies (EE), FUSION, NUKLEAR, NANOMIKRO, Efficient Energy Conversion and Use (REUN) and Technology-Innovation and Society (TIG).

During 2014, R&D work has been done in the following areas: fundamental theoretical and experimental research on the generation of intense electron beams, strong electromagnetic fields and their interaction with biomass, materials and plasmas; application of those methods in the areas of energy production through controlled thermonuclear fusion in magnetically confined plasmas, in material processing and in energy technology.

Mentioned research areas require additionally the profound knowledge on modern electron beam optics, vacuum technologies, material technologies, high voltage technologies and high voltage measurement techniques.

## Department for Pulsed Power Technologies:

*(Head: Prof. Dr.-Ing. Georg Müller)*

In environmental- and bio-technology the research and development is devoted to pulsed power technology with repetition rates up to 20 Hz, power in the Giga-Watt range and electric field strengths of  $10^5$ - $10^7$  V/m. The research is concerned with short pulse ( $\mu$ s) - and with ultra-short pulse (ns) treatment of biological cells (electroporation). The focus is related to large-scale applications, treatment of large volumes, to the realization of a high component life time and to the overall process integration. Main directions of the work are the electroporation of biological cells for extraction of cell contents (KEA process), the dewatering and drying of green biomass, the treatment of micro algae for further energetic use and sustainable reduction of bacteria in contaminated effluents. Another key research topic is related to the surface modification and corrosion protection of metals and alloys using high-energy, large-area pulsed electron beams (GESA process). The research is focused on electron beam physics, the interaction of electron beams with material surfaces and the corresponding investigations on material specific characterization. The goal is to develop a corrosion barrier for improved compatibility of structural nuclear reactor materials in contact with heavy liquid metal coolants (Pb or PbBi). In the field of fusion research the activities are dealing with experimental and theoretical studies on the plasma-wall interaction at the first wall and divertor of tokamak fusion reactors. Numerical codes (TOKES and MEMOS) are further developed, applied and validated for prediction of the impact of transients on the erosion and lifetime of plasma facing components (PFCs) with the goal to improve reactor design (Programs: EE, NUKLEAR, FUSION).

- The construction of the new out-door algae cultivation facility, called PBR1000, was completed in summer 2014. The primary objectives to be obtained with this installation are to produce sufficient biomass for pilot-scale PEF-processing and to optimize cultivation protocols with regard to improve process ability by pulsed electric fields aiming to lower energy demand and increased product extraction yields
- To study electrode abrasion as a function of pulse duration disk-shaped stainless steel electrodes, embedded into a polycarbonate continuous-flow cell were used within a CaCl<sub>2</sub>-electrolyte medium. It was found, that electrode erosion caused by PEF treatment does not increase with pulse duration, when specific energy input is kept constant.
- For parameter studies on the electroporation of plant cells a pulse source enabling a waveform generation within a wide parameter range is required. For this purpose a semiconductor-based Marx generator for the generation of bipolar pulses was designed. The design consists of a series connection of IGBT bridges, which can be controlled individually in order to generate a stepwise arbitrary waveform.
- Development of a new theoretical model to describe the whole electroporation phenomena has been started in collaboration with INRIA in Bordeaux and the IGR in Villejuif (both France). The model is based on classical electromagnetic equations for the electric aspects and phenomenological equations for the permeabilisation aspects. The main breakthrough of the model is that it separates the conductivity and the permeability of the membrane. The model still requires full calibration of all parameters. Preliminary studies confirm that such an approach can efficiently reproduce the experimentally observed behaviors finally (Program: EE, HGF-Portfolio BioEconomy).
- The aim of the joint IASS-KIT project on oxygen free methane reforming is to develop an experimental reactor for continuous hydrogen production by thermal decomposition of methane in liquid metals. In the past the principal feasibility of this process has been shown using lead (Pb) or tin (Sn) as heat transfer medium. However, at the desired temperatures (up to 950°C) the liquid metals contribute significantly to the corrosion of the reactor materials due to the high solubility of steel alloying elements.

Therefore material compatibility tests in liquid tin are one of the focus points of the work. At 900°C tungsten and graphite showed no attack, while a slight corrosion attack was visible at Mo. Based on these results a concept for a methane reactor using graphite as Sn contact material at the high temperatures and Mo as structural materials in the intermediate temperature range (< 550°C) was suggested.

- In the field of transmutation of long-living high-level radioactive waste from existing nuclear power reactors the institute's contribution is the development of a suitable corrosion protection especially for parts under high loads like fuel claddings or pump materials in contact with liquid Pb or PbBi. Pulsed large area electron beams (GESA) are used to modify the surface of steels such that they fulfil the requirements of their surrounding environment. Conditioning the liquid metals with regard to its oxygen concentration and the transport of oxygen are further tasks. All tasks are embedded in European and international projects like e.g. MATTER, SEARCH, ESNIIplus and MaTISSE. (Program: NUKLEAR).
- In the frame of different EFDA-tasks, a F4E-grant and an ITER Organization (IO) contract a variety of numerical simulations have been performed to support design activities for ITER and DEMO and experimental campaigns at JET. Analysis and computer simulation of disruption mitigation schemes of massive gas injection (MGI) have been done applying the numerical integrated tokamak code TOKES for 2-D and 3-D simulation of MIG radiation impact on first wall. MEMOS was further used to assist JET experiments in frame of the programs for ITER-like wall. Simulation results allowed reproducing of involved surface processes and the melt damage.
- Simulation of the mitigation efficiency of the run-away electron (RE) beam impact on the ITER first wall by special sacrificial W diaphragm has been performed using ENDEP, MEMOS and TOKES codes. The simulations have shown, that the 'nail' interaction with the RE beam of 300 MJ total energy results in severe wall melting close to the 'nail' with the melt depth up to 300 µm, which is fully intolerable. Performing a parametric study revealed that the wall surface starts melting if the RE beam energy exceeds 90 MJ for 10 ms time duration. (Program: FUSION).

## **Department for High Power Microwave Technologies:**

*(Head: Dr. Gerd Gantenbein)*

The Department for High Power Microwave Technologies is focusing on RF sources (gyrotrons) for electron cyclotron resonance heating and current drive (ECRH&CD) of magnetically confined nuclear fusion plasmas and on the application of microwaves to chemical processes, materials and composites.

- Collaboration within the W7-X project PMW for planning, construction and testing of the 10 MW CW, 140 GHz electron cyclotron resonance heating (ECRH) system for the stellarator W7-X at IPP Greifswald. In particular, the 1 MW CW, 140 GHz gyrotrons have been developed in cooperation with EPFL-CRPP Lausanne and Thales Electron Devices (TED), Vélizy, France. In 2014, SN2i and SN7i have been delivered to KIT for FAT tests. Both tubes have passed FAT at KIT and final SAT at IPP Greifswald. The tubes will be used for conditioning and startup of W7-X stellarator. The delivery and acceptance tests of the last series gyrotron is expected in 2015. The target for the finalization of the 10 MW ECRH system is 2015. The quasi-optical transmission system and the high-voltage modulators for the gyrotrons have been developed in cooperation with IGVP, University of Stuttgart.
- Within the European Gyrotron Consortium (EGYC) and in collaboration with its industrial partner Thales Electron Devices (TED), Vélizy, France, EGYC is developing gyrotrons for the International Thermonuclear Experimental Reactor (ITER). According to a change in the delivery strategy for ITER, Europe will

provide a total of 6 MW CW RF power at 170 GHz for the 24 MW CW ECRH system. Fusion for Energy (F4E) is coordinating the project. Institutional partners are CNR, Italy, EPFL-CRPP, Switzerland and HEL-LAS, Greece. In 2014, the procurement for the 1 MW 170 GHz short-pulse gyrotron has been completed. First experiments of this gyrotron have been performed end of 2014 at KIT showing key parameters of the ITER specifications.

- Despite the switch to the 1 MW conventional-cavity gyrotron for the first delivery of ITER, KIT is pushing forward the development of multi-MW (2 MW) coaxial-cavity gyrotrons in frame of EUROfusion and as prerequisite for future DEMO gyrotrons. In 2014, first experiments with depressed collector operation showed very promising results. The gyrotron has been operated in the 2 MW range with an efficiency of up to 48%.
- Future fusion experiments will require frequency step-tunable gyrotrons. A step-tunable 1 MW gyrotron (105-163 GHz), including a microwave vacuum window made of synthetic CVD-diamond for future ECRH systems of large-scale tokamak experiments was under test in 2014. Based on numerical simulations a high Q cavity was installed. The maximum efficiency achieved (non-depressed collector operation) was 38%, the maximum RF output power was 1.44 MW.
- KIT is in collaboration with EPFL-CRPP, Lausanne, to design a new (126 GHz / 84 GHz) dual-frequency 1 MW gyrotron based on design of ITER for TCV tokamak. In 2014, first physical designs for an innovative dual-frequency launcher concept and triode MIG have been completed.
- The test stand of the 10 kW / 28 GHz gyrotron has been completed in 2014. All relevant gyrotron components, including the first conventional cathode have been delivered, assembled and tested in cw operation. The tube has achieved a world record in efficiency for 2<sup>nd</sup> harmonic 28 GHz gyrotrons of 43% (non-depressed collector operation).
- In 2014, thermomechanical studies of high power gyrotron cavities and collectors have been performed in close collaboration with F4E and Politecnico Torino (POLITO) and in frame of master studies at KIT. New estimations on the heat transfer coefficient and the surface roughness coefficient, which are key parameters for the design of the cooling system, have been obtained.
- Quality of operation of the magnetron injection gun and secondary electron emission at e. g. the collector are of fundamental importance for gyrotron operation. Related possible efficiency degradation mechanisms in gyrotrons have been investigated: (i) a new theoretical model has been developed and implemented to simulate the effect of secondary electron emission at the collector or the components of the tube, (ii) measurements on current-voltage characteristics of a magnetron injection gun (MIG) has been introduced and analysed with respect to the average work function, temperature and standard deviation of the work function distribution of the emitter. First current measurements of a emission test device for verification of emitter uniformity have been performed with an existing W7-X gun in 2014.
- In frame of EUROfusion, KIT has continued its investigations on advanced gyrotrons for future DEMO. Target is the design of an 240 GHz gyrotron with frequency step-tunability and the possibility for operation at 170 GHz and 204 GHz additionally. In 2014 the design of coaxial cavity gyrotron and, alternatively, a conventional cavity gyrotron has been progressed. First studies on multi-staged depressed collectors which have the potential of significantly increasing the gyrotron efficiency have been started. Simulations have been launched on the use of ferromagnetic material to reduce peak power densities in gyrotron collectors, which might become of particular importance for multi-staged depressed collectors.

- In collaboration with the Federal University of Sao Carlos, Brazil systematic studies on microwave sintering of alumina-mullite composites were performed. Those materials are characterized by excellent chemical, physical and mechanical properties. The outcome of its low thermal expansion coefficient is high temperature stability and excellent thermal shock resistance.
- In the framework of a DAAD fellowship in collaboration with Alexandria University, Egypt systematic and comparative studies on microwave and conventional sintering of natural HA scaffolds were performed.
- A system for in-situ monitoring of the dielectric and the calorimetric properties during the microwave heating of materials at 2.45 GHz was developed and applied for dielectric characterization of materials like polymer composites, bone and hydroxylapatite samples in the 2,45 GHz range.
- Contributions have been given to the BMBF funded project MACOS which aims to develop a high power microwave applicator to speed up the decontamination of concrete surfaces from nuclear power plants.
- A compact high power microwave applicator was developed for the BMBF-funded DER Project which is coordinated by the TU Bergakademie Freiberg.
- The HEPHAISTOS technology has been further developed in frame of the BMBF funded project FLAME, which is coordinated by KIT. The main goal is to investigate the utilization of microwave heating for the production of fiber lightweight construction with its main focus on carbon fiber composites.
- In the frame of the Central Innovation Programm SME (ZIM) the potential of a thermo-selective microwave assisted gluing of textile leather to plastic base has been investigated.



# Contents

## General overview

Institute for Pulsed Power and Microwave Technology	
Institut für Hochleistungsimpuls- und Mikrowellentechnik (IHM) .....	i
Director: Prof. Dr.-Ing. John Jelonnek.....	i
Department for Pulsed Power Technologies: (Head: Prof. Dr.-Ing. Georg Müller).....	ii
Department for High Power Microwave Technologies: (Head: Dr. Gerd Gantenbein).....	iii
Contents.....	vii

<b>1</b>	<b>HGF Program: FUSION .....</b>	<b>1</b>
1.1	Plasma Wall Interaction (PWI) .....	1
1.2	Microwave Heating System for W7-X (PMW).....	7
1.2.1	Introduction .....	7
1.2.2	Series Gyrotrons for W7-X.....	8
1.2.3	Transmission Line System for W7-X .....	9
1.2.4	In-Vessel Components for W7-X.....	10
1.3	170 GHz, 1 MW CW Gyrotron Development for ITER .....	11
1.3.1	Introduction .....	11
1.3.2	Design and Operating Parameters.....	13
1.3.3	Short-Pulse Prototype.....	15
1.3.4	Experimental Results with Coaxial-Cavity Gun (CCG).....	16
1.3.5	Preliminary Results with Regular MIG .....	20
1.3.6	Summary on the initial short-pulse experiments .....	21
1.3.7	Beam-wave interaction modelling (F4E GRT-432, 553) .....	21
1.3.8	Quasi-optical mode converter and matching optical unit for the TE <sub>32,9</sub> -mode gyrotron .....	21
1.4	Frequency Step-Tunable Gyrotron Development for future ECCD Systems.....	24
1.4.1	Introduction .....	24
1.4.2	Experimental set-up.....	24
1.4.3	Numerical Simulation.....	26
1.4.4	Experimental Results .....	29
1.4.5	Conclusions .....	31
1.5	EUROfusion: Research and development towards a Gyrotron for future DEMO .....	31
1.5.1	Summary .....	31
1.5.2	Verification of the Coaxial-Cavity technology for DEMO .....	33
1.5.3	Towards a future 240 GHz Gyrotron for DEMO (WP HCD 4.2.3) .....	41
1.5.4	Studies on multi-stage collectors for fusion gyrotrons (WP HCD 4.3) .....	43
1.6	Emission uniformity test device for future MIGs.....	45
1.7	Advanced technologies for future high-power gyrotrons .....	47
1.7.1	Using ferromagnetic material to reduce power densities in collectors.....	47

1.7.2	Experimental investigations of a 20 kW / 28 GHz second harmonic CW gyrotron designed for evaluation of new emitter technologies .....	47
1.7.3	Thermo-mechanical studies of gyrotron cavities.....	50
1.7.4	Investigation on Secondary Electron Emission Models .....	51
1.7.5	Evaluation of Gyrotron Cathode Emission Inhomogeneity .....	51
1.8	FULGOR (Fusion Long-Pulse Gyrotron Laboratory).....	52
1.9	Launcher Handling and Testing facility LHT.....	53
<b>2</b>	<b>HGF Program: Energy, Topic Renewable Energy .....</b>	<b>56</b>
2.1	Overview .....	56
2.1.1	Construction and Operation of the new 1000 l photobioreactor “PBR1000” .....	56
2.1.2	Correlation between electrode erosion and pulse duration due to Pulsed Electric Field (PEF) treatment .....	58
2.1.3	Stimulation of algae growth by nanosecond pulsed electric fields .....	59
2.1.4	Measurements of the cellular membrane conductance reflect the dynamics and voltage dependence of electric-field-induced pore formation .....	62
2.1.5	New models to describe the electroporation phenomena .....	65
2.1.6	Study of the dynamics of the transmembrane voltage .....	66
2.1.7	Organization of the 2014 Bioelectrochemistry Gordon Research Seminar .....	67
2.1.8	Fast MOSFET-Based High-Voltage Switch for a Cable Pulse Generator .....	68
2.1.9	Modular Trigger Generator for Over-voltage Triggering of Marx Generators .....	68
2.1.10	Design of a semiconductor-based Marx generator .....	70
<b>3</b>	<b>HGF Program: Nuclear: Safety Research for Nuclear Reactors.....</b>	<b>72</b>
3.1	32-30-02 Cross Cutting activities .....	72
3.1.1	Corrosion and Wear Protection for New Reactor Technologies .....	72
3.1.2	Oxygen free methane reforming in liquid metals.....	72
3.1.3	GESA optimization - Metal Surface Layers after Pulsed Electron Beam Treatment.....	76
3.2	32-24-03 Transmutation – Liquid Metal Technology .....	78
3.2.1	Materials and oxygen transport and control in heavy liquid metal cooled subcritical systems (MYRRHA) .....	78
3.2.2	Erosion-tests of promising materials for liquid metal pumps (MATISSE).....	79
3.2.3	Manufacturing of MAXPHASE materials (MATISSE).....	80
3.2.4	Oxygen Transport in liquid metals (SEARCH) .....	82
3.2.5	Pressurized tube experiment (MATTER) .....	84
3.2.6	GESA Beam Dynamics.....	85
3.2.7	Optimization of FeCrAl to be used as corrosion barrier in liquid metals .....	87
<b>4</b>	<b>HGF Program: Rationelle Energieumwandlung und Nutzung (REUN) .....</b>	<b>90</b>
4.1	Dielectric Characterization, Concepts and Results.....	90
4.1.1	In-situ characterization and modelling of polymer composites curing .....	90
4.1.2	Dielectric characterization using the cavity perturbation method.....	91
4.1.3	In-situ monitoring of the dielectric and the calorimetric properties .....	92
4.2	Collaboration Projects.....	94
4.2.1	Dielectric study on microwave assisted desorption of soil.....	99

5	HGF Program: NANOMIKRO .....	100
5.1	Microwave synthesis and sintering of Mullite and Alumina-Mullite composites .....	100
5.2	Microwave sintering of Hydroxyapatite.....	101
	HGF Program: FUSION .....	102
	Publications at cross-referenced journals:.....	102
	HGF Program: NUSAFE.....	103
	Publications at cross-referenced journals:.....	103
	HGF Program: REUN .....	104
	Publications at cross-referenced journals:.....	104
	HGF Program: EE.....	104
	Publications at cross-referenced journals:.....	104
	HGF Program: NANOMIKRO .....	104
	Publications at cross-referenced journals:.....	104
	Appendix.....	106



# 1 HGF Program: FUSION

## 1.1 Plasma Wall Interaction (PWI)

The contract: JW14-TA-ANAL-01 with Fusion Consortium

The ITER Organization (IO) has recently decided to install a full-tungsten (W) divertor from the start of operations. One of the key issues with such a strategy is the possibility of W melting and melt splashing during transients, which can lead to modifications of surface topology and which may lead to higher disruption frequency or compromise subsequent plasma operation. Although every effort will be made to avoid leading edges, ITER plasma stored energies are sufficient that transients can drive shallow melting on the top surfaces of plasma-facing components (PFC). A new experiment has now been performed on JET in the new ITER-Like Wall (ILW) environment, in which a deliberately misaligned W element (lamella) in the outer divertor has been used to perform controlled ELM transient melting experiments for the first time in a tokamak.

Main application of MEMOS was regular assisting for the JET experiments in frame of the programs M13-01 and M13-02 for the ITER-like wall in which tungsten PFC surface melt motions under ELM impacts are under investigation. The MEMOS simulations allowed prompt estimations of the time intervals and heat loads needed for melting of the special lamella (Fig. 1.1.1) Simulation results allowed reproducing of involved surface processes and the melt damage for the surface temperature measured at the lamella leading edge. The modeling has been carried out for the JET H-mode reference discharge #84779 which supplied multiple input for MEMOS regarding ELMs heat loads of a frequency of 30 Hz. The obtained surface temperature dependent on time and evaporation rates are used for cross-checks of measurements. As one of the results, it has been shown that between MEMOS output and the measured parameters such as surface temperature good qualitative and quantitative agreements exist. Also the L-mode reference discharge #84514 was analyzed.

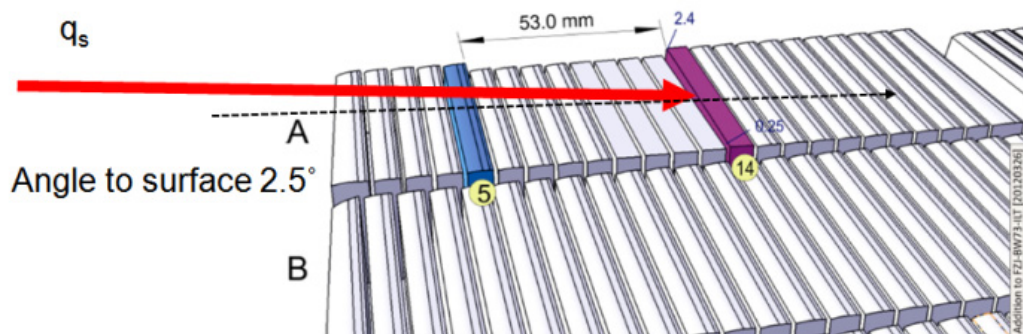


Fig. 1.1.1

The design of JET divertor lamellas used in MEMOS. The height of exposed edge of the special lamella (in magenta) is 2.4 mm.

Finally, simulations have been performed, for L-mode plasma loads without the complication of ELMs, and have been performed both for a reference, well aligned lamella and the misaligned element. Input heat loads are obtained from experimental data, notably high resolution infra-red (IR) thermography. During ELMing H-mode, the calculated time dependent, 3D temperature distributions in the special lamella lead

to extremely high temperature gradients at the leading edge ( $\sim 10^6$  K/m) and noticeable W evaporation. In fact, the simulations demonstrate that consistency with the measured IR temperatures is only possible if the impinging heat flux is a factor  $g_s \sim 2-4$  lower than expected from geometrical considerations (mitigation factor  $f_s = 1/g_s$ ). The code also indicates that shielding by the evaporated tungsten prevents bulk melting between ELMs. Encouragingly, the simulations are also able to quantitatively reproduce the dimensions of the damaged area observed by high resolution photography after the first pulse in which melting was achieved. The principle mechanism responsible for the melting is identified as the **JxB** force due to the thermo-emission currents from the hot surface, which generate velocities up to 0.7 m/s in the direction observed experimentally. No melt splashing is expected on the basis of the MEMOS simulations of melt depth and melt velocity and none is found experimentally. Comparison of the final calculated damage after H-mode reference discharge #84779 with experimental damage of the special lamella is shown in Fig. 1.1.2.

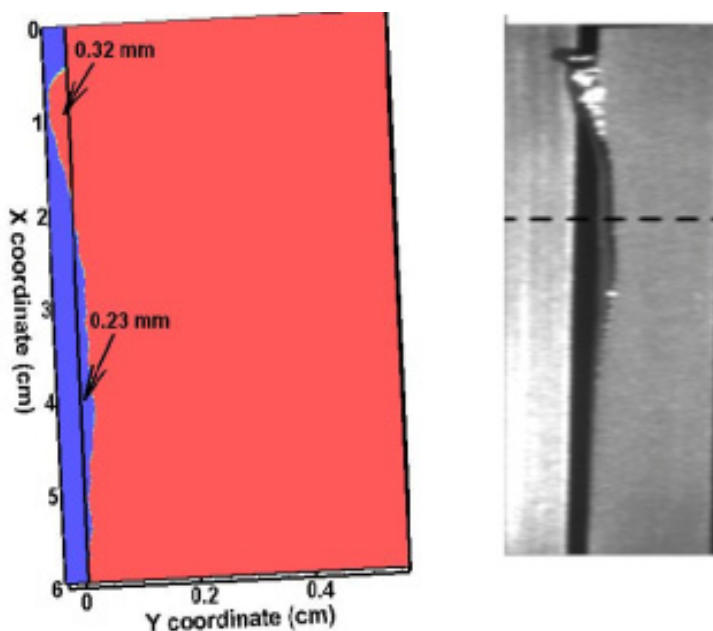


Fig. 1.1.2 Final calculated surface profile view from the top surface (Left) and view of Special Lamella damage (right).

The simulations for the shot JPN84779 with mitigation factor  $f_s = 0.4$  and accounting for the plasma shielding appropriately fit to the experimental data regarding time dependences of the surface temperature, measured vaporized tungsten and final damage of special lamella.

#### Contract with ITER organization WB# 4370007670

Analysis of importance of the **JxB** force generated by the thermo-emission current on melt layer damage of W monoblocks in the full-W divertor under ELM-like heat loads expected in ITER were performed using the code 3D MEMOS validated against JET-ILW experiments.

In case of strong magnetic field being parallel to the surface, thermo-emission electrons escaping from the surface can partly return back to the surface due to the gyro rotation around the magnetic field lines. That leads to additional decreasing the total thermo-emission current. Both mechanisms described above are important for ITER transient loads, in which impacting plasma heat loads impact rather large scale surfaces with relatively uniformly.

To demonstrate the suppression of melt motion caused by the  $\mathbf{J} \times \mathbf{B}$  force numerical simulations of ITER W monoblock damage under multiple ITER ELM-like heat loads are performed by the 3D MEMOS code. Absorbed energy density of ELMs at the monoblock surface was taken about  $1.1 \text{ MJ/m}^2$  with uniform energy distribution along the heated area. Simulations are carried out for the wide region of plasma pressures expected in ITER ELMs  $P = 0.02, 0.5$  and  $0.8$  bars. Triangle pulse shape of ELM is assumed with duration about  $0.7 \text{ ms}$  and  $0.35$  rise time. Overall impact angle of magnetic field lines at the top monoblock surface is about  $4.5$  degree. Depth of tungsten armour is taken about  $2 \text{ mm}$  with water cooling of W monoblocks from the back side. ELM frequency –  $5 \text{ Hz}$ ,  $B=2.65 \text{ T}$ . Due to negligible evaporation (about  $0.00067$  microns per each ELM) vapour shielding above the monoblock surface is not formed and tangential friction force of impacting plasma causes the melt motion. The simulations are performed for the target consisting of  $4 \times 4$  monoblocks (each monoblock has  $28 \text{ mm}$  in toroidal direction and  $12 \text{ mm}$  in poloidal, gap width –  $0.05 \text{ mm}$ , each monoblock has toroidal chamfer with chamfer height  $0.5 \text{ mm}$ ) geometry demonstrated on Fig. 1.1.3. Leading edges of monoblocks are shadowed.

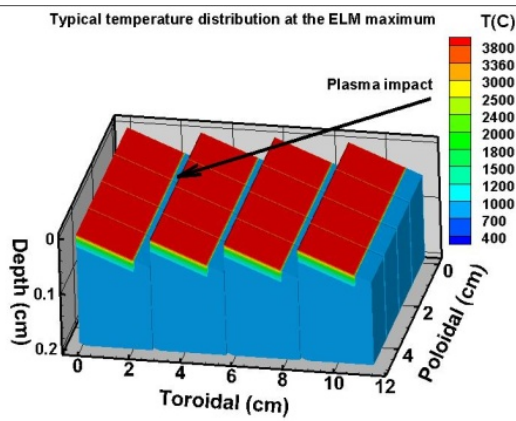


Fig. 1.1.3 Sketch of the tungsten target used in simulations of ITER multi ELMs impact scenario.

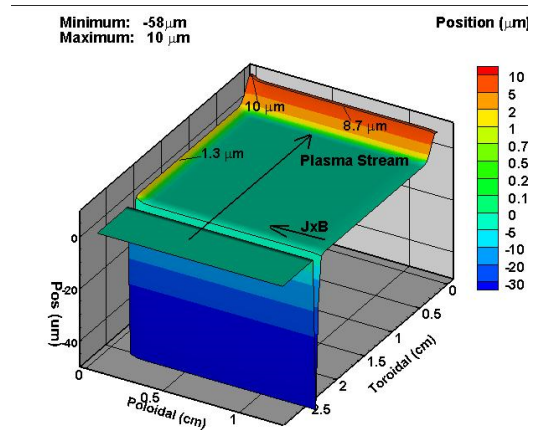


Fig. 1.1.4 Final erosion profile of single monoblock after 100 ELMs.  $P=0.02$  bars.

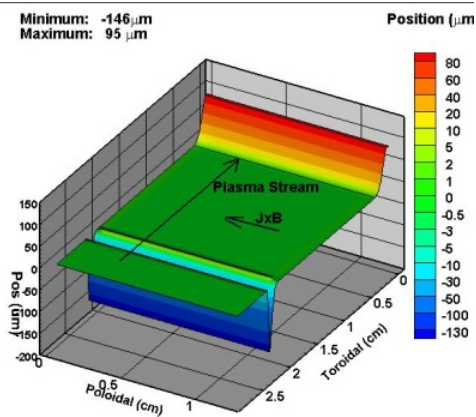


Fig. 1.1.5 Final erosion profile of single monoblock after 100 ELMs.  $P=0.5$  bars.

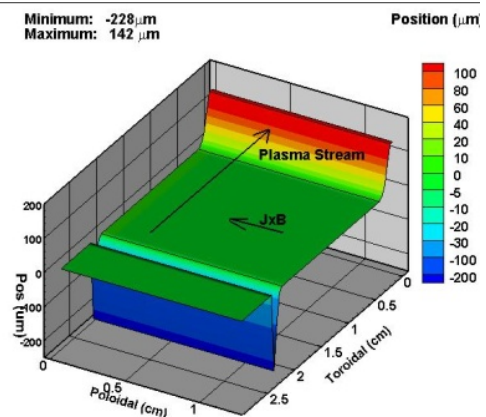


Fig. 1.1.6 Final erosion profile of single monoblock after 100 ELMs.  $P=0.8$  bars.

Final erosion profiles of single monoblocks after 100 ELMs are demonstrated on Fig. 1.1.4 for the scenario  $P=0.02$  bars, on Fig. 1.1.5 for the scenario  $P=0.5$  bars, and on Fig. 1.1.6 for the scenario  $P=0.8$  bars. For the calculated scenarios the melt layer thickness does not exceed 15 microns for each ELMs, the velocities of melt motion are below the critical velocities for droplet splashing and gap bridging. It is clearly seen that amplitude of surface damage in toroidal direction linearly depends on the pressure of impacting plasma respectively 10, 95 and 142 microns after 100 ELMs (0.1, 0.95 and 1.42 microns per single ELM). Erosion in the toroidal direction dominates and it is produced by the tangential friction force of the impacting plasma. Numerical simulations demonstrated that in the poloidal direction melt motion damage caused by the  $\mathbf{J \times B}$  force with Richardson thermo-emission current limited by the space charge is small (Fig. 1.1.4) and the  $\mathbf{J \times B}$  force produces negligible melt layer displacement in comparison with the melt layer damaged produced by the tangential friction force of the impacting plasma. After 100 ELMs erosion is about 1.3 microns (0.013 microns per ELM). It should be pointed out that the  $\mathbf{J \times B}$  force generated by thermo-emission current can lead to the noticeable melt motion damage of ITER tungsten armour in the regions with sharp temperature gradients (sharp heat load gradients). Influence of the  $\mathbf{J \times B}$  force on W armour erosion of ITER armour under transients with sharp heat load gradients has to be further numerically investigated.

**EFDA Task WP13-IPH-A07-P1-01/KIT/PS:** Analysis and computer simulation of disruption mitigation schemes of massive gas injection (MGI)

Massive injection of noble gas into the hot core of the tokamak before the disruption induces a sequence of physical processes, which would lead to the core cooling down by radiation, this mitigating the impact of the plasma to the first wall and to the divertor. Hence, the wall damage by disruptions in JET remains tolerable. To investigate the mitigation of the disruptive damage in ITER conditions a series of dedicated experiments on MGI has been performed in JET. Unfortunately, the JET diagnostics is not fitted for such short event as MGI with characteristic time duration of 1-10 ms. During the disruption caused by MGI the JET diagnostics is performing at the limit of its time resolution or even beyond the limit. However, cross-reference analysis of the available measurements combined with analysis of TOKES simulations allowed suggesting the MGI scenario. The scenario is the sequence of physical processes universal for all JET pulses analyzed. It provides the basis for the MGI scenario extrapolation to ITER.

Successful mitigation of ITER disruption requires irradiation of up to 90% of the discharge energy. However, the results of dedicated series of experiments in JET have revealed unexpected saturation of the radiated energy fraction at ~70-80% when the amount of injected Ar increased almost one order of the magnitude, from  $6.5 \cdot 10^{20}$  up to  $5.3 \cdot 10^{21}$  atoms. Analysis of the MGI physics performed in our group has revealed that the amount of NG in the saturation range is always enough to irradiate the thermal energy of electrons and the plasma current energy. Cross-reference analysis of experiments and simulations allows supposing that the thermal energy of ions cannot be converted into radiation because of very ineffective excitation of Ar ions by D ions and long equipartition time between D ions and electrons. The thermal energy of ions deposited not only onto divertor targets, but mainly on the first wall due to SSP roaming during CQ stage of MGI.

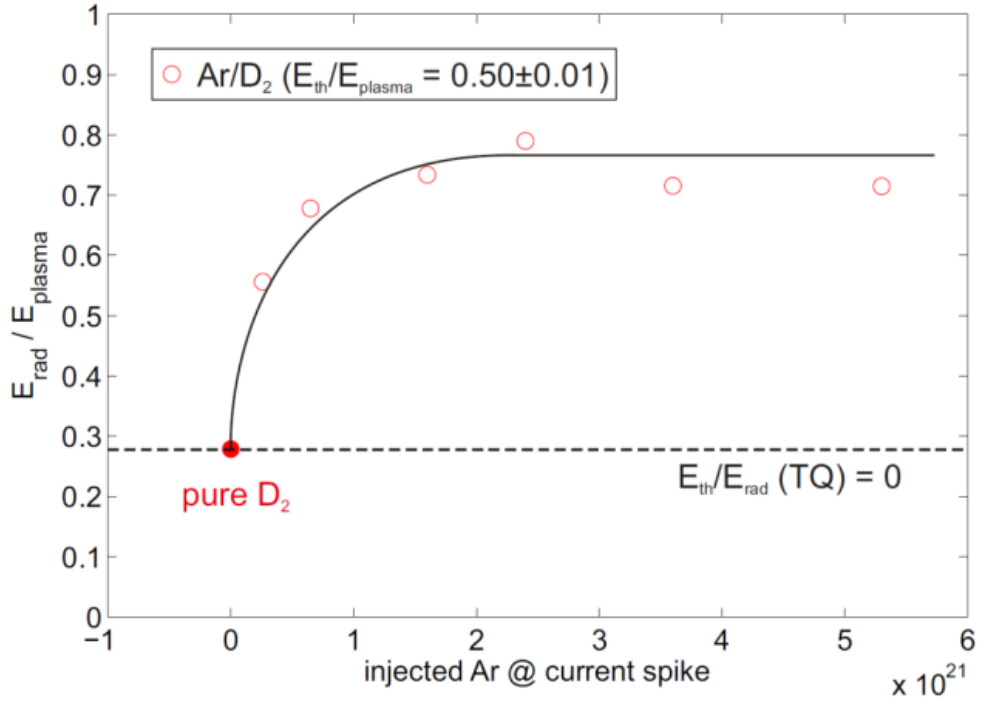


Fig. 1.1.7 Saturation of  $f_{rad}$  with the amount of injected Ar, measured in JET experiments.

One should mention again that JET diagnostics is not suited for measurements during MGI, so all the models, proposed for explanation of the MGI physics are based on indirect evidences or on the measurements performed at the limit of diagnostics validity. Unfortunately, there is no possibility to improve JET diagnostics to the level, which allows direct measurements for a final decision of this issue. The  $E_{rad}$  saturation at 75% could be a result of various factors, like decreasing of mixing efficiency with increasing of injected gas amount, cross-transport mechanisms saturation or radiation asymmetries, which can influence  $E_{rad}$  measurement. The proposed model explains all above mentioned experimental results:  $f_{rad}$  saturation at  $\sim 70\text{-}80\%$ , the dependence  $f_{rad}(E_{th}/(E_{th}+E_{mag}))$ , the  $W_{dia}(t)$  dependence measured in JET, but high electron temperature, suggested by this model contradicts with CQ time duration of 10 ms. An attempt to resolve this contradiction will be done in the future investigations.

Rough extrapolation of the result to ITER is straightforward: the minor radius of ITER is twice larger than that of JET. This results in slightly larger  $T_e$  in ITER core center comparing to the JET's one. As a result, the equipartition time in ITER  $\sim 6$  ms due to twice higher density and slightly larger  $T_e$ , so ion thermal energy can be radiated during  $\tau_{cQ} > 15$  ms.

An alternative approach for the disruption mitigation has been proposed. The discharge is cooled down with small amount of the noble gas and the RE generation is allowed. For mitigation of the RE beam impact on the tokamak wall a special sacrificial diaphragm, consisted of several tungsten 'nails' with 2 cm diameter, has been proposed. The 'nails' should be distributed poloidally and toroidally in a special way, but a simplest and non-optimal nails distribution is shown in Fig. 1.1.7. The nail height of 10 cm and the RE beam poloidal diameter of 1 m, results in the distance between nails less than 0.5 m in poloidal section, which resulted in 40 nails per section and for the toroidal asymmetry with  $n=1$ , as shown in Fig. 1.1.8, one should install the nails in 8 equidistant poloidal sections.

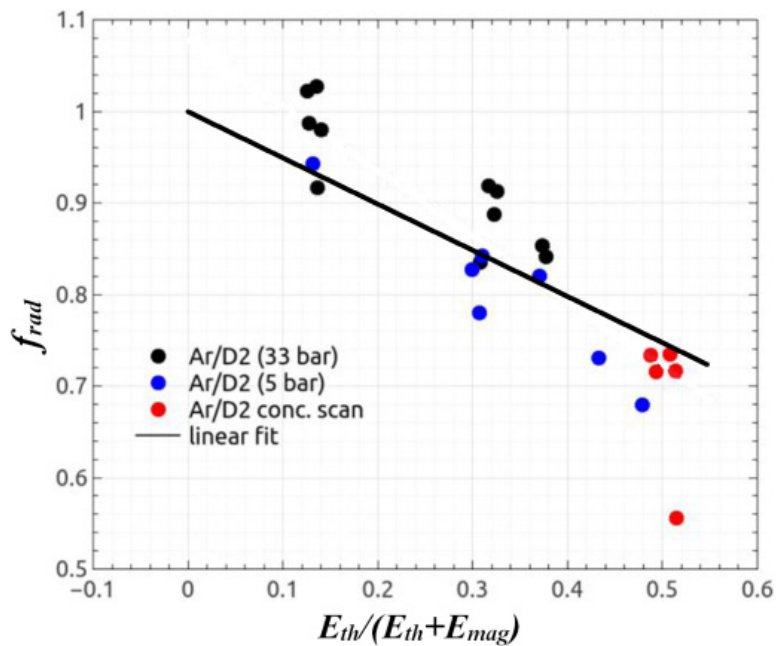


Fig. 1.1.8  $f_{rad}$  dependence of the  $E_{th}/(E_{th}+E_{mag})$  ratio measured in the dedicated series of experiments in JET. The measured dependence fits perfectly with the assumption energy that radiated are the electron thermal energy and the plasma current, but the ion thermal energy did not (black line).

Numerical simulation for the sacrificial diaphragm erosion under action of RE beams and mitigation of the heat load to the ITER first wall has been performed. The heat load mitigation is due to excluding direct contact of RE with the wall and the RE beam energy re-radiation by the W plasma shield. First of all the RE beam heats the 'nail' to the vaporization temperature and vaporizes small part of it. The vaporized material is ionized with the RE and after that the beam energy is deposited mainly to the plasma produced from the vaporized tungsten. As a result the RE beam energy is re-radiated with the plasma cloud onto larger wall area effectively reducing the wall heat load and erosion.

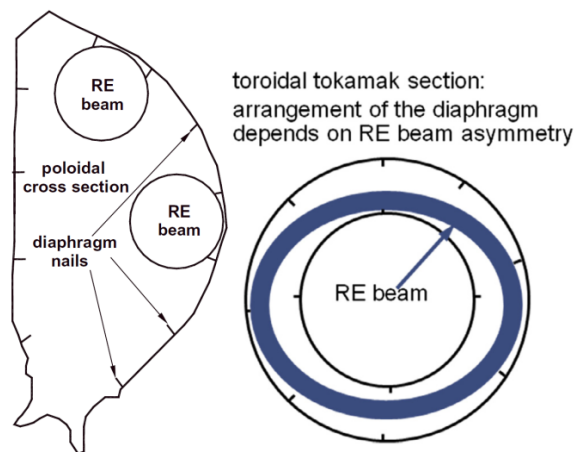


Fig. 1.1.9 Arrangement of the diaphragm protecting ITER wall from RE beam. Poloidal distance between 'nails' depends on RE beam diameter (left panel). It should ensure that RE nowhere touched the wall. Right panel shows toroidal ITER section through the midplane. Toroidal distance between 'nails' depends of the RE beam asymmetry.

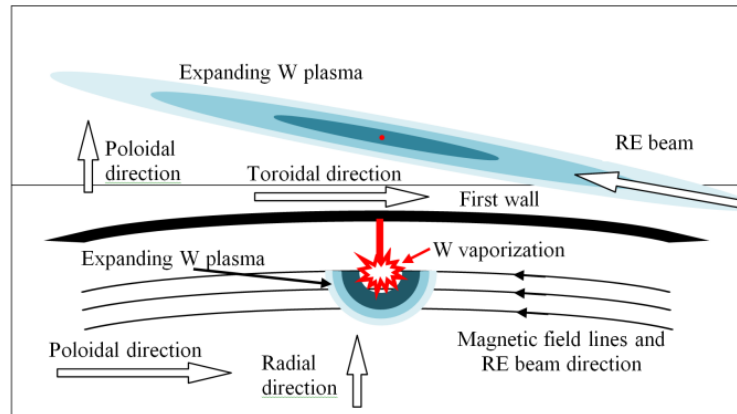


Fig. 1.1.10

W plasma expansion under action of heating by RE beam. Upper panel is the view from center to the outer wall, the point at the centre is the 'nail'. The W plasma cloud expands along the magnetic field line and diffuses across. The lower panel is the view in toroidal direction on the poloidal section crossing the 'nail'.

Simulation of the mitigation efficiency of the RE beam impact on the ITER first wall by special sacrificial W diaphragm has been performed using ENDEP, MEMOS and TOKES codes. The simulations performed have shown, that the 'nail' interaction with the RE beam of 300 MJ total energy results in severe wall melting close to the 'nail' with the melt depth up to 300  $\mu\text{m}$ , which is fully intolerable. Performing a parametric study, we have revealed that the wall surface starts melting if the RE beam energy exceeds 90 MJ for 10 ms time duration of the beam deposition. Lower RE beam energies are tolerable. During interaction with RE beam of threshold energy vaporized are  $\sim 20$  g of tungsten, that is  $\sim 6 \cdot 10^{22}$  W atoms – much less, than  $\sim 10^{26}$  Ne atoms, necessary for preventing RE generation.

#### Staff involved

Dr. B. Bazylev, Dr. Yu. Igitkhanov, Dr. I. Landman, Dr. S. Pestchanyi

## 1.2 Microwave Heating System for W7-X (PMW)

### 1.2.1 Introduction

Electron cyclotron resonance heating (ECRH) and current drive (ECCD) are the standard methods for localized heating and current drive in future fusion experiments the only CW heating methods available locate. Thus, ECRH will be the basic day-one heating system for the stellarator W7-X which is currently under final construction at IPP Greifswald. It is expected that the ECRH system for W7-X will be finalized in 2015. In its first stage W7-X will be equipped with a 10 MW ECRH system operating at 140 GHz in continuous wave (CW).

The complete ECRH system is coordinated by the project "Projekt Mikrowellenheizung für W7-X (PMW)". PMW has been established by KIT together with IPP and several EU partners in 1998. The responsibility of PMW covers the design, development, construction, installation and system tests of all components required for stationary plasma heating on site at IPP Greifswald. PMW coordinates the contribution from Institute of Interfacial Process Engineering and Plasma Technology (IGVP) of the University of Stuttgart too. IGVP is responsible for the microwave transmission system and part of the power supply (HV-system).

IPP Greifswald is responsible for the in-vessel components and for the in-house auxiliary systems. PMW benefits from the collaboration with Centre de Recherche de Physique des Plasmas (CRPP) Lausanne, Commissariat à l'Énergie Atomique (CEA), Cadarache and Thales Electron Devices (TED), Vélizy. A contract between CRPP Lausanne, FZK Karlsruhe and TED, Vélizy, had been settled to develop and build the series gyrotrons. First step in this collaboration was the development of a prototype gyrotron with an output power of 1 MW CW at 140 GHz.

Seven series gyrotrons have been ordered from the industrial partner Thales Electron Devices (TED), Vélizy. First operation and long pulse conditioning of these gyrotrons is being performed at the teststand at KIT. Pulses up to 180 s duration at full power are possible (factory acceptance test, FAT) whereas 30 minutes shots at full power are possible at IPP (necessary for site acceptance test, SAT). Including the pre-prototype tube, the prototype tube and the 140 GHz CPI-tube, in total 10 gyrotrons will be available for W7-X in final state. To operate these gyrotrons, in addition to the Oxford Instruments and Accel magnets, eight superconducting magnet systems have been manufactured at Cryomagnetics Inc., Oak Ridge, USA.

Most of the components of the transmission system, HV-systems and in-vessel-components have been ordered, manufactured, delivered and are ready for operation at IPP Greifswald. A part of the existing ECRH system has been already used to test new concepts and components for ECRH. A significant delay arose in the project due to unexpected difficulties in the production of the series gyrotrons.

### 1.2.2 Series Gyrotrons for W7-X

In 2005, the first TED series gyrotron SN1 had been tested successfully at FZK and IPP (920 kW/1800 s). It met all specifications during the acceptance test, no specific limitations were observed. In order to keep the warranty SN1 has been sealed, one prototype gyrotron is routinely used for experiments.

The series gyrotrons following SN1 did show a more or less different behavior with respect to parasitic oscillations excited in the beam tunnel region. These oscillations resulted in an excessive heating of the beam tunnel components, in particular of the absorbing ceramic rings. The gyrotrons re-opened after operation showed significant damages due to overheating at the ceramic rings and the brazing of the rings. A possible solution was proposed and successfully tested by KIT. As the main difference to the usual beam tunnel this design features corrugations in the copper rings which handicap the excitation of parasitic modes.

The thermal loading of the collector depends on the interaction efficiency between the electromagnetic field and the electron beam. And, of course, it depends on the pulse length. For high power operation at continuous wave (CW) the thermal loading is close to what is feasible in terms of cooling and lifetime of the collector. For the series tubes a patented sweeping procedure has been introduced which combines a vertical and radial displacement of the electron beam at the collector. This results in an almost constant power deposition at the inner wall along the axis and removes the particularly dangerous temperature peaks at the lower and upper reversal points of the electron beam.

Additional to the innovative collector sweeping, modifications have been realized and already tested in order to reduce the absorption of the internal stray radiation by covering stainless steel components with copper.

A possible corrosion in the water cooling circuit of the diamond window at the brazing structure is prevented by replacing the water by inert Silicon oil.

In 2014, the plan has been to achieve Factory acceptance (FAT) and Site Acceptance (SAT) of the series gyrotrons SN2i and SN7i. SN7 has been delivered in January 2013 already. Short pulse operation showed 1 MW output power with an expected efficiency of 30% without energy recovery at the collector. But, the measurement of the output beam quality showed a clear deviation from the specification which prevents the tube from long pulse operation. Low power RF measurements on a similar device and mechanical measurements confirmed a manufacturing failure of the internal surface of the quasi-optical mode transformer (launcher). The failure happened at the manufacturer of the launcher. Based on this, the complete gyrotron was taken back to TED for repair.

The series tube SN2i was delivered to KIT end of 2013, in January 2014 the gyrotron was prepared for the tests which started immediately. In short pulse operation ( $\sim$  ms) the tube showed a behavior similar to the previous tubes with an out put power of up to 1 MW. The output RF beam profile has been measured with an infrared system and analysed. Both, the Gaussian beam content as well as the central position of the beam at the output window are very good and well within the specifications. Long pulse conditioning of the tube has been performed with up to 1800 s operation at half of the nominal output power (500 kW) and up to 180 s operation at full output power (910 kW). The factory acceptance test was terminated and the tube was shipped to IPP for final site acceptance test with a pulse length of up to 1000 s and 950 kW. The maximum efficiency achieved was 40% including energy recovery by single stage depressed collector voltage.

After repair the series gyrotron SN7i has been delivered to KIT after summer 2014. The acceptance procedure demonstrated 1800 s pulse length at 500 kW output power and 180 s pulse length at 950 kW output power. The beam profile measurement showed 98% of Gaussian mode content. After acceptance of the tube it was shipped end of 2014 to IPP. The final acceptance tests are scheduled for early 2015.

### 1.2.3 Transmission Line System for W7-X

The transmission of the gyrotron power to the plasma is performed via an optical system, which consists of single-beam and multi-beam waveguide (MBWG) elements, in total more than 150 reflectors. For each gyrotron, a beam conditioning assembly of four mirrors is used to match the gyrotron output to a Gaussian beam with the correct beam parameters, and to set the appropriate polarization needed for optimum absorption in the plasma. A fifth mirror directs the beam to the beam combining optics, which is situated at the input plane of a multi-beam wave guide. This MBWG is designed to transmit up to seven beams (five 140 GHz beams, one 70 GHz beam, and one channel connected to the N-port remote-steering launchers via switches) from the gyrotron area (entrance plane) to the stellarator hall (exit plane). To transmit the power of all gyrotrons, two symmetrically arranged MBWGs are used. At the output planes of the MBWGs, two mirror arrays separate the beams again and distribute them via two other mirrors and CVD-diamond vacuum barrier windows to individually movable antennas (launchers) in the torus.

In 2014, the commissioning of the ECRH system is further advanced. The beam paths of several gyrotrons were aligned up to the towers; in this context, the imaging characteristics of the multi-beam transmission system (MBWG) could be confirmed also with high-power beams (Fig. 1.2.1).

Transmission tests over half the MBWG path were performed, showing tolerable, but higher losses than calculated, and higher than measured before. This issue needs to be resolved by further tests of the complete MBWGs.

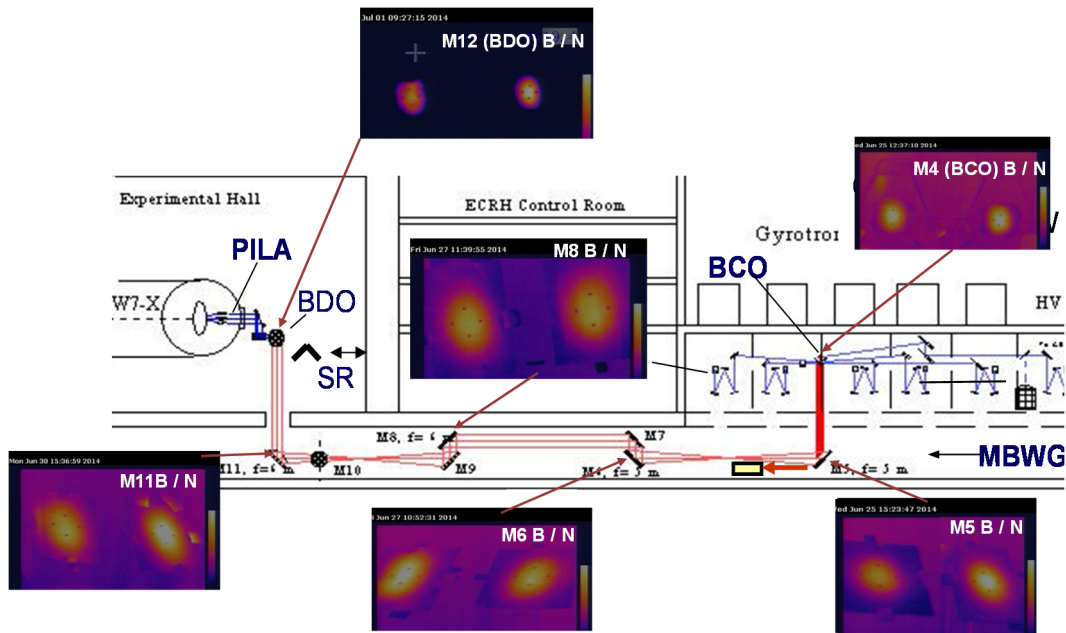


Fig. 1.2.1 Sketch of the multi-beam transmission system. The inserts show thermographic pictures obtained during the alignment of the mirrors on various mirror surfaces; they demonstrate the imaging characteristics of the multi-beam waveguide (Note that the wanted positions where the beams should hit the mirrors are marked with 4 dots in form of a cross).

Often, the commissioning work of gyrotrons and transmission system was hampered by arcing in the dummy loads, which initiated a new attempt for high-power load development. Meanwhile, the design of a prototype 1 MW CW load with Teflon tube absorbers is ready for construction.

For investigations of long-term stability of gyrotron/ mirror alignment, a high-power cw beam target has been manufactured. It is a homogeneously cooled plane mirror with a fast thermal response time that has no limit on the pulse length. It can be installed in the W7-X transmission line either on top or in lieu of a plane mirror or a polariser. Measurement of beam position is done with thermal imaging.

Ongoing is beam characterisation and the subsequent design and manufacturing of the surfaces of the matching mirrors for newly delivered gyrotrons; in 2014, these were the Thales tubes S2i and S7i. The newly designed mirrors incorporate power monitors which operate at two frequencies (104 and 140 GHz).

The receivers attributed to the directional couplers on the mirrors M14 are being installed at present. The alignment controls of the transmission lines using these coupler signals are finally assembled after the conical-scan mechanics and electronics had to be redesigned; commissioning is foreseen beginning 2015.

#### 1.2.4 In-Vessel Components for W7-X

The four huge front-steering launchers slipped collision-free into their narrow ports with a clearance of only several mm on their precisely aligned assembly rail system as shown in Fig. 1.2.2. Vacuum tightness of their Helicoflex flange connections could be achieved. The media connection and commissioning of the launcher are on-going. The launching geometry of the front steering mirrors has been proved inside the plasma vessel. The launching angles and the launch directions could be measured in the real geometry.

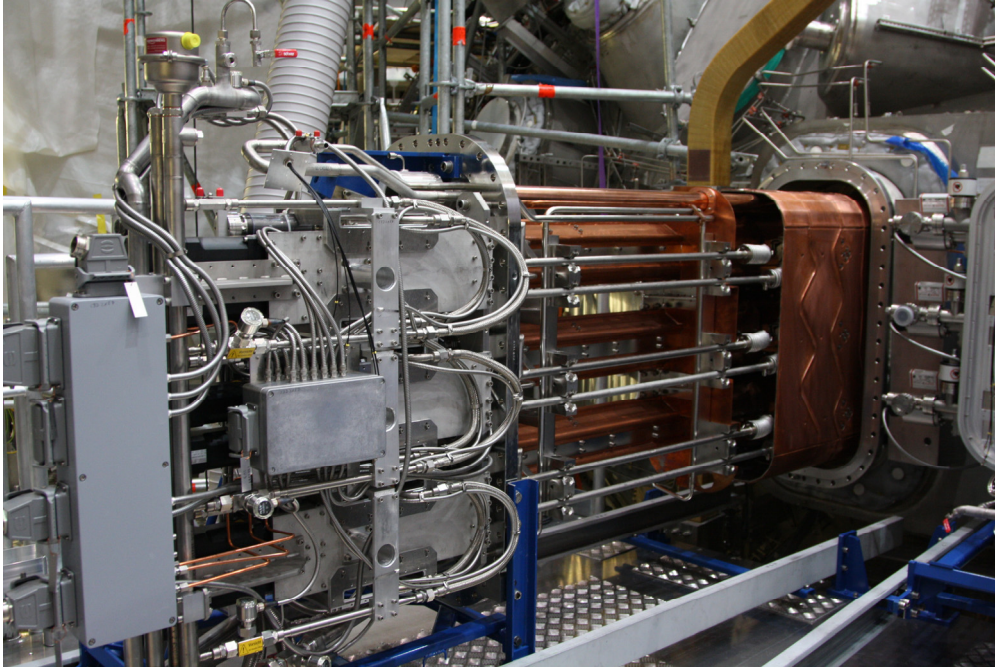


**Fig. 1.2.2**  
ECRH-launcher on rail system during slip-in into its W7-X port.

Opposite to the launcher on the inner wall heat shield specially shaped reflector tiles have been designed in order to reflect the non-absorbed part of the ECRH-beam a second time through the plasma center. The reflectors made out of the molybdenum alloy TZM will improve the heating efficiency in case of incomplete single pass absorption ECRH scenarios. These tiles are equipped with a holographic reflection grating and are presently manufactured by the IGVP-Stuttgart.

## **1.3 170 GHz, 1 MW CW Gyrotron Development for ITER**

### **1.3.1 Introduction**

The European Gyrotron Consortium (EGYC) together with its industrial partner Thales Electron Devices (TED), Vélizy-Villacoublay, France and F4E is presently developing the EU 170 GHz, 1 MWCW conventional-cavity gyrotron for heating and current drive (ECRH&CD) on ITER. The development was initiated in 2008 as a risk mitigation action during the development of the 2 MW coaxial-cavity gyrotron for ITER. Since then, preliminary designs of the cavity and the MIG have been reported.

The technological design of the 1 MW gyrotron is as similar as possible to the 1 MW, 140 GHz CW gyrotron for Wendelstein W7-X, Greifswald making use of the strong experience gained during the series production of several industrial tubes. Same is valid for the principal scientific design. However, the knowledge and understanding gained during the development of the coaxial-cavity gyrotron were taken into account also for the design improvements of several subcomponents. More details about the scientific design and the operating parameters of the tube are presented in next section.

Based on the project strategy developed by F4E, two prototypes are foreseen: (i) a single CW industrial prototype intended to reach the ITER requirements in terms of output power, efficiency, RF beam quality and pulse length, and (ii) a modular SP prototype intended to validate the design of the main gyrotron components in pulse length of few milliseconds.

The CW prototype is under manufacturing and the delivery is planned for 2015. The first phase of RF tests will be performed with the existing Oxford Instrument (OI) super-conducting magnet (SCM) at the KIT gyrotron test stand by the end of 2015 with a pulse length limited to 3 min due to high voltage power supply. In parallel, a new liquid Helium-free (LHF) SCM will be procured and delivered to the EU gyrotron test stand at EPFL-CRPP. Tests on the 1 MW, CW prototype will be extended to CW operation at EPFL-CRPP.

The fabrication of the components of the SP prototype has been completed and some preliminary experiments have been performed in 2014 with the use of an existing coaxial-cavity MIG and a modified anode available at KIT.

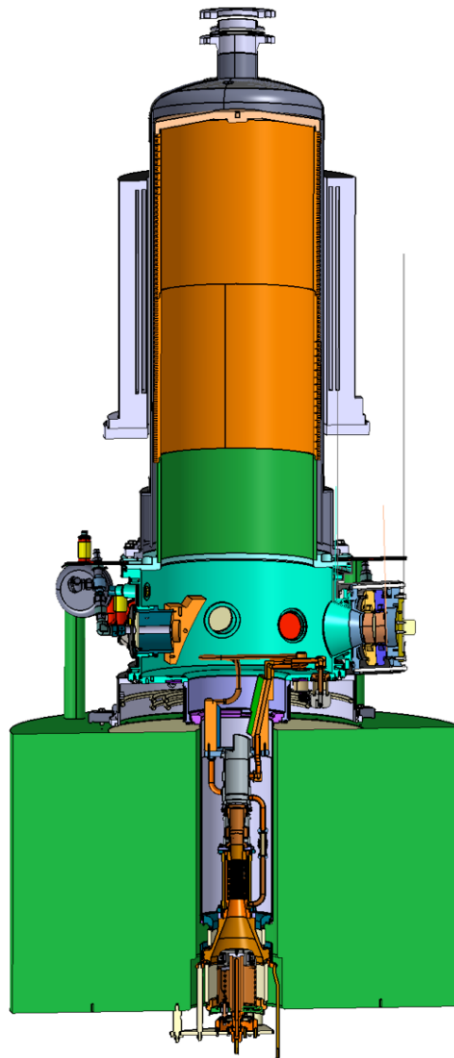


Fig. 1.3.1  
Three-dimensional view of CW prototype.

<i>Parameters</i>	<i>Nominal</i>	<i>Low Voltage</i>
<i>Operating Cavity Mode</i>	<i>TE<sub>32,9</sub></i>	
<i>Magnetic Field B<sub>0</sub></i>	<i>6.78 T</i>	<i>6.69 T</i>
<i>Beam Voltage V<sub>b</sub></i>	<i>80 kV</i>	<i>70 kV</i>
<i>Deceleration Voltage V<sub>d</sub></i>	<i>35 kV</i>	
<i>Beam Current I<sub>b</sub></i>	<i>40 A</i>	<i>45 A</i>
<i>Beam Radius R<sub>b</sub></i>	<i>9.44 mm</i>	
<i>Pitch Angle α</i>	<i>1.3</i>	<i>1.2</i>

Table 1.3.1

### 1.3.2 Design and Operating Parameters

A three dimensional view of the CW prototype is shown in Fig. 1.3.1. The key components of the gyrotron are as follows: (i) the MIG where the electron beam is generated, (ii) the beam-tunnel to suppress any parasitic oscillation which could be excited between MIG and cavity, (iii) the cavity in which the interaction takes place, (iv) the quasi-optical system (QOS) which converts the nominal operating mode into the linearly polarized fundamental Gaussian-like free-space mode, and finally the single stage depressed collector (SDC), which gathers the spent beam electrons. More details about the design of the key components of the gyrotron.

The nominal operating parameters of the gyrotron are given in Table 1.3.1. The operation of the gyrotron with a low voltage operating point was also investigated to explore the capabilities of the power supply specifications of ITER (see also Table 1.3.1). For both operating points, the expected gyrotron performance satisfies ITER criteria as shown in Table 1.3.2.

The efficient operation of the gyrotron at both operating points is possible due to the flexibility of the Oxford Instruments (OI) SCM available at KIT. The currents of the SCM coils are supplied by three independent power supplies (PS). This advantage provides the flexibility to generate magnetic field profiles with the following characteristics: (i) the appropriate value for the magnetic field at the cavity, shown in Table 1.3.1, (ii) the appropriate magnetic compression, in order to ensure that the electron beam radius at the cavity has the specified value, as it is also shown in Table 1, and (iii) a large range of the magnetic field angles  $\phi_B$  at the emitter and hence flexibility to adjust the average pitch angle  $\alpha$  of the beam at the cavity.

<i>Output Power at RF Window</i>	<i>1MW</i>
<i>Operating Frequency (Cold Cavity)</i>	<i>170.23 GHz</i>
<i>Gaussian Mode Content</i>	<i>98.6%</i>
<i>Interaction Efficiency</i>	<i>35%</i>
<i>Overall Efficiency w/o SDC</i>	<i>32%</i>
<i>Overall Efficiency with SDC</i>	<i>&gt;50%</i>
<i>Internal Losses (IL, including stray radiation)</i>	<i>10.5%</i>
<i>Stray Radiation</i>	<i>&lt; 2.4%</i>

Table 1.3.2

The magnetic field angle  $\varphi_B$  is a very important operating parameter due to the fact that it is the only way to adjust the pitch angle when a diode gun is used, as it is the case for the 1 MW EU gyrotron, while keeping constant all other operating parameters, such as the magnetic field at the cavity, the beam radius and the voltage. In particular, the pitch angle is affected by the variation of the magnetic field angle due to the fact that the initial transverse velocity  $v_t$  of the electron trajectories depends on the cross product  $\mathbf{E} \times \mathbf{B}$  of the electric  $\mathbf{E}$  and magnetic  $\mathbf{B}$  fields on the surface of the emitter ring. A variation of more than  $8^\circ$  of  $\varphi_B$  is possible with the OI-SCM, keeping the appropriate values for the magnetic field at the cavity and the magnetic compression. This range ensures a significant adjustment range for the pitch angle of the order of  $\Delta\alpha \sim 1$ , while the spread remains low (smaller than 3%) for all cases. However the laminarity of the beam is also affected by the variations of  $\varphi_B$ , as shown in Fig. 1.3.2. For negative values, the beam is non-laminar, for positive values the beam is laminar, while for the nominal value  $\varphi_B = 0$  the shape of the beam is at the boundary of the two states.

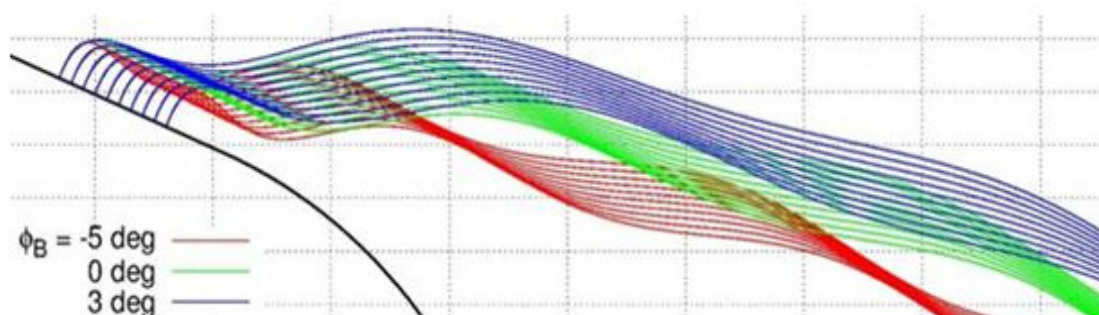


Fig. 1.3.2  
Beam trajectories for several magnetic field angles at the emitter ring region.

An additional parameter which should be taken into account in the gyrotron design and operation is the depression voltage at the cavity due to the space charge of the electron beam which in the cylindrical cavity gyrotron could have a significant value. The depression voltage for the EU gyrotron for ITER is of the order of 10% of the accelerating voltage. The MIG is optimized considering the possibility full CW neutralization conditions, i.e. beam voltage is equal to the accelerating voltage. For the operation of the gyrotron in SP conditions a higher accelerating voltage is required for the compensation of the depression voltage. The pitch angle, also in this case, is adjusted with the magnetic field angle  $\varphi_B$  variation.

### 1.3.3 Short-Pulse Prototype

In order to validate the design of the key components of the CW gyrotron, a SP prototype has been manufactured at KIT. TED is the sub-contractor for the manufacturing of the MIG. The physical design of the key components is identical to the CW prototype. However, the construction of the tube is significantly simpler. In particular, the sub-components are assembled using flanges in order to ensure modularity, and the cooling is limited to the electron gun and to the collector with the purpose of keeping the duty cycle as high as possible. A three-dimensional view of the short pulse prototype is shown in the next figure on the left side. All subcomponents have been manufactured and assembled in 2014.

Before the delivery of the nominal electron gun, it was decided to perform some preliminary experiments with an existing electron gun available at KIT. The coaxial cavity gyrotron (CCG) MIG of the modular SP gyrotron was used for this purpose. The anode of this gun had to be redesigned in order to generate the appropriate beam parameters at the cavity and to adapt the MIG to the appropriate flange of the SP prototype.

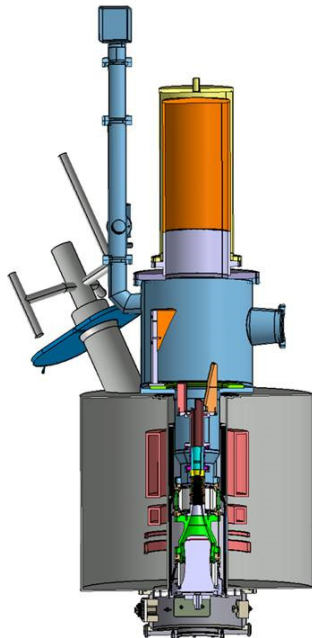


Fig. 1.3.3  
Three-dimensional view of SP prototype.



Fig. 1.3.4  
The short pulse prototype assembly with the CCG-MIG.

It should be mentioned that the CCG-MIG is not ideal for the operation of the 1 MW gyrotron: (i) the beam quality is significantly lower than that of the nominal MIG, in particular, the velocity spread of the electron beam is two to three times higher, and (ii) the criteria to suppress the electron trapping mechanisms are not satisfied. In addition, the operation of the gyrotron with depressed collector is not feasible using the CCG-MIG due to technical limitations. In particular, the size of the CCG-MIG is too big and it is not possible to connect the anode with the power supply due to the limited space in the warm bore hole of the OI-SCM. This will not be the case for the nominal MIG which is much smaller than the CCG-MIG.

The purpose of experiments using this non optimal MIG, were: (i) preliminary validation of the design of the cavity and the QOS, (ii) detect possible parasitic oscillation in the beam tunnel region, (iii) measurements of stray radiation losses, and, (iv) comparison of the gyrotron operation with the two different (non-optimal and optimized) guns.

The gyrotron subcomponents were cleaned and the whole gyrotron was assembled. A picture of the SP prototype is given in Fig. 1.3.4. The achieved background vacuum after the operation of the ion getter pumps was of the order of  $10^{-9}$  mbar.

The voltage standoff capability of the tube was tested using a high impedance HV power supply. Without magnetic field, the voltage standoff was very good for voltages below 100 kV. However, some discharges/instabilities were observed for voltages more than 80 kV when the nominal magnetic field was present. This behavior of the tube was expected due to the fact that a deep potential well is formed at the rear part of the CCG-MIG at the presence of the magnetic field. This is not the case with the optimized MIG.

### 1.3.4 Experimental Results with Coaxial-Cavity Gun (CCG)

After a short conditioning period, oscillation at the nominal  $TE_{32,9}$  mode was realized. The frequency of the output RF beam was measured as 170 GHz. Extrapolating this result to the CW tube and taking into account the thermal expansion of the cavity, the expected frequency of the CW tube will lie in the ITER specification  $170 \pm 0.3$  GHz. The pulse length was generally kept at the level of half of a millisecond due to the low level of conditioning of the tube. A significant influence on the pressure in the tube during the pulse was observed. In particular, the pressure rises from  $10^{-9}$  mbar at the beginning of the pulse to more than  $10^{-6}$  mbar at 2 ms pulse length. This issue will be addressed in the second phase of the experiments when the gyrotron will be assembled with the nominal MIG, with the aim of reaching pulse lengths of a few ms. The optimal position of the electron beam at the cavity was investigated by using the x- and y-axis alignment system available in the OI-SCM. It consists of six dipole coils, three for each axis, in order to transversely displace the electron beam at the cavity in a controlled way. Two current power supplies are connected with the dipole coils, one for each direction. The transverse displacement of the electron beam is estimated as  $40 \mu\text{m}/\text{A}$ , with a maximal current of 20 A for each direction. In other words, a displacement of the beam of the order of  $\pm 0.8$  mm could be corrected by this system. However, the perturbation of the magnetic field of this system could have some influence on the beam quality. This issue has not been investigated yet.

The criterion used for the optimization of the electron beam position at the cavity was the maximization of the voltage for which the nominal mode remains stable. The maximal voltage is affected by the currents applied on the dipole coils as it is shown in Fig. 1.3.5. The optimal output power is also achieved at the position where the maximum voltage has the highest value. The corresponding currents are  $I_x = -8$  A and  $I_y = 2$  A for the x- and y- dipole coils respectively, which corresponds to a beam misalignment of about

0.33 mm. It should be noted that, despite the probable electron beam quality degradation due to the magnetic field of the dipole coils, the output power remains relatively unaffected for beam displacements of the order of  $\pm 0.3$  mm.

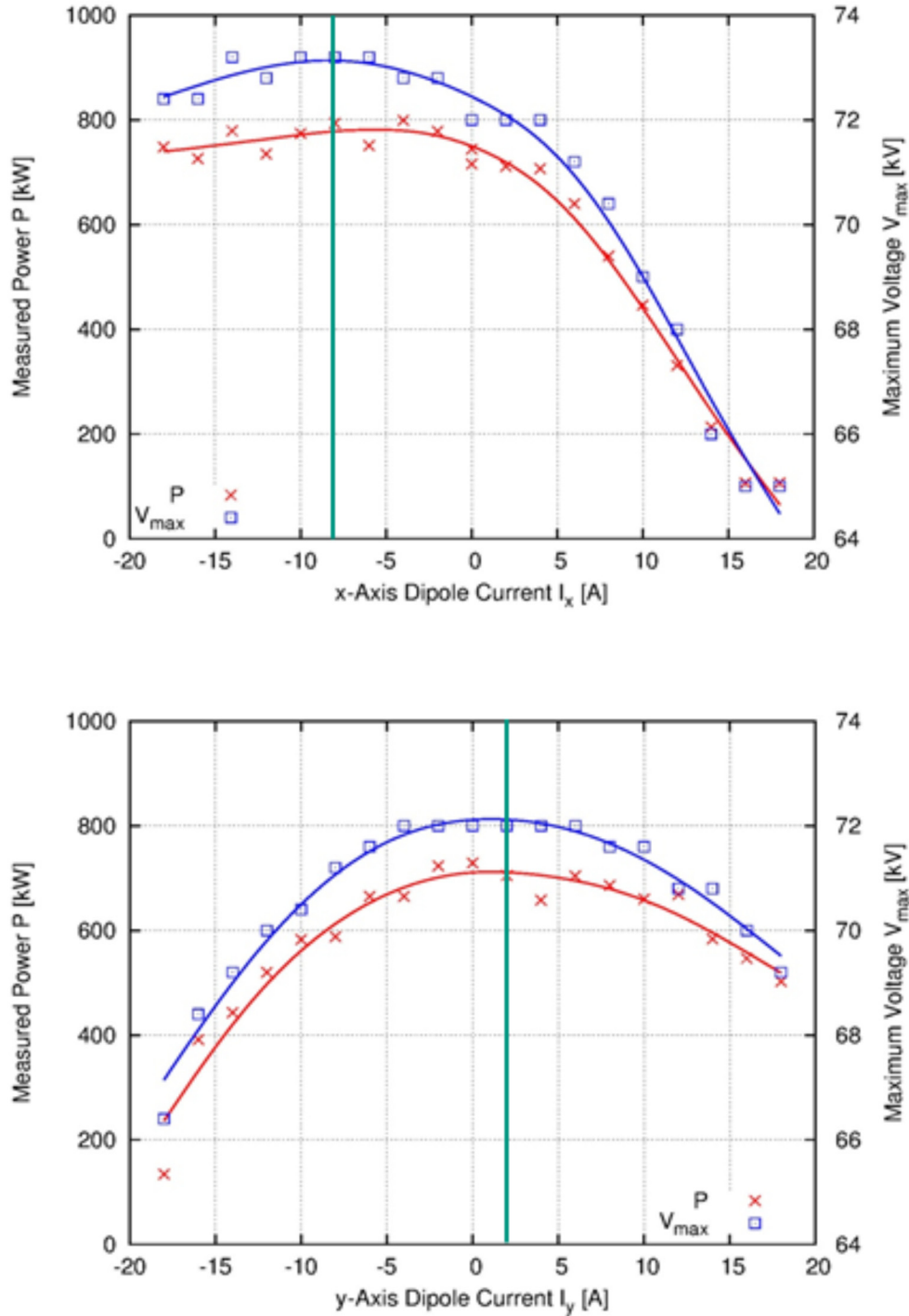
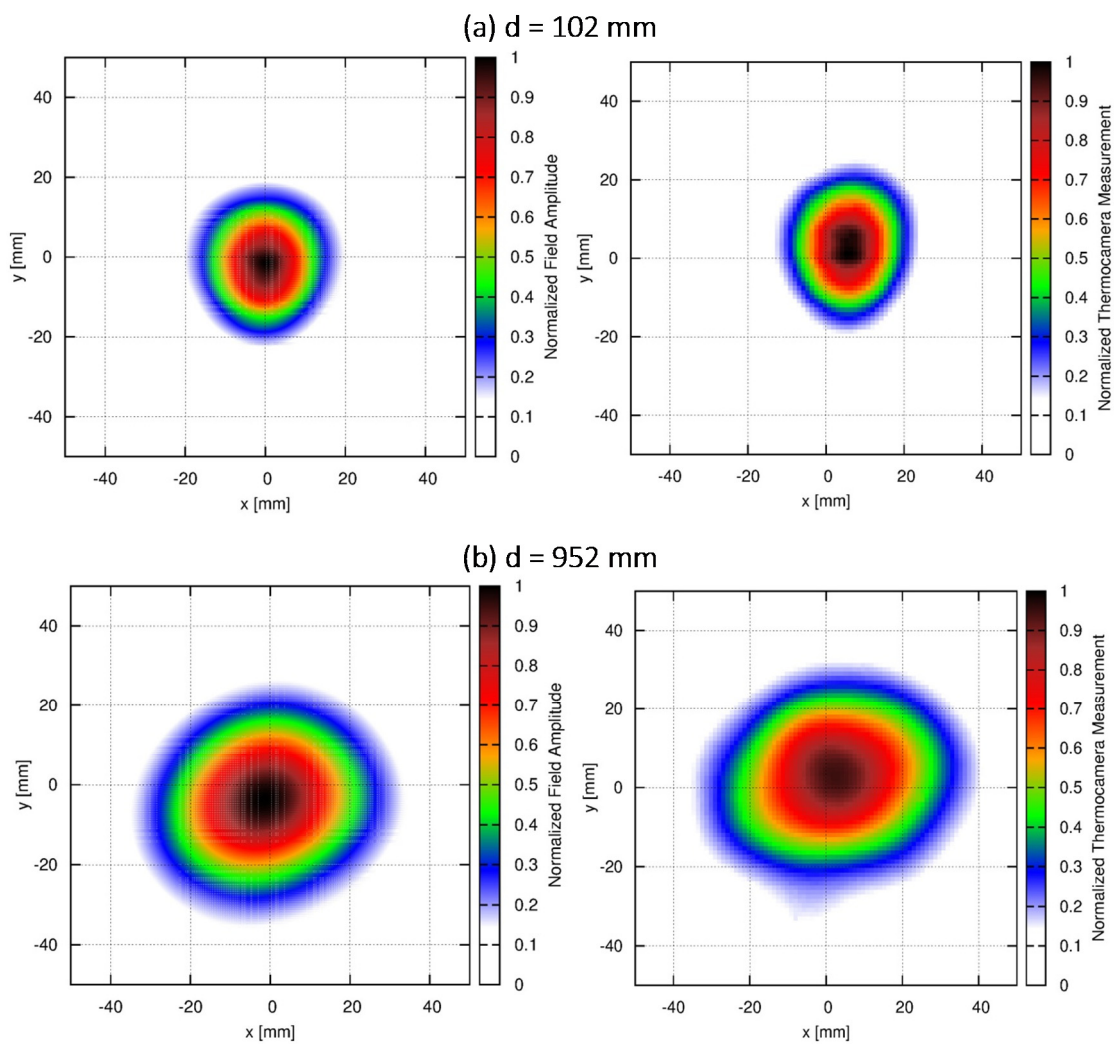


Fig. 1.3.5 Maximum voltage for which the nominal mode remains stable (blue squares) and the power (red crosses) versus the x- and y- dipole currents of the SCM.

The profile of the output mm-wave beam was also experimentally measured using an infrared camera recording the temperature elevation of a target placed in the beam path, within several distances away from the output window. A comparison of the experimental with the theoretical profile is shown Fig. 1.3.6 for two different positions of the target. The Gaussian mode content is estimated as 96.5%, which fulfills the ITER criterion, while the theoretical value is 98.6%. This discrepancy can be explained by the fact that the frequency of the RF beam in SP operation is 170 GHz, slightly higher than the 170 GHz where the operation of the QOS is optimized. The stray radiation losses were also measured using a ballistic calorimeter and a bolometer attached to the two relief windows placed on the mirror box. The stray radiation losses are estimated to be 3.5%. However, the uncertainty of this measurement is quite large since for more accurate measurements a longer pulse length (of several milliseconds) is necessary. More accurate measurements of the stray radiation losses will be performed with the nominal MIG assembly.



**Fig. 1.3.6**  
A comparison of the theoretical (left) and the experimental (right) beam profile at distances of 102 mm (a) and 952mm (b) from the window.

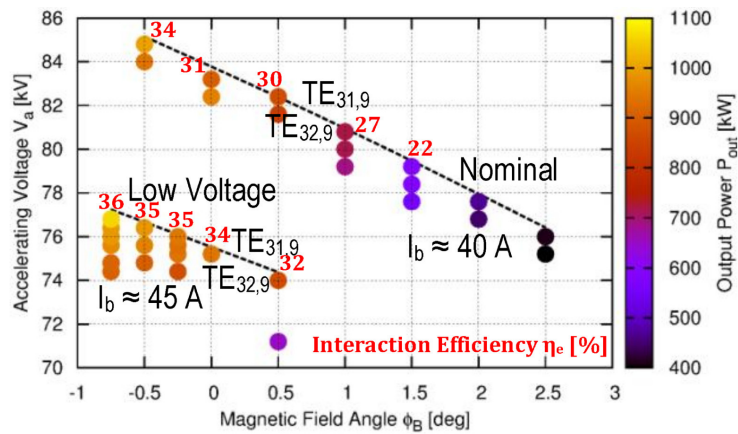


Fig. 1.3.7 Gyrotron stability region for operation on the nominal and low voltage operation points, as a function of the angle between the magnetic field line and the emitter. The color scale gives the corresponding output power and the numbers in red the efficiency.

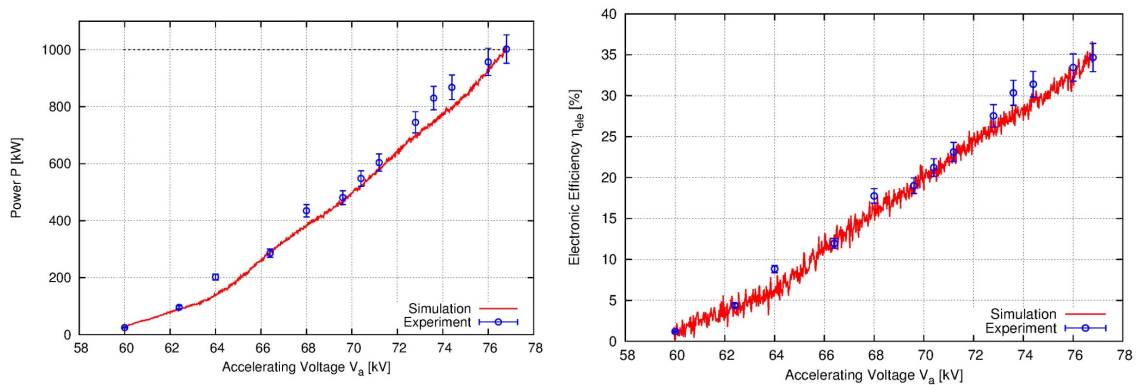


Fig. 1.3.8 Comparison of theoretical and experimental results of output power and efficiency versus the accelerating voltage.

It should be noted that no parasitic oscillation was observed during the gyrotron tests for many sets of operating parameters. This fact constitutes a short pulse experimental validation of the beam-tunnel design.

The stability of the nominal mode  $TE_{32,9}$  versus the main competitor  $TE_{31,9}$  was experimentally studied for several values of the magnetic field angle at the emitter. The stability regions for the nominal and the low voltage operating points are shown in Fig. 1.3.7. The dashed lines represent the maximum voltage at which the nominal mode is excited versus the magnetic field angle at the emitter. Each dot corresponds to a pulse; the colors of the dot indicate the output power, while the interaction efficiency, estimated for selected points, is noted in red. For the estimation of the interaction efficiency 10% internal losses and the simulated voltage depression were considered. An output power in excess of 1 MW was achieved for both operating points while the interaction efficiency was higher than 30%, in agreement with the simulated theoretical values (see the table before). From this one can expect an efficiency of 50% if operation with the nominal electron gun in depressed regime is possible.

A comparison of the theoretical and experimental results of output power and efficiency versus the accelerating voltage is shown in the second figure on page 19. The low voltage operation was performed with a magnetic field angle at the emitter of  $\varphi_B = -0.5$  deg. The *Ariadne* code was used for the calculation of the beam parameters at the cavity, while the *EURIDICE* code was used for the estimation of the output power and interaction efficiency (10% internal losses and the simulated voltage depression were also considered). As it is shown in Fig. 1.3.8, the theoretical and experimental results are in excellent agreement.

<i>Pulse</i>	<i>V<sub>a</sub> [kV]</i>	<i>I<sub>b</sub> [A]</i>	<i>P<sub>o</sub> [kW]</i>	<i>η<sub>e</sub> [%]</i>
<i>#383</i>	<i>75.6</i>	<i>50.7</i>	<i>1046</i>	<i>33</i>
<i>#385</i>	<i>77.2</i>	<i>62.0</i>	<i>1192</i>	<i>30</i>
<i>#386</i>	<i>78</i>	<i>64.0</i>	<i>1291</i>	<i>31</i>
<i>#387</i>	<i>78.8</i>	<i>67.0</i>	<i>1313</i>	<i>30</i>

**Table 1.3.3**

Finally, it should be also mentioned that the operational margin of the gyrotron was briefly studied, by increasing the beam current and/or the accelerating voltage, starting from the low voltage operation point. Very stable operation was observed even for operating parameters significantly higher than the nominal ones, such as shown in **Table 1.3.3**, where the output power and the interaction efficiency of several cases are presented. It is impressive that the output power has reached values higher than 1.3 MW with a reasonable electronic efficiency.

### 1.3.5 Preliminary Results with Regular MIG

The regular electron gun has been provided by THALES end of October and was immediately installed in the gyrotron. The tube has been cleaned, pumped, preliminarily conditioned using heating wires and prepared for the FAT (Factory Acceptance Test). First emission of electrons from the emitter has been observed end of November. Other requirements related to the FAT, mainly related to the HV Stand-off conditions, have been fulfilled end of November. Finally, the FAT took place on 2<sup>nd</sup> and 3<sup>rd</sup> of December at the final end of 2014 in presence of F4E officials. Unfortunately, further experiments with the new “regular” gyrotron setup were strongly limited by instabilities on the High Voltage Power Supply (HVPS). Nevertheless, the nominal mode TE<sub>32,9</sub> at correct frequency ~170 GHz has been excited. The gyrotron has been also investigated at both operating points (low voltage & nominal). After minor optimization of the gyrotron operating point the tube was able to generate 1 MW power for 1 ms pulse length with reasonable efficiency ~28%. The further experiments started at the beginning of 2015, where many interesting investigations as more accurate verification of the gyrotron operating points, operation with depression voltage in order to measure the overall gyrotron efficiency, estimation of the Gaussian mode content of the RF output beam, measurement of the stray losses, expansion of the pulse length, etc. are scheduled.

### 1.3.6 Summary on the initial short-pulse experiments

Initial experiments with the SP tube were performed, using an existing electron gun, which was not designed for this tube. An output power in excess of 1 MW was successfully generated with an electronic efficiency and a frequency which are compatible with ITER requirement. The Gaussian mode content of the output beam is estimated to 96.5%, a value also compatible with ITER gyrotron specifications. No parasitic oscillations were observed while the internal stray radiation losses remain at a low, acceptable level. In addition, comparisons between the experimental results and simulation results are in excellent agreement.

Experiments of the SP gyrotron with the nominal MIG are ongoing. The aim of these experiments is to validate the design of the nominal MIG, as well as, the operation with depressed collector voltage.

The delivery of the CW prototype is expected in summer 2015.

### 1.3.7 Beam-wave interaction modelling (F4E GRT-432, 553)

Extensive, highly realistic multi-mode interaction simulations for the 170 GHz, 1 MW EU gyrotron for ITER have been performed using EURIDICE. The following issues were addressed: (i) The validation of the beam-wave interaction for the updated, definitive gun design (Gun v3-FT), including parameter scans. (ii) The identification and validation of an operating point for highly efficient 1 MW operation at lower voltage (~70 kV), both in CW and short-pulse operation. Typical results are shown Fig. 1.3.9. In addition, the investigations on the modelling of the parasitic dynamic After-Cavity Interaction (ACI) were continued with trajectory codes, PIC codes, as well as CST Particle Studio (in collaboration with HELLAS). It was concluded that, in most cases, dynamic ACI is an artefact of the extensively used trajectory codes, which, as a result were proven to be inappropriate for such simulations.

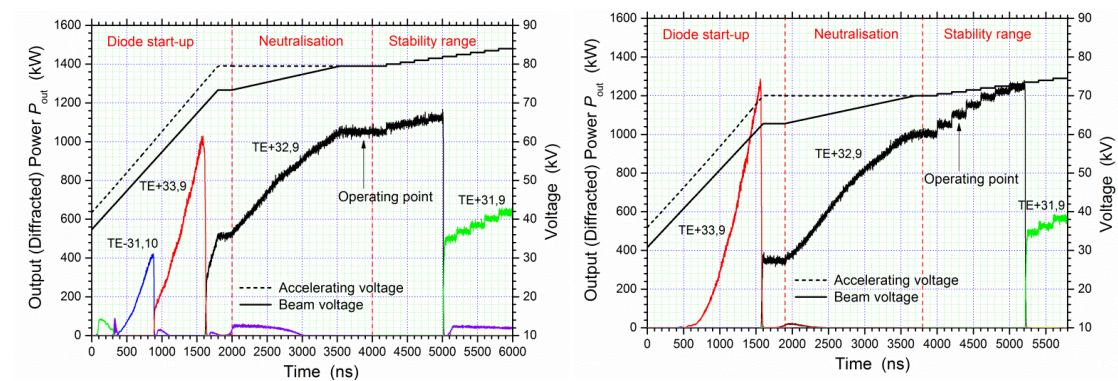


Fig. 1.3.9 Multi-mode interaction simulations for the EU gyrotron for ITER. Left: Nominal operating point (79.5 kV, 40 A). Right: Low-voltage operating point (71 kV, 45 A).

### 1.3.8 Quasi-optical mode converter and matching optical unit for the TE<sub>32,9</sub>-mode gyrotron

A quasi-optical mode converter developed for the TE<sub>32,9</sub>-mode gyrotron consists of a mirror-line launcher and three quasi-quadratic mirrors. As the surface contours of mirror-line launchers are much complicated than helically deformed launchers, it is very important to investigate the tolerance of the quasi-optical mode converter.

The launcher has been tested with the low power microwave source at KIT. The mode purity of the source used in the low power measurement is estimated to be approximately 98.7%. In the simulation, the counter-rotating component of 1.3% has been included. Concerning both location and shape the measurement and the simulation of the launcher output pattern show very good agreement.

The tolerance of the quasi-optical mode converter has been investigated, and the influence of frequency shift on the Gaussian mode content has also been investigated (see Fig. 1.3.10).

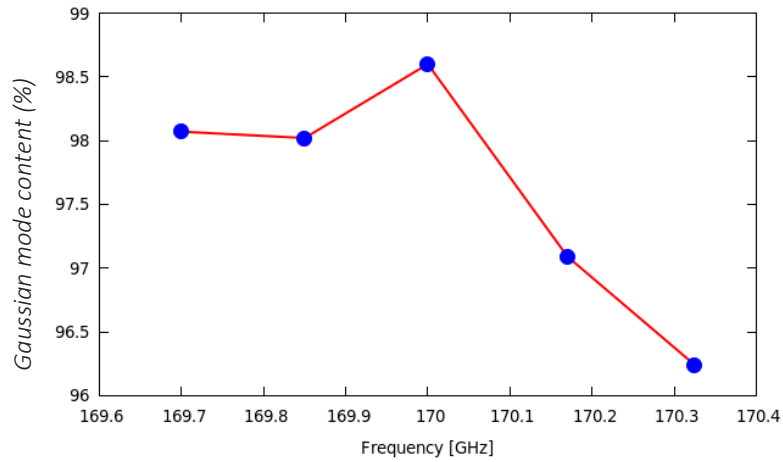


**Fig. 1.3.10**  
Gaussian mode content vs frequency.

A Matching Optical Unit (MOU) designed for the TE<sub>32,9</sub>-mode ITER gyrotron has been improved. The beam-shaping mirrors have been optimized to provide a conversion efficiency of 98.3% for the RF beam to the HE<sub>11</sub>-mode which can satisfy the requirement of the conversion efficiency to be larger than 95%, and the power transmission is calculated to be 98.5%. The field distribution of the RF beam radiated from the MOU is shown in Fig. 1.3.11. The dimensions of the MOU vessel have to be defined taking into account the possible displacement of the mirrors and the installation of an appropriate cooling system.

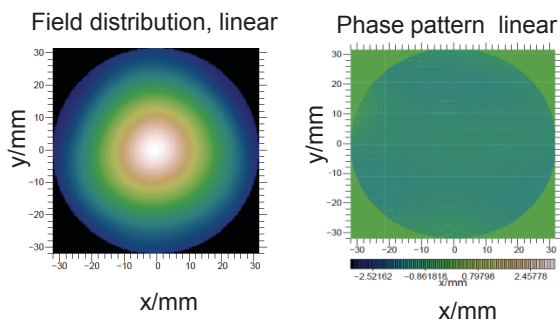


**Fig. 1.3.11**  
Field distribution at the output of the MOU.

A computer code for the vector analysis of fields in launchers is under development at KIT. In addition, a subroutine for the generation of curved triangle meshes has been developed in order to match the circular waveguide wall surface.

A new numerical method for the synthesis of launchers for high power gyrotrons has been developed. Based on the new method, a launcher has been designed as shown in Fig. 1.3.12, where the operating mode is the TE<sub>32,9</sub>-mode and frequency is 170 GHz, and the Gaussian mode content is calculated to be 98.66% at the launcher aperture. In Fig. 1.3.12, the wall profile is somewhat a combination of harmonic and mirror-line deformation. Such kind of launchers can be called hybrid-type launchers.

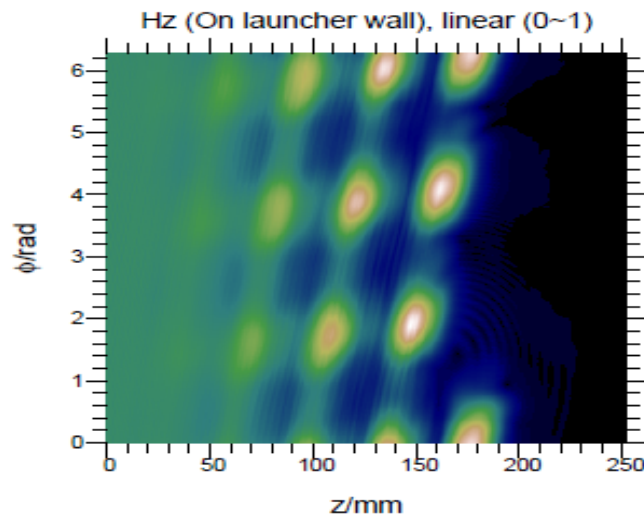
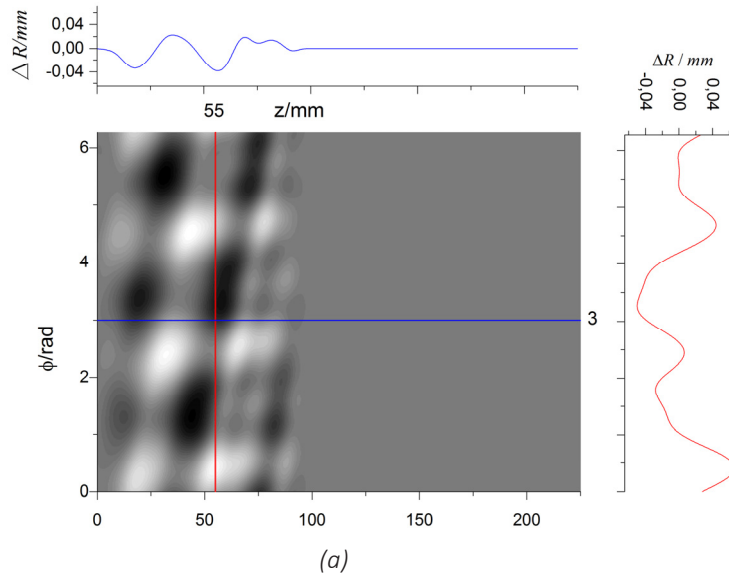


Fig. 1.3.12 Hybrid-type launcher designed for the conversion of the TE<sub>32,9</sub> mode @ 170GHz, wall profile (a) and field distribution on launcher wall (b).

## 1.4 Frequency Step-Tunable Gyrotron Development for future ECCD Systems

### 1.4.1 Introduction

Frequency step-tunable gyrotrons capable to operate in a frequency range of a few tens of GHz have attracted a great interest for application to advanced electron cyclotron resonance heating (ECRH) and current drive (CD) systems in future nuclear fusion devices. For instance, a broadband ECRH system is under development at the ASDEX upgrade tokamak. Due to the gradient of magnetic induction always present in toroidal devices, the RF energy is efficiently deposited in a well localized narrow plasma layer. Based on that at a certain RF frequency the magnetic field is no longer a free parameter and must be defined by the heating conditions. However, in fusion devices, it is desirable to have the magnetic field as a free parameter for operation with different plasma currents. Furthermore, the suppression of neoclassical tearing modes requires driving current on the high magnetic field side, without changing the magnetic field. Other layers of plasma can be reached by a change of the gyrotron frequency or using mechanically steerable mirrors inside the toroidal chamber making use of the Doppler shift. The last one requires the installation of movable parts (flexible cooling pipes) inside the plasma chamber, which is not desirable, and the first solution is more advantageous.

In comparison with single-mode devices operating at fixed frequency the development of megawatt multi-frequency gyrotrons faces additional challenges: (a) effective interaction of the electron beam with the several operating modes in the gyrotron cavity, (b) quasi-optical output-coupling system, efficiently working at the several modes with high Gaussian mode content at the output window and producing only a low stray radiation level, (c) broadband dielectric output vacuum window.

The optimization of the beam-wave interaction in the cavity of the IHM (KIT) D-band (110...170 GHz) gyrotron was performed several years ago and the results of the experimental tests for that resonator geometry were presented in previous annual reports. In the current study, an updated cavity geometry has been experimentally investigated. The new geometry was developed in order to improve the efficiency of the interaction and the output power.

### 1.4.2 Experimental set-up

The design of the KIT step-tunable gyrotron is modular which means that it is a demountable D-band gyrotron used for various tests and component verifications. A schematic view of the experimental setup is shown in the Fig. 1.4.1.

In the experiments, frequency tuning by changing the operating cavity mode has been achieved by slow variation of the magnetic field produced by the superconducting (SC) gyrotron magnet.

A broadband silicon-nitride Brewster angle window provided by National Institute of Fusion Science, Toki, Japan (NIFS) has been used for RF transmission.

The quasi optical system of the multi frequency gyrotron and its performance has been optimized for different frequencies.

The magnetron-injection-gun (MIG) is of triode type (currently used in diode mode operation) equipped with a LaB6 emitter. Initially the design of the MIG was developed for a 1MW gyrotron operating at TE<sub>22,6</sub> mode.

Special attention was paid to the quality of the hollow electron beam inside the cavity. It was noticed during the former experiments that the thermal pattern produced by the electron beam on the surface of the collector showed azimuthally non-homogenous electron emission from the cathode of the magnetron injection gun (MIG) and an axially misaligned electron beam. Non-homogeneity of the emission was in the range of 50% of the intensity. The cathode was exchanged by a new, spare one having significantly better emission properties.

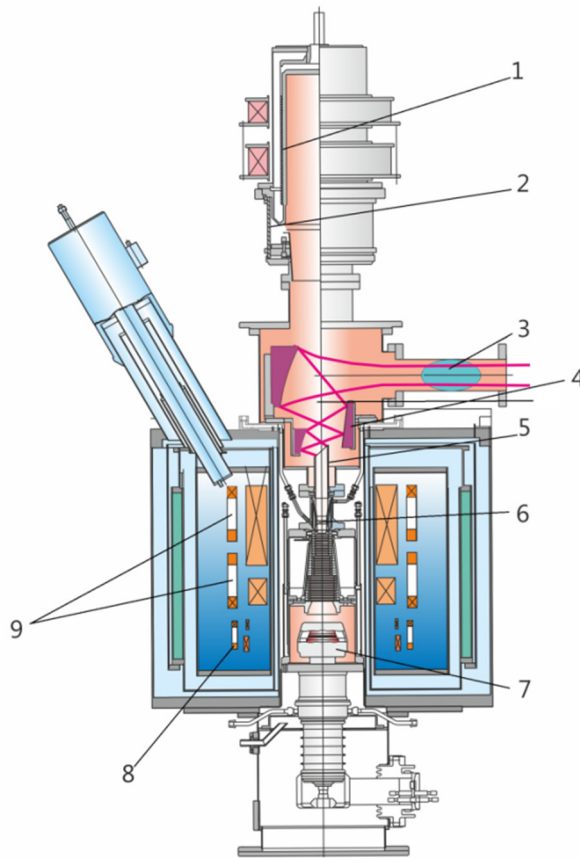


**Fig. 1.4.1**

**Gyrotron and super conducting magnet layout. 1 – collector, 2 – insulating ceramics, 3 - Brewster window, 4 – mirror box, 5 – launcher, 6 – cavity, 7 – electron gun, 8 – SC magnets, 9 – dipole coils.**

After an iterative procedure with angle of SC magnets alignment the tolerance of 0.1 mm axial misalignments between the magnetic and mechanical axis was achieved at the position of electrons fly-path from the emitter to the cavity. That led to improved axial alignment of the electron beam.

Modularity of the gyrotron allowed easy replacement of the resonator by a new one which has an extended length of the section with constant diameter, in comparison to one used before.

### 1.4.3 Numerical Simulation

At 140 GHz the operating gyrotron cavity mode is a  $TE_{22,8}$ -mode. The original cavity, along with the non-linear uptaper and the cutoff section is shown in Fig. 1.4.2. The magnetic field profile is also shown. This resonator has a middle section with length  $L_2 = 14.5$  mm. Several results of the experimental study with this original geometry have been presented in previous annual reports.

The new version of the resonator was numerically optimized using the EURIDICE code-package. The objective of the numerical optimization was to increase the interaction efficiency by a parametric study of its dependence on the length  $L_2$  of the middle section. It is known that longer resonators can lead to an increase of the interaction efficiency. However, the diffractive quality factor increases accordingly as  $Q_{dif} \sim (L_2/\lambda)^2$ . This leads to an increase of the ohmic losses and to a decrease of the starting currents of the competing modes, which raises the risk of mode competition. Multi-mode simulations are thus necessary to assess the trade-off between interaction efficiency and ohmic losses / mode competition, when the length of the middle section is changing.

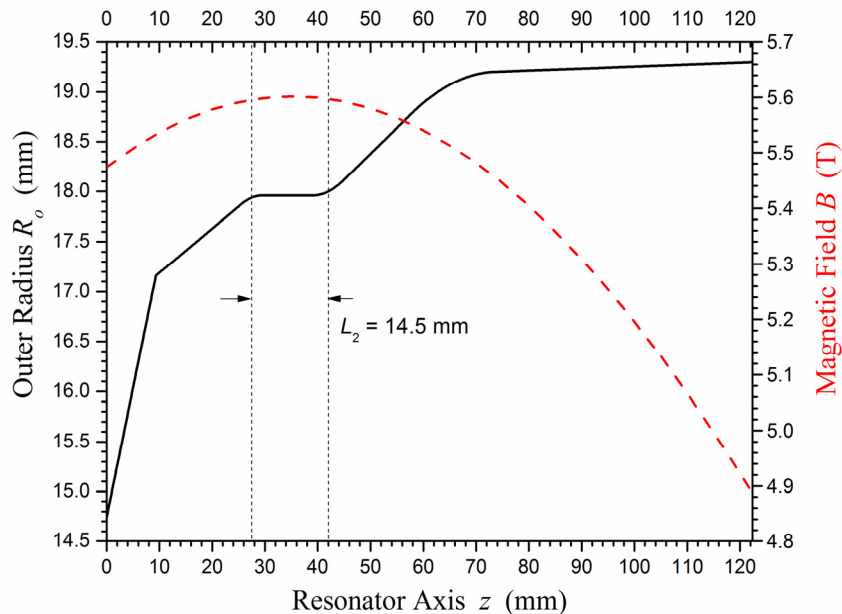
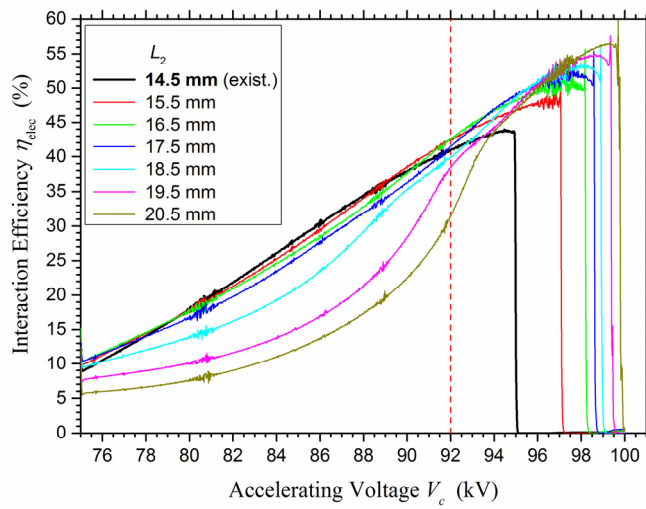


Fig. 1.4.2 Original version of the resonator geometry (solid line) and magnetic field profile (dashed line).

For the numerical simulations, the selected reference operating point for the  $TE_{22,8}$ -mode at 140 GHz is: accelerating voltage  $V_c = 92$  kV, electron beam current  $I_b = 40$  A, maximum magnetic field  $B_0 = 5.6$  T, and, electron beam radius  $R_b = 7.95$  mm (for maximum coupling). Note that because of the voltage depression due to the beam space charge in short pulse operation, the given accelerating voltage corresponds to a beam voltage  $V_b \sim 86$  kV (beam energy). This is taken into account in the simulations. In order for the results to be even more relevant with the possible experimental operating configurations, two values for the electron velocity ratio were considered:  $\alpha = 1.3$  and  $\alpha = 1.4$ . Such values are achievable experimentally by properly setting the currents to the magnet coils. For the parametric study, the length  $L_2$  of the middle section of the resonator was changed in steps of 0.5 mm from its value in the original resonator (14.5 mm) up to 20.5 mm. The wall smoothing sections were kept the same as in the original version but the taper

angles were slightly modified in order to secure fixed initial and final wall radii, as well as fixed total length (122.35 mm). The conductivity value used for the calculation of the realistic ohmic losses is  $\sigma = 1.73 \times 10^7$  S/m.

At the initial step, single-mode simulations of the cavity only (i.e. from  $z \sim 10$  mm to  $z \sim 55$  mm in Fig. 1.4.2) and assuming a homogeneous magnetic field were performed. The calculated interaction efficiency versus the accelerating voltage with reference pitch factor  $\alpha = 1.4$  and for several values of  $L_2$  is shown in Fig. 1.4.3. In these simulations, as the accelerating voltage is increasing, the electron velocity ratio  $\alpha$  is changing adiabatically and the beam current is changing using the Schottky formula. Apparently, by increasing the middle section length  $L_2$ , no saturation in the maximum achievable interaction efficiency is found. However, after  $L_2 = 17.5$  mm the increase in maximum efficiency is small and the required operating parameters are significantly different from the reference values  $V_c = 92$  kV,  $B_0 = 5.6$  T.



**Fig. 1.4.3**  
Single-mode simulations of the TE<sub>22,8</sub> mode: Dependence of the interaction efficiency on the accelerating voltage for different lengths  $L_2$  of middle section the resonator.

In order to investigate the effect of mode competition which results in a saturation of the gyrotron efficiency, the above start-up simulations were repeated taking into account 29 competing modes. These are the modes having their resonance frequencies within 95-105% of the frequency of the operating TE<sub>22,8</sub>-mode and beam coupling factors larger than 50% compared to that of the operating mode. In the case of  $\alpha = 1.3$  the maximum achievable efficiency in stable single-mode operation reached saturation at  $L_2 = 18.5$  mm, whereas in the case of  $\alpha = 1.4$  the maximum achievable efficiency reached saturation at  $L_2 = 16.5$  mm. Given these results the value  $L_2 = 17.5$  mm was chosen for the new resonator.

	<i>Original Version</i>	<i>New Version</i>
<i>Middle section length <math>L_2</math> (mm)</i>	<i>14.5</i>	<i>17.5</i>
<i>Cold diffractive quality factor <math>Q_{dif}</math></i>	<i>830</i>	<i>1240</i>
<i>Magnetic field <math>B_0</math> (T)</i>	<i>5.6</i>	<i>5.6</i>
<i>Acc. voltage <math>V_c</math> (kV)</i>	<i>90.0/93.0</i>	<i>94.5/95.0</i>
<i>Beam voltage <math>V_b</math> (kV)</i>	<i>83.9/86.5</i>	<i>88.3/88.4</i>
<i>Beam current <math>I_b</math> (A)</i>	<i>39.4/39.9</i>	<i>40.2/40.2</i>
<i>Pitch factor <math>\alpha</math></i>	<i>1.28/1.41</i>	<i>1.31/1.43</i>
<i>Frequency (GHz)</i>	<i>140.11/140.10</i>	<i>140.05/140.06</i>
<i>Power <math>P_{out}</math> (kW) (at end of the uptaper)</i>	<i>1000/1280</i>	<i>1400/1450</i>
<i>Losses <math>P_{ohm}</math> (kW)</i>	<i>40/48</i>	<i>61/62</i>
<i>Ohmic wall loading <math>\rho_{out}</math> (kW/cm<sup>2</sup>)</i>	<i>2.0/2.4</i>	<i>3.0/3.0</i>
<i>Interaction eff. <math>\eta_{elec}</math> (%)</i>	<i>31.5/38.5</i>	<i>41.2/42.5</i>
<i>Transverse eff. <math>\eta_{\perp}</math> (%)</i>	<i>50.7/57.9</i>	<i>65.2/63.3</i>
<i>Output eff. <math>\eta_{out}</math> (%)</i>	<i>28.2/34.5</i>	<i>36.9/38.0</i>

**Table 1.4.1**  
**Operating parameters and performance of the TE<sub>22,8</sub> mode in the original and new resonator**  
**(for low/high pitch factor  $\alpha$ )**

To further validate the new resonator with  $L_2 = 17.5$  mm, additional more realistic multi-mode simulations were performed. The full cavity and non-linear uptaper geometry was simulated and the axial dependence of the magnetic field was taken into account. The beam parameters during the voltage ramp-up were provided by the beam optics code ESRAY. ESRAY calculated also a velocity spread of around 5% rms in pitch factor  $\alpha$ , which was considered in the multi-mode interaction simulations. The simulations validated the new cavity design. Typical results are shown in Fig. 1.4.4, where the power diffracted from the right end of the geometry (i.e.  $z = 122.35$  mm) is plotted versus the accelerating voltage for the case  $\alpha = 1.4$ .

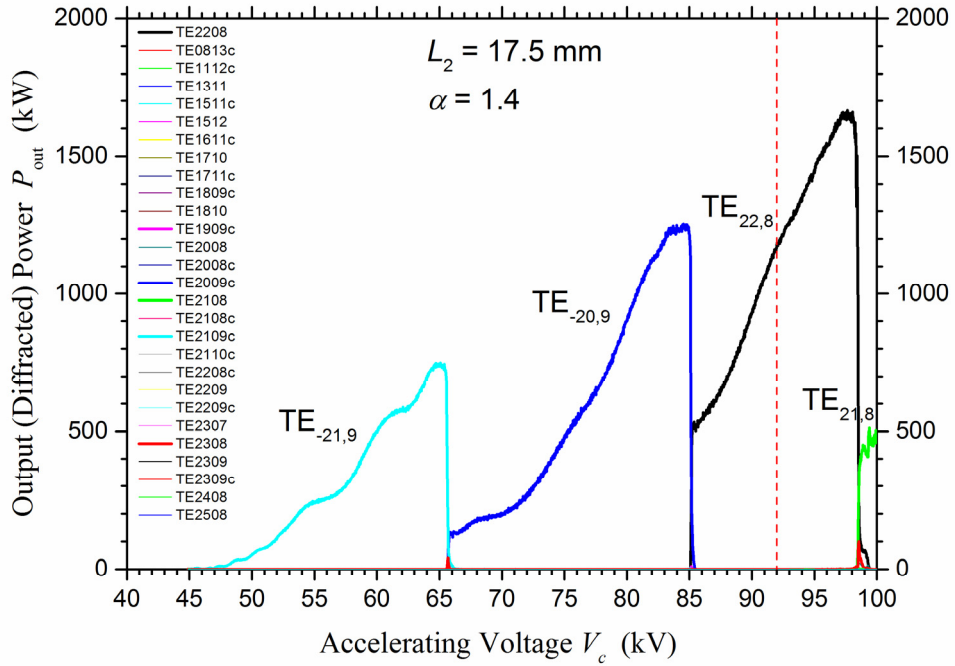


Fig. 1.4.4 Multi-mode simulations of the new version of the resonator: Dependence of the output power on the accelerating voltage. (A negative azimuthal index denotes a counter-rotating mode.)

The calculated performances of the original and the new version of the cavity regarding the  $TE_{22,8}$ -mode for low and high electron velocity ratios  $\alpha$  are compared in Table 1. For each case, the level of the accelerating voltage is chosen to be around 2.5 kV lower than the maximum accelerating voltage at which the operating mode is lost. The effect of the longer cavity is verified by the significantly increased transverse efficiency  $\eta_{\perp} = \eta_{elec}(1+\alpha^2)/\alpha^2$ , where the interaction efficiency is defined as  $\eta_{elec} = (P_{out} + P_{ohm})/(V_b I_b)$ . The output efficiency  $\eta_{out} = P_{out}/(V_c I_b)$  is also shown. With the new version, an output efficiency enhancement by 30% for low  $\alpha$  and by 10% for high  $\alpha$  is demonstrated.

After the investigations reported above, for new series of measurements a resonator with a 17.5 mm long cylindrical middle section was produced and installed in the gyrotron. The experimental results are presented in the next section.

#### 1.4.4 Experimental Results

In this section the results of the measurements using the optimized new resonator will be presented.

The radius of the resonator in the middle section is  $R_r=17.96$  mm.

In the Table below the experimental output power, for all measured modes and the corresponding beam parameters are summarized.

<i>Mode</i>	<i>V<sub>acc</sub>[kV]</i>	<i>U<sub>b</sub>[keV]</i>	<i>R<sub>b</sub>[mm]</i>	<i>I<sub>b</sub>[A]</i>	<i>B[Tesla]</i>	<i>P<sub>out</sub>[kW]</i>
<i>TE<sub>28,9</sub></i>	<i>79.3</i>	<i>74.9</i>	<i>8.07</i>	<i>43.0</i>	<i>6.647</i>	<i>1150</i>
<i>TE<sub>27,9</sub></i>	<i>82.7</i>	<i>78.3</i>	<i>8.15</i>	<i>44.0</i>	<i>6.562</i>	<i>1070</i>
<i>TE<sub>26,9</sub></i>	<i>82.7</i>	<i>77.4</i>	<i>7.97</i>	<i>42.0</i>	<i>6.398</i>	<i>1200</i>
<i>TE<sub>25,9</sub></i>	<i>81</i>	<i>75.5</i>	<i>8</i>	<i>44</i>	<i>6.264</i>	<i>1093</i>
<i>TE<sub>24,8</sub></i>	<i>74.0</i>	<i>68.2</i>	<i>8.04</i>	<i>42.5</i>	<i>5.711</i>	<i>1200</i>
<i>TE<sub>23,8</sub></i>	<i>74.0</i>	<i>67.6</i>	<i>8.02</i>	<i>44.0</i>	<i>5.584</i>	<i>1210</i>
<i>TE<sub>22,8</sub></i>	<i>76.0</i>	<i>69.1</i>	<i>8.05</i>	<i>45</i>	<i>5.468</i>	<i>1150</i>
<i>TE<sub>21,7</sub></i>	<i>74.3</i>	<i>68.8</i>	<i>8.33</i>	<i>43.0</i>	<i>4.97</i>	<i>1035</i>
<i>TE<sub>20,7</sub></i>	<i>77.3</i>	<i>71.6</i>	<i>8.3</i>	<i>42.5</i>	<i>4.86</i>	<i>1004</i>

**Table 1.4.2**  
Experimentally measured output power and corresponding parameters (magnetic field in cavity, beam current, beam radius, beam energy).

The electron gun of the gyrotron was operated as a diode MIG. The radius of the electron beam changes as  $\propto f^{1/3}$  with the frequency  $f$  from 124 GHz up to 169 GHz. A pair of gun coils is used to keep the pitch factor of the electrons at the design value. Both, in the simulation and in the experiment for the excitation of most of the cavity modes the pitch factor  $\alpha = 1.4$  was used.

Since the operation of the gyrotron was performed in short pulses ( $\approx 1$  ms), in order to estimate the interaction efficiency the depression of the electron beam voltage in the cavity region must be taken into account. It adds to the other stray losses and ohmic losses. As an example, for the oscillation in the  $TE_{23,8}$ -mode at 143.36 GHz with an output efficiency of 37%, according to the simulation, for a cathode voltage of 74 kV, a beam current of 44 A and the actual magnetic field used in the experiment, the beam energy in the cavity is 67.6 keV. Therefore, we can estimate that the interaction efficiency must be at least 40% (here we have neglected stray and ohmic losses). The corresponding beam energies for all considered modes are presented in the Table 1.4.2.

The highest output power of about 1440 kW was measured for the  $TE_{23,8}$ -mode at 143.36 GHz with an increased beam current of  $I_{\text{beam}} = 54$  A. In this case the efficiency was 35%.

The experimental measurements for all the different cavity modes were performed at reduced cathode voltage ( $\approx 75$  kV). A systematic measurement of the gyrotron performance in a wider range of parameters was not completed due to lack of time.

### 1.4.5 Conclusions

The recent results of the step-frequency tunable D-band gyrotron at IHM with a numerically optimized countour of the resonator show an improved performance in terms of efficiency and output power. The gyrotron was operated in the frequency range from 124 GHz up to 169 GHz. The highest achieved output efficiency of the device was around 38% (without depressed collector operation). For all the different cavity modes an output power of minimum 1 MW has been demonstrated.

## 1.5 EUROfusion: Research and development towards a Gyrotron for future DEMO

### 1.5.1 Summary

This section covers the work done in 2014 in frame of the Heating & Current Drive (H&CD) Project implemented under the EUROfusion Consortium for the period 1<sup>st</sup> January 2014 to 31<sup>st</sup> December 2020 (although the financial framework is defined from 2014 to 2018). This project forms part of the European DEMO CDA Programme. In 2012, former EFDA published “Fusion Electricity – A roadmap to the realisation of fusion energy” that sets out a strategic vision to demonstrate the generation of electrical power by a Demonstration Fusion Power Plant (DEMO) by 2050. The roadmap elaborates 8 strategic missions to tackle the main challenges in achieving this overall goal. The need for the Heating & Current Drive (H&CD) Project is derived from following:

*“In a DEMO based on long-pulse/inductive regimes of operation, and not on fully steady state, Heating and Current Drive (H&CD) systems need primarily to provide heating power for H-mode access, capability of MHD instabilities suppression and increase of the pulse length whereas the detailed control of the equilibrium current density profile will not be the primary requirement... Therefore, the approach taken in the Roadmap in the H&CD area under Mission 6 is to pursue only specific developments to comply with the parameters of DEMO (e.g. higher magnetic field) and to ensure high system availability (e.g. by minimizing the need of maintenance outside the scheduled periods), reliability (e.g. by ensuring the modularity of the systems) and plant efficiency (e.g. by minimizing the re-circulating power). This will involve mainly R&D activities in the area of NB and EC technologies. These activities will be complemented by an analysis of the plasma regimes in DEMO to guide the final decision on the H&CD systems to be taken on the basis of the ITER experience.”*

The primary objective of the DEMO Heating & Current Drive Project is to deliver a feasible, integrated concept design of the DEMO Heating & Current Drive System, with an acceptable confidence level to meet the Heating & Current Drive Requirements. The DEMO Heating & Current Drive System will form an essential system of the European demonstration fusion power plant, referred to as DEMO.

The concept design shall be substantiated and verified to an appropriate level for a plant-level Conceptual Design Review by activities such as CAD modelling, engineering analysis, prototyping and testing of components, manufacturing feasibility studies, cost analysis, RAMI analysis, Safety analysis, etc.

The activities performed in the frame of the WP H&CD will be complemented by other activities included in other EUROfusion WPs (specially for IC) and by an analysis of the plasma regimes in DEMO to guide the final decision on the H&CD systems to be taken on the basis of the ITER experience.

The detailed work programme for the DEMO activities is described in [3]. Related to gyrotron development the institutes IHM and IAM-AWP are involved in the work packages related to WP HCD 4.0 “Electron Cyclotron (EC) R&D, conceptual design and advanced technologies”. In particular KIT is responsible for the work packages

- 4.2. “Electron Cyclotron (EC) R&D, Conceptual Design and Advanced Technologies: R&D”
- 4.3. “Electron Cyclotron (EC) R&D, Conceptual Design and Advanced Technologies: Advanced Technologies”

The work packages are performed in close cooperation with HELLAS, Greece and EPFL-CRPP, Switzerland.

The work packages contain four major topics:

Verification of the leading EU coaxial-cavity technology as base for future DEMO (upgrade of the 170 GHz coaxial SP prototype and experimental verification)

Conceptual design and advanced tool developments for future frequency step-tunable 240 GHz gyrotrons and necessary broadband window technologies

Preparation of the experimental setup for future DEMO (10 T SC magnet, characterization methods for dielectric materials of critical gyrotron components at 240 GHz (at CRPP))

Advances in multistage depressed collector technologies for future high-efficient DEMO gyrotrons

In 2014, following activities have been performed:

- 4.2.1 Experiments using the 2 MW coaxial modular short-pulse pre-prototype

The experimental performance of the KIT 170 GHz, 2 MW coaxial-cavity gyrotron modular short-pulse pre-prototype has been validated in short pulse and depressed-collector operation. An output power of ~1.9 MW and an efficiency of ~47% at ~3 ns has been achieved (51 kV + 39 kV (depression voltage), 76 A beam current). Numerical verification of the experimental results has been performed.

- 4.2.2 Verification of coaxial gyrotron pre-prototype at longer pulses

A scientific design for an improved magnetron injection gun for the KIT 2 MW coaxial short-pulse pre-prototype has been started. Numerical studies on alternative operating points for improved performance of the gyrotron have been done.

- 4.2.3 Conceptual design of a 240 GHz step-frequency tunable short-pulse pre-prototype

A systematic mode-selection approach for very high-order mode gyrotrons have been derived.

Initial conceptual studies on the 240 GHz gyrotron (conventional/coaxial) and auxiliaries have been done. Initial physical design for key components (cavity, MIG - in progress) and corresponding numerical studies have been done.

In frame of the numerical tool development at Hellas following activities have been performed:

Mode-selectivity properties of gyrotron cavities with double corrugation, CCCI code extension and benchmarking at higher-order modes

Studies on parasitic oscillations in gyrotron beam tunnels, work on improved boundary condition in NESTOR code, studies on existing gyrotrons

- 4.2.4 Test assemblies of broadband windows

An initial market survey for available diamond discs has been done. Focus has been on expanding the diameter above 140 mm leading to aperture of the waveguide >50 mm for a CVD-diamond Brewster-angle window. Different indirect cooling layouts for diamond Brewster-angle windows were investigated and the temperature distributions and resulting stresses were studied. In all cases, the temperature is not above the allowable limits.

At CRPP the optical test bench for verification of dielectric materials has been procured and commissioned. The measurement methodologies are being defined and preliminary dielectric permittivity measurements of relevant materials for the gyrotron R&D have been performed in the 140-220 GHz frequency band.

- 4.2.5 10 T magnet installation and testing

Requirements on the magnet and initial specifications have been set. Suppliers have been involved and initial scouting for available magnets have been done.

- 4.3.1 Concept design of Multi-Stage Depressed Collector (MSDC)

A systematic approach has been started to develop algorithms and codes to find the optimal electrodes' voltages and efficiencies for multi-stage depressed collectors. As base for that a survey and classification of existing MSDC concepts has been done. Initial conceptual simulations and studies of two-stage collector configurations have been performed which allows to increase the efficiency of a gyrotron by total 10%, finally limited by secondary electrons.

In the following sections more detailed description for the different work packages are provided.

## 1.5.2 Verification of the Coaxial-Cavity technology for DEMO

### Introduction

The development of the modular 2 MW, 170 GHz short-pulse pre-prototype as base for multi-megawatt CW coaxial-cavity gyrotrons beyond ITER (Fig. 1.5.1) is in progress at Karlsruhe Institute of Technology (KIT). Coaxial-cavity gyrotrons, with inner conductor, offer significant advantages in comparison to conventional gyrotrons with a hollow circular waveguide cavity, namely reduced voltage depression and a reduced mode competition, resulting in higher RF output power at even higher operating frequencies. It is assumed that in future for the demonstration fusion power plant (DEMO), gyrotrons delivering RF power in the multi-megawatt range at frequencies above 200 GHz will be required. Gyrotrons of coaxial-cavity type are a promising option for the future applications. First experimental results obtained with the 2 MW, 170 GHz modular-type short-pulse coaxial-cavity pre-prototype have been published in. The current modular pre-prototype configuration allows the generation of >2 MW RF output power in short-pulses with a reasonable electronic efficiency of approximately 30% without depressed collector operation. Recently, experiments with a single-stage depressed collector (SDC) have been performed. In depressed operation the overall efficiency of the gyrotron has been increased to ~48%. The design specifications including the nominal operating parameters are summarized in Table 1.5.1.

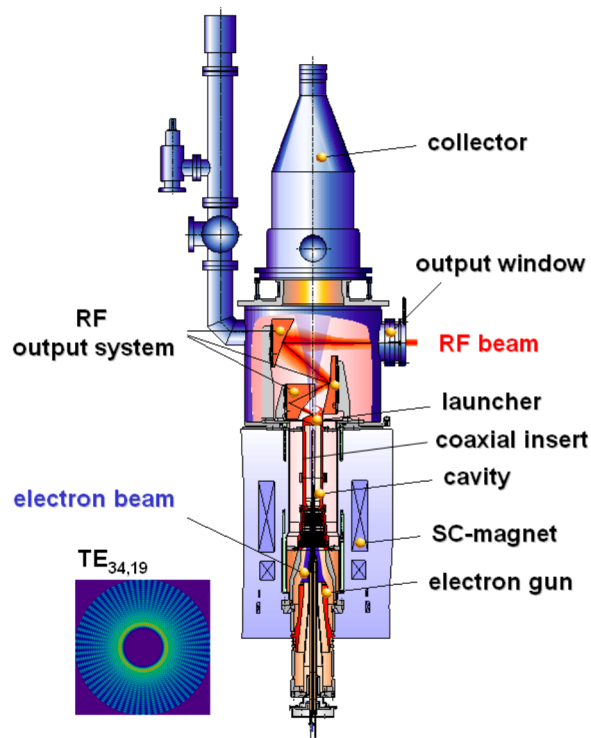


Fig. 1.5.1  
Coaxial-Cavity Gyrotron

<i>Operating cavity mode</i>	<i><math>TE_{34,19}</math></i>
<i>Frequency</i>	<i>170 GHz</i>
<i>RF output power</i>	<i>2 MW</i>
<i>Beam current</i>	<i>75 A</i>
<i>Accelerating voltage</i>	<i>90 kV</i>
<i>Velocity ratio</i>	<i><math>\sim 1.3</math></i>
<i>Cavity magnetic field</i>	<i>6.87 T</i>
<i>Efficiency with SDC</i>	<i>&gt;50%</i>

Table 1.5.1

#### Achieved Results in 2014

In the recent experiments two effects - firstly, a halo current of the electron beam and, secondly, parasitic low frequency (LF) oscillations - have limited the gyrotron operation. It has been found, that the halo current was generated at the cathode surface, but not at the emitter region. The halo current is supposed to

be caused by electrons trapped between the cathode and the magnetic mirror at the cavity. In particular, secondary electrons emitted from the cathode surface near the emitter are assumed to contribute significantly. In order to keep the halo current small, the aperture of the anode has been narrowed by introduction of a halo-shield (see Fig. 1.5.2).

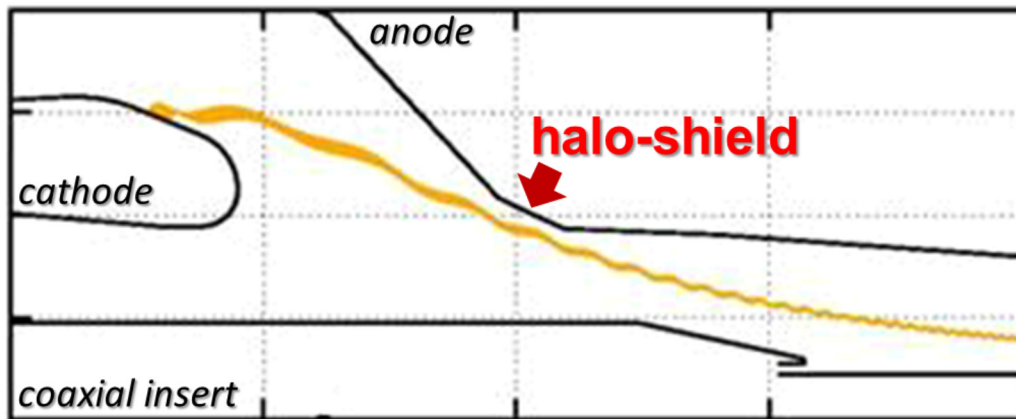


Fig. 1.5.2  
The profile of the gyrotron anode used in the experiment (halo-shield is indicated)

To understand these effects, the trajectories of electrons emitted from the cathode surface around the emitter have been calculated. The results confirmed the existence of magnetically trapped electrons between the electron gun and the cavity regions. It has been shown, that the electrons, in particular secondary electrons, emitted from the rear part region of the electron gun can easily be trapped, which would explain a forming of electron halo, observed experimentally. The second limitation was due to a parasitic LF oscillation with a very high intensity at 453 MHz which was found for beam currents  $I_b > 60$  A. That parasitic oscillation was mainly responsible for the unstable behavior of the pre-prototype in the experiment. It has been found that the parasitic LF oscillation has been excited inside the mirror box of the tube.

In the updated design, used in this reporting period, the unwanted LF oscillations have been suppressed. The suppression of the LF-oscillations increased significantly the stability of the gyrotron and allowed an operation of the tube up to the nominal parameters. However, at the nominal operating point the body current was fairly high, up to  $\sim 100$  mA. That high value is assumed to be caused by the halo current which is bombarding the anode at the position of the halo-shield. Experiments have shown that the value of the body current did rise when the electron beam current was increased. At the same time it was depending on the accelerating voltage. The gun is of diode type, therefore, the pitch factor is rising in accordance with the accelerating voltage. A higher pitch factor is accompanied by a larger number of trapped electrons and thus by an increase of the halo current. In order to reduce the body current the magnetic field profile had been modified, which increased the distance between the electron beam and the anode around the halo shield while the electron beam parameters in the cavity remained nearly constant. Already first experiments with the new magnetic field profile have shown that although the body current has been nearly completely reduced, the gyrotron operation became significantly more unstable. That confirms the hypothesis that a reduction of the beam halo, due to the electron current to the halo-shield, results in an improvement of gyrotron operation stability. Finally, after optimization of the operating parameters, an RF output power of 2 MW with an efficiency of 28% (without SDC) has been successfully achieved at pulse

lengths in the order of 1-1.5 ms. The dependency of the generated RF output power on the accelerating voltage at the beam current of 75 A is shown in Fig. 1.5.3.

In order to further increase the RF power, the static axial magnetic field in the gyrotron cavity has been slightly increased. This allowed the shift of the excitation region of the nominal mode up to ~92 kV. In parallel, the electron beam current has been set to 84 A. A new world record in the generated RF output power (per single tube), namely 2.3 MW with an efficiency close to 30%, has been obtained.

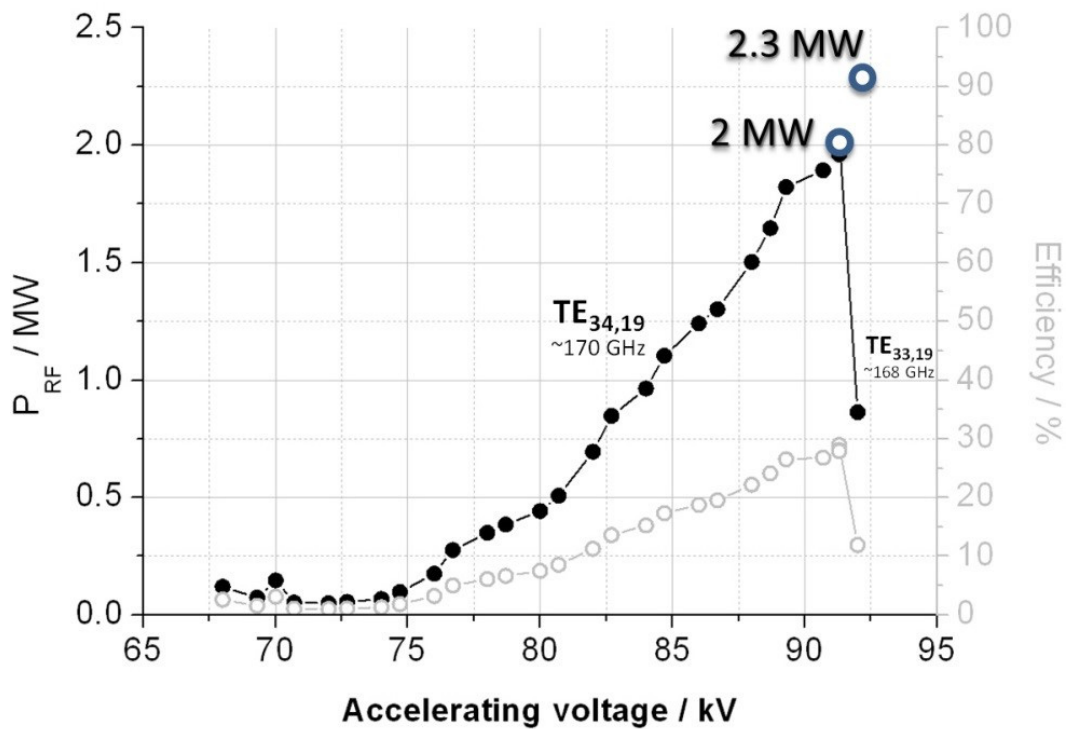


Fig. 1.5.3 Measured RF output power and efficiency as a function of accelerating voltage (obtained at  $B_{cav} = 6.87$  T and  $I_b \sim 75$  A), measured without single stage depressed collector (SDC). The record output power measured at the slightly increased operation parameters ( $B_{cav} = 6.90$  T and  $I_b \sim 84$  A) is indicated.

In order to operate the gyrotron with depressed collector, the gyrotron body has been electrically isolated from the cryostat (the collector itself is already isolated from the body using a ceramic ring) as presented in Fig. 1.5.4. The depression voltage has been connected both to the gyrotron body and to the coaxial insert. In the very first experiments some high voltage limitations have been observed already at 33-35 kV.

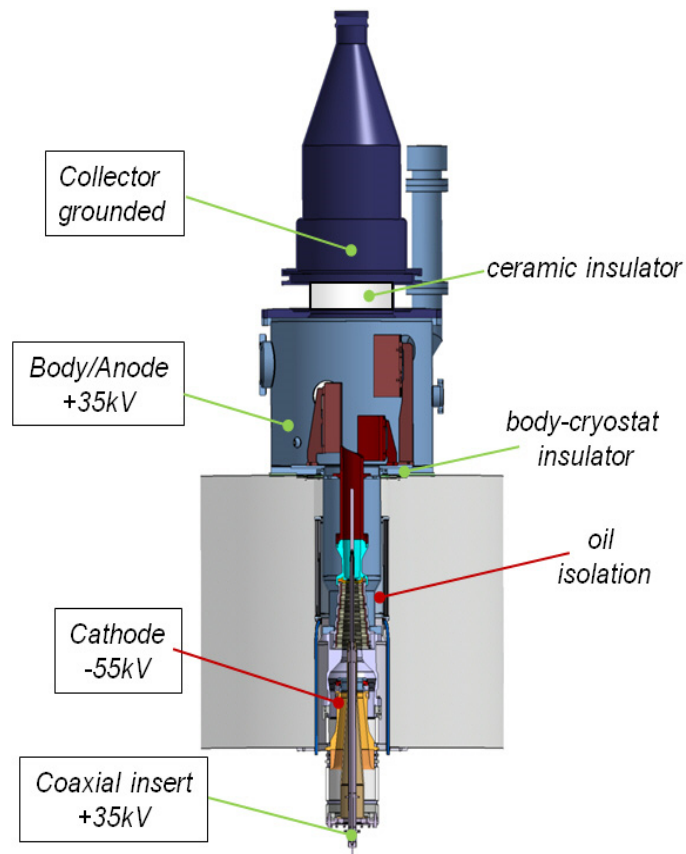


Fig. 1.5.4  
Gyrotron configuration in single stage depressed collector operation

However, further conditioning of the tube allowed finally reaching values close to 40 kV. A further increase of the depression voltage was not possible due to a limitation of the body voltage power supply. After optimization of the gyrotron operating point systematical measurements have been done at two different beam currents 76 A (nominal value) and 83 A. The main goal was to investigate the dependency of the RF output power and the overall gyrotron efficiency on the applied depression voltage. The cathode voltage was continuously tuned, keeping the total accelerating voltage ( $U_a$ ) constant. The behavior of the gyrotron during the experiments was very stable. For both values of beam current the measured output power remained constant and the overall efficiency increased vs. applied depression voltage. In the range of applied depressed voltage, no saturation of efficiency and no decrease of generated power have been observed. As well, no significant increase of the body current (gyrotron body & coaxial insert) has been noted during the operation. The achieved results are presented in Fig. 1.5.5 and Fig. 1.5.6. Finally at the operation with depression voltage close to 40 kV, 1.9 MW @  $I_b=76$  A and  $U_a\sim 90$  kV with efficiency close to 48%, and 2 MW @  $I_b=83$  A and  $U_a\sim 92$  kV with efficiency close to 45% have been demonstrated. The effective pulse length was around 3.5 ms.

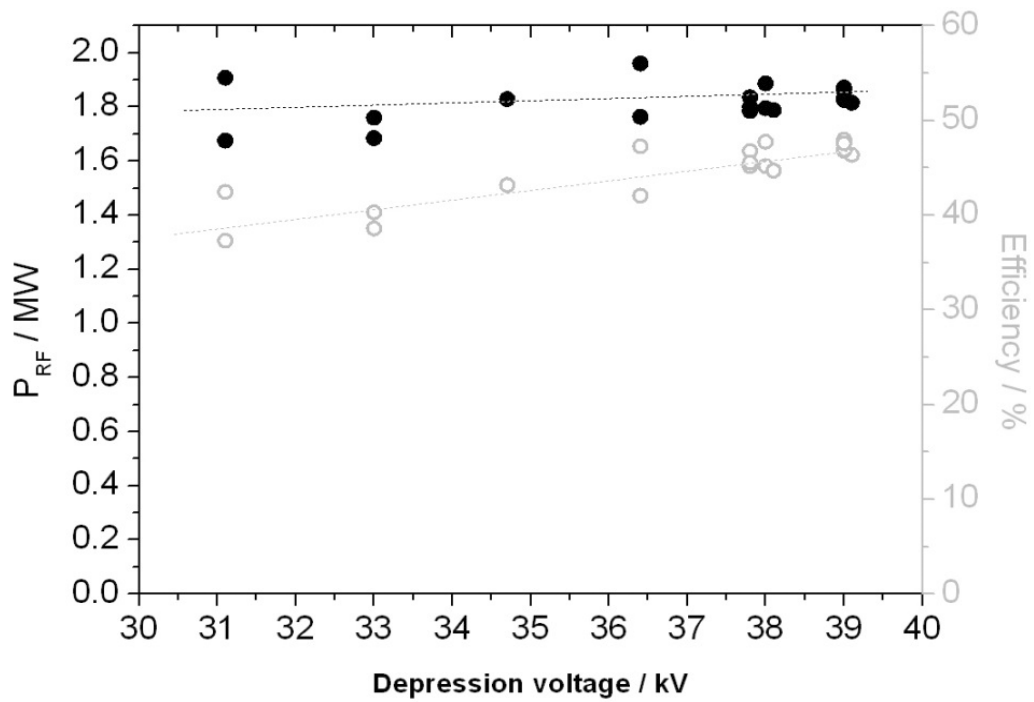


Fig. 1.5.5  
 Measured RF output power and efficiency as a function of depression voltage (obtained at  $B_{cav} = 6.90$  T and  $I_b \sim 76$  A,  $U_a \sim 90$  kV).

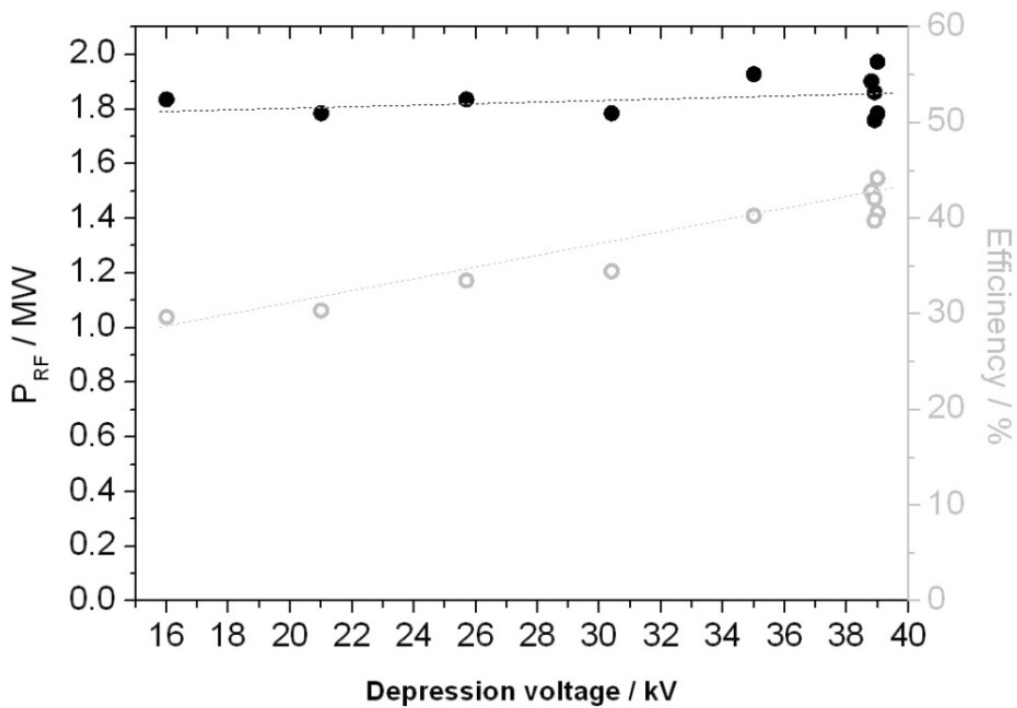


Fig. 1.5.6  
 Measured RF output power and efficiency as a function of depression voltage (obtained at  $B_{cav} = 6.90$  T and  $I_b \sim 83$  A,  $U_a \sim 92$  kV).

Numerical verification of the experimental results was also initiated. The point of maximum efficiency (48%) was considered. The experimental parameters at that point are given in Table 1.5.2.

<i>Magnet coil currents HIS/IES2/IES1/IKS/INL (A)</i>	<i>111/48.7/30.1/0/60</i>
<i>Cathode voltage</i>	<i>51 kV</i>
<i>Body (depression) voltage</i>	<i>39 kV</i>
<i>Accelerating voltage</i>	<i>90 kV</i>
<i>Beam current</i>	<i>76.5 A</i>
<i>RF output power at load</i>	<i>1.9 MW</i>
<i>Efficiency with SDC</i>	<i>48%</i>

Table 1.5.2

For these experimental values, the magnetic field profile and the electron beam parameters were obtained after electron beam-optics simulations with the *Ariadne++* code [3]. They are shown in Table 1.5.3

<i>Maximum magnetic field</i>	<i>6.891 T</i>
<i>Beam voltage (energy)</i>	<i>87.3 kV</i>
<i>Beam radius</i>	<i>9.9 mm</i>
<i>Guiding-centre spread</i>	<i>0.28 mm</i>
<i>Velocity ratio, <math>\alpha</math></i>	<i>1.353</i>
<i>rms. <math>\alpha</math>-spread</i>	<i>7.5%</i>

Table 1.5.3

Based on this magnetic field profile and beam parameters, realistic beam-wave interaction simulations were carried out using the EURIDICE code [4]. The geometry used for the simulation (cavity & nonlinear uptaper) along with the realistic magnetic field profile are shown in Fig. 1.5.7.

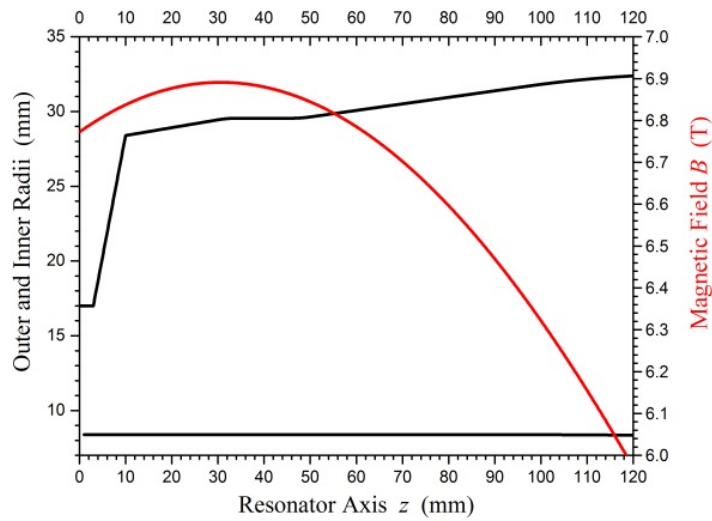


Fig. 1.5.7  
Geometry of cavity, inner conductor and magnetic field.

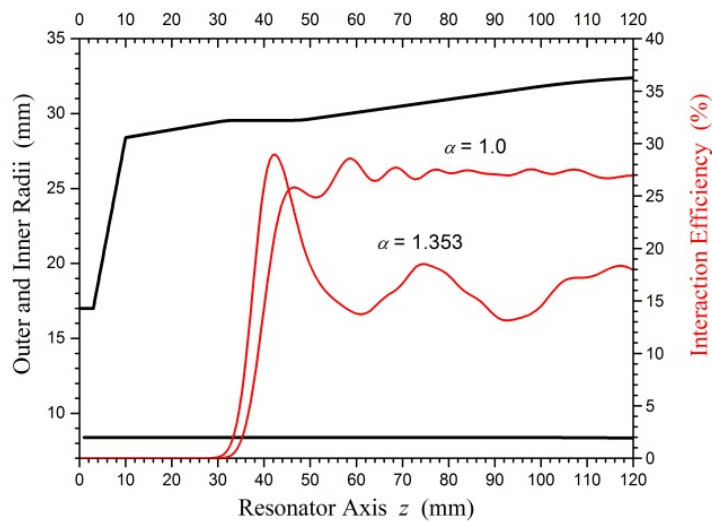


Fig. 1.5.8  
Calculated interaction efficiency.

With this configuration and assuming overall losses of around 10%, the calculated power on the load is rather low, about 1.1 MW, which is in large disagreement with the measured power of 1.9 MW. This is owed to a severe overbunching and after cavity interaction, as can be seen in Fig. 1.5.8 (case  $\alpha = 1.353$ ) where the interaction efficiency versus the cavity axis is plotted. This is an indication that the actual beam parameters are different from those considered. A possible effect could be the reduction of the velocity ratio  $\alpha$  due to the beam halo. (A halo was not considered in *Ariadne++* simulations.) For example, if  $\alpha = 1$  (rather than  $\alpha = 1.353$ ), the calculated power on the load becomes significantly larger (about 1.6 MW) because the overbunching is avoided. That's evident from Fig. 1.5.8, case  $\alpha = 1.0$ . However, there is still a remaining discrepancy with the measured power. Further investigations to understand and solve this issue are necessary.

## Conclusion

Taking into account the earlier discovered issues with the electron gun related to the electron beam halo, the achieved experimental results with the gyrotron (with and without SDC) presented in this report are very promising. The preparation of a new design of the electron gun, in which a significantly reduced value of the beam halo is expected, is in progress. As a next step the procurement of the new gun is planned. Thus a further improvement of the gyrotron stability and increase of the electrical efficiency in the future experiments is expected. In parallel, the gyrotron will be step by step prepared for operation at longer pulses. The appropriate upgrade of the gyrotron setup (i.e. installation of diamond output window, cooled cavity and long-pulse collector) is under preparation.

### 1.5.3 Towards a future 240 GHz Gyrotron for DEMO (WP HCD 4.2.3)

#### Physical design of a coaxial cavity gyrotron

The preliminary coaxial cavity design found in 2013 has been studied in more detail using the interaction codes CAVITY and EURIDICE (see Fig. 1.5.9). The operating point chosen for the simulations was changed to higher current and lower voltage in order to increase the efficiency of the tube. The ohmic loading on the inner conductor is strongly dependent on its dimensions and corrugations and it is still to be understood how much of this is due to physical reasons and how much due to possible numerical issues. Nevertheless, it appears that mode competition is not too severe also for small insert radii; therefore the uncertainty of its dimensions does not affect the basic design and neither the study of other components of that gyrotron design. Also with realistic beam parameters (thickness, spreads), the design appears robust. Multi-particle, multi-mode simulations have been carried out using the HELIOS supercomputer. The general mode selection strategy for very high-order mode gyrotrons, which has been developed based on the design considerations in 2013, has been accepted for publication.

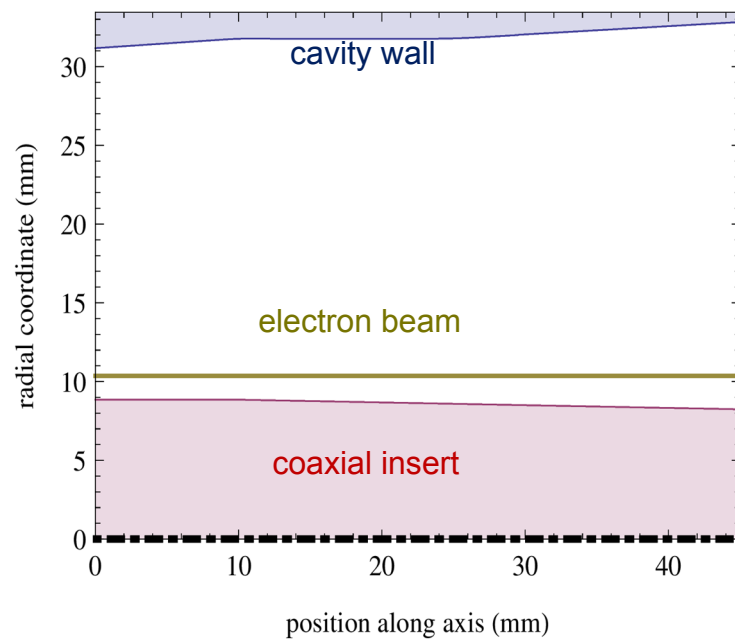


Fig. 1.5.9  
Geometry of cavity wall and coaxial insert, position of the electron beam for the preliminary design.

The routines SCHCHI (searches for possible competing modes) and CHIMP (plots mode eigenvalues over radii ratio between cavity wall and coaxial insert) needed fundamental changes due to limited functionality in very highly overmoded coaxial cavities. This has been addressed by writing a new routine – SCNCHIMP – which combines the essential functions of the two in a natural way and which is more appropriate for modern computing capabilities. Thus, SCNCHIMP can replace SCHCHI and CHIMP in all relevant cases.

Before designing an appropriate magnetron injection gun (MIG), it was necessary to investigate how a realistic magnet for a 240 GHz gyrotron would look like. A first design has been proposed by an industrial manufacturer and used for subsequent MIG studies. These studies focused on the development of a coaxial triode MIG. The current design assumes an emitter radius of 65 mm. Attention has been drawn to low electric fields in the gun region, nonexistence of reflected beam electrons and good overall beam parameters. Ongoing studies take into account the removal of potential wells and secondary electrons.

### **Physical design of a conventional cavity gyrotron**

Initial feasibility study and the fundamental design of a DEMO-compatible (output power  $\sim 1$ -2 MW, efficiency  $>60\%$ ) conventional cavity gyrotron have been initiated. The operating frequencies around 240 GHz have been investigated with the considerations of a slow frequency step-tunability of 30 – 40 GHz for multi-frequency operation and fast frequency tunability of 2-3 GHz. At 236 GHz, the mode  $TE_{43,15}$  is selected for optimization as cavity mode for the DEMO gyrotron. This vacuum tube would also support 170 GHz,  $TE_{31,11}$  mode operation for ITER and could be used for the ECCD system of a pulsed DEMO version at 269 GHz which is currently discussed.

The novel systematic approach has been proposed to finalize the physical parameters of the conventional cavity. These parameters are optimized such that maximum output power and efficiency are achieved with the reasonable ohmic cavity wall loading of 2 kW/cm<sup>2</sup>. The RF behavior of the conventional cavity is verified using the code packages “EURIDICE” and “CAVITY”. Initially, multiple single mode calculations were carried out to finalize the operating parameters of the gyrotron. To verify the effects of competing neighboring modes on the performance of the gyrotron, multi-mode, self-consistent, time dependent calculations have been performed. The result with considering 99 neighboring modes is presented in Fig. 1.5.10. Despite of the considerations of the large number of neighboring modes, the result supports stable output of 830 kW with an electrical efficiency of 38% (without depressed collector) which authenticates the proposed cavity design and the operating parameters.

The performance of the cavity has been further verified by considering realistic electron beam parameters like a velocity spread in the electron beam ( $> 6\%$ ), the beam thickness ( $\sim \lambda/5$ ) etc. The various electron beam spread implementation methodologies have been rigorously analyzed to find out convergence criteria for the realistic beam simulations. The stability of gyrotron operation has been investigated with respect to variation of beam parameters and mechanical tolerances. The design of other components (Magnetron Injection Gun (MIG), quasi-optical launcher and mirror system, depressed collector) for the hollow-cavity 236 GHz DEMO gyrotron are progressing at IHM KIT.

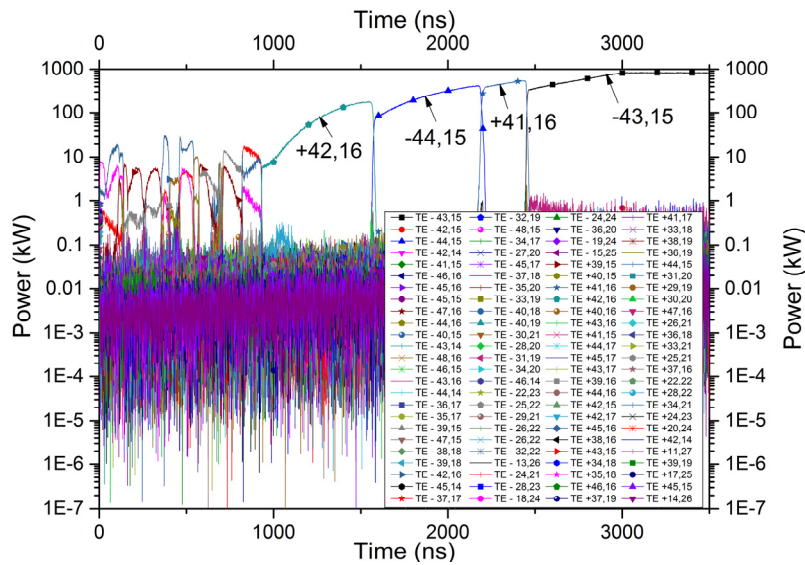


Fig. 1.5.10  
Result of multi-mode self-consistent, time dependent calculations with consideration of a large number of 99 neighbouring modes (TE<sub>43,15</sub> main mode)

#### 1.5.4 Studies on multi-stage collectors for fusion gyrotrons (WP HCD 4.3)

Nowadays, the efficiency of gyrotron beam-wave interaction is typically below 35%. Applying a Single-stage Depressed Collector (SDC) results in 50% overall efficiency in CW operation. Multi-stage Depressed Collectors (MDC) may boost the overall efficiency to a significantly higher level (goal: above 60%), which will not only save operation costs, but will also reduce the requirements on the cooling system of the collector and lower heat stress. The latter also leads to a longer lifetime and higher reliability.

Firstly, the basic requirements of the MDC and its ancillary equipment shall be found out. It includes a basic study of the required voltage range. In order to find out the basic requirement of the power supply, one needs to know:

- the range of electrode voltages in a MDC for the typical fusion gyrotrons
- number of stages
- efficiency improvement

With the above knowledge, a compromise point (or a suitable range) is to be found among the complexity, cost and performance. To answer these questions without a concrete design, one has to consider a general collector model with the following assumptions:

- There is no current between the MDC electrodes.
- Every electron is collected by the optimal electrode.
- The influence of space charge effects is negligible.

A Dynamic Programming (DP) algorithm is used to find the optimal electrodes voltages in  $\mathcal{O}(V^2N)$  time instead of the sweeping  $\mathcal{O}(V^N)$ .  $V$  and  $N$  are the discretization of electron energy and number of stages, respectively.

Taking the gyrotron for W7-X stellarator as an example, the optimal voltages under the ideal assumptions are shown in Fig. 1.5.12 and Table 1.5.4. It can be seen, that the collector efficiency converges to 100%. However, the most evident efficiency improvements are expected for a 2-5 stages collector. The first stage has 30 kV depression instead of 38 kV, which is implied by Fig. 1.5.11, because a small voltage reserve has been added. This 8 kV gap introduces an energy tolerance and allows to capture the slow electrons, which have not been observed in the simulation, but were measured in the experiment. For this reason, the simulated 2-stages collector has a  $\approx 10\%$  lower efficiency than the ideal optimum. Fig. 1.5.11 shows a probability function for the 240 GHz gyrotron under design as well. It is noticeable that the electrons in the 240 GHz gyrotron have more focused energy. The reason for this is that the input electron beam of the cavity simulation is an ideal beam, which does not have any initial space and velocity spread. Therefore its corresponding curve in Fig. 1.5.11 looks more ideal. One can conclude that the both gyrotrons have similar energy probabilities at the entrance of the collector and therefore similar range of electrode voltages, which, for a three-stage MDC is in the range 30 kV – 70 kV.

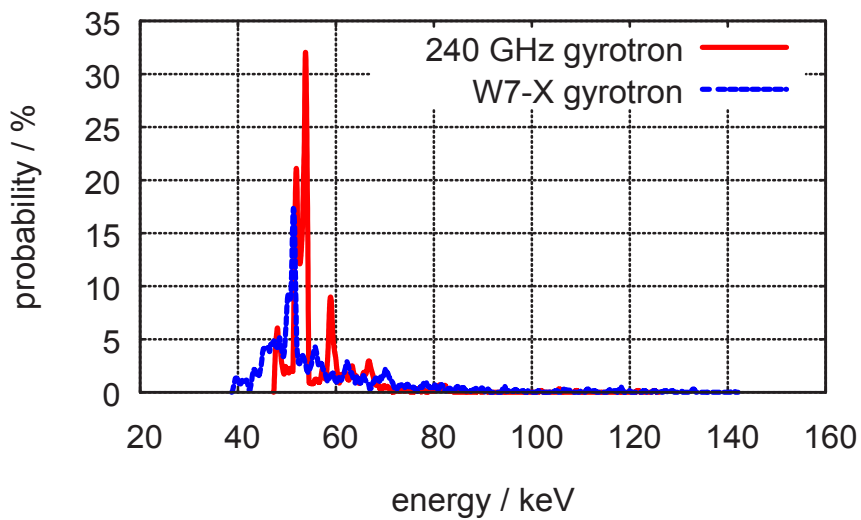


Fig. 1.5.11  
The probability density of the electron energy

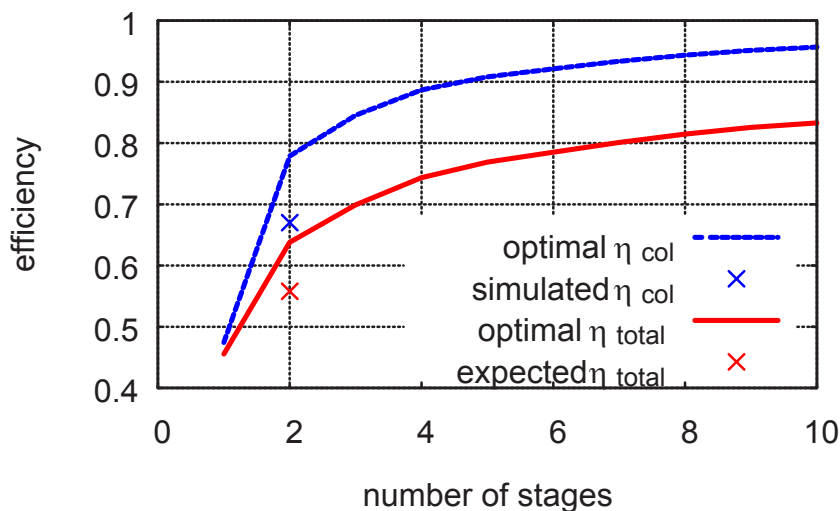


Fig. 1.5.12  
Ideal efficiency for the W7-X gyrotron

<i>No. of stages</i>	<i>Voltage depression /kV</i>							$\eta_{col} / \%$
<i>1</i>	<i>30</i>	-	-	-	-	-	-	<i>47.7</i>
<i>2</i>	<i>30</i>	<i>51.4</i>	-	-	-	-	-	<i>77.9</i>
<i>3</i>	<i>30</i>	<i>50.7</i>	<i>67.3</i>	-	-	-	-	<i>84.5</i>
<i>5</i>	<i>30</i>	<i>48.7</i>	<i>55.7</i>	<i>67.3</i>	<i>83.5</i>	-	-	<i>90.8</i>
<i>7</i>	<i>30</i>	<i>44.9</i>	<i>50.8</i>	<i>55.7</i>	<i>61.3</i>	<i>73.7</i>	<i>77.9</i>	<i>93.3</i>

**Table 1.5.4**  
Optimum collector efficiency in dependence of number of collector stages and optimum voltage depression for the W7-X gyrotron.

## 1.6 Emission uniformity test device for future MIGs

Already in 2013 an emission uniformity test device for magnetron injection guns was built. Firstly, the device allows to measure the temperature distribution at the emitter surface. It is done by an infrared camera which measures the temperatures along the azimuthal angle of the emitter from the outside of a vacuum vessel through a CaF-window. Secondly, the emission distribution of electrons along the azimuthal angle is measured which allows the determination of the homogeneity of the work function. It is performed by small holes with a diameter of 0.8 mm in the anode surface as shown in the figure. Behind these holes electrically isolated probes are installed which measure the current through the holes. The cathode can be rotated continuously. The device operates at a reduced voltage (a few kilovolts), but at the same current density as in gyrotrons.

The figure shows the current measurement of one hole versus the total current to the anode. The ratio describes very well the relation between the areas of the hole to the total anode. From such a measurement the work function of the emitter can be calculated with a spatial resolution of about 0.8 mm.

The device also allows the measurement of the topology of the cathode surface. A distance meter has been installed outside the vessel: By illuminating the cathode surface with a movable laser beam the distance and thus the geometrical homogeneity of the cathode surface can be measured with an accuracy better than 10  $\mu\text{m}$ .

During operation of the device it was found that the cathode could only be rotated up to a temperature of about 700°C. It is assumed that this happens due to the expansion of the ceramical connection between cathode and anode (Fig. 1.6.1). Next step will be an improved design which allows full rotation at operating temperatures up to about 1100°C.

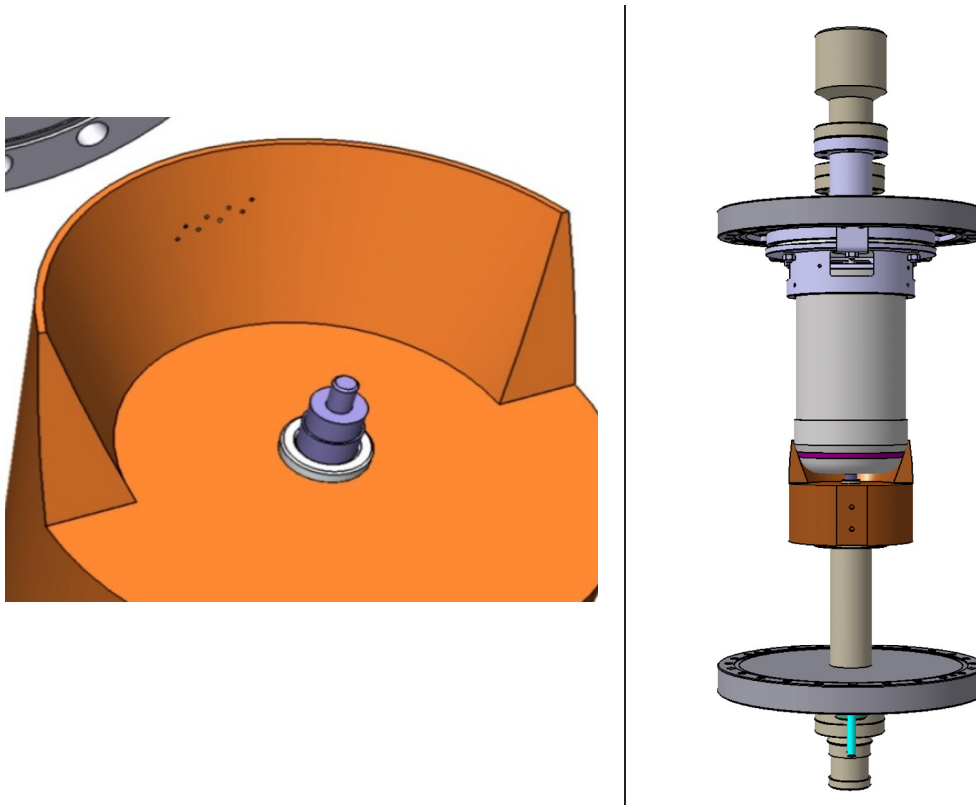


Fig. 1.6.1  
CAD view of test device and detail of anode with sampling holes.

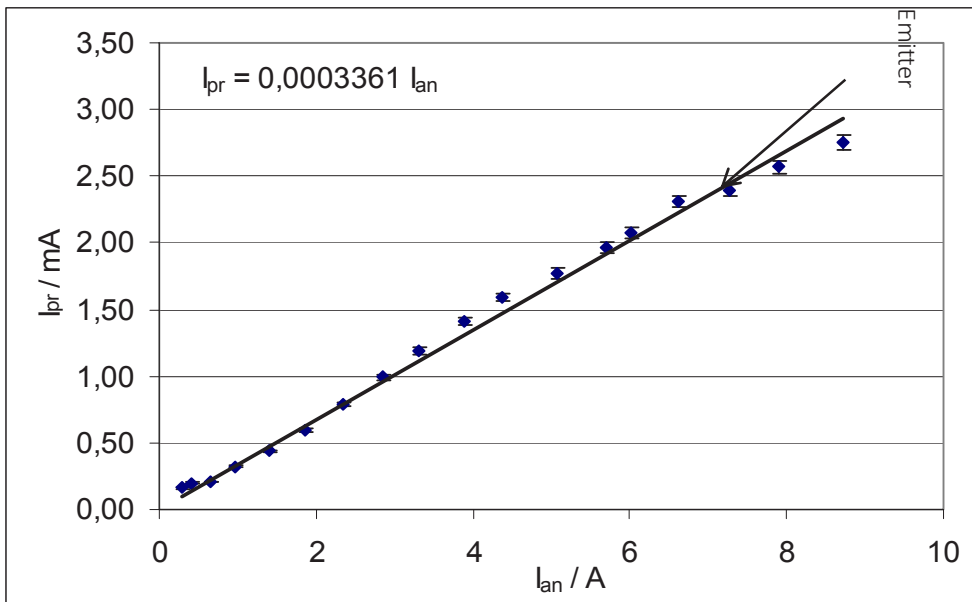


Fig. 1.6.2  
Measurement of current in one hole versus total current to the anode. The proportionality constant corresponds to a diameter of 0.6 mm (design value: 0.8 mm).

## 1.7 Advanced technologies for future high-power gyrotrons

### 1.7.1 Using ferromagnetic material to reduce power densities in collectors

High power CW gyrotrons usually use a sweeping system based on low frequency (5 – 50 Hz) oscillating magnetic fields to spread the spent electron beam on the collector wall. With this measure the average power density on the collector structure can be kept below the critical value of 500 W/cm<sup>2</sup>. Nevertheless, the instantaneous values of the transient peak power density are still quite high (typically of the order of several kW/cm<sup>2</sup>) and due to the cyclic nature of the sweeping, thermal fatigue effects will occur that have a direct impact on the lifetime of the tube. Therefore a method to spread the electron beam in the collector using a static, non-oscillating method would be favorable. In particular in case of a MDC the application of non-oscillating method is mandatory.

A conceptual study with the KIT in-house code ESRAY showed that a ferromagnetic ring around the lower part of the collector could spread the electron beam significantly by introducing a non-adiabatic transition region. In combination with additional small (DC-driven) solenoids and an additional adaption of the shape of the collector wall the maximum power density on the collector structure could be reduced to values below the critical threshold. Fig. 1 shows the widened electron beam trajectories in the optimized collector.

In a next step, the sensitivity of the system on external influences (e.g. magnetic stray fields) has to be investigated.

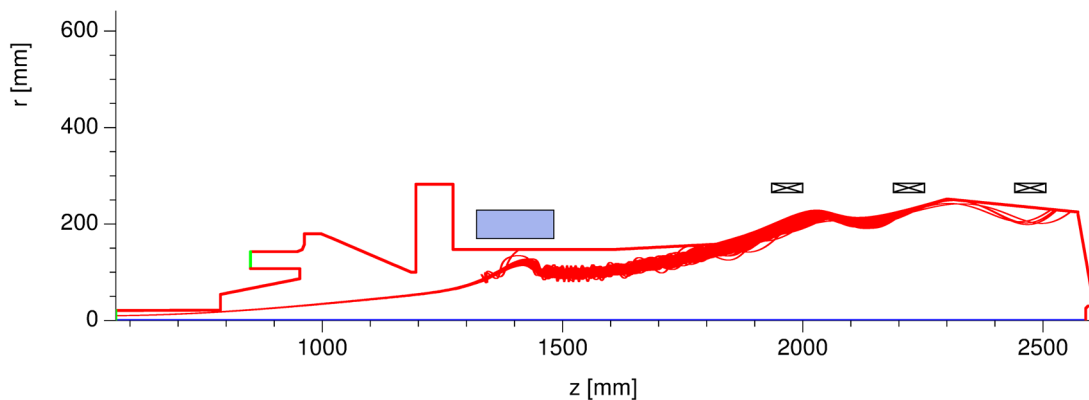


Fig. 1.7.1

Electron beam trajectories (red) in an optimized gyrotron collector equipped with a ferromagnetic ring (lower part, blue color) and three additional correction coils.

### 1.7.2 Experimental investigations of a 20 kW / 28 GHz second harmonic CW gyrotron designed for evaluation of new emitter technologies

A long lifetime of the emitter is one of the key elements in increasing overall lifetime of gyrotrons. Today's Megawatt gyrotrons for fusion applications mostly contain M-type emitters with a typical current density on the emitter surface of just more than 2.5 A/cm<sup>2</sup> and lifetimes less than 10<sup>4</sup> hours. To test radically new emitter technologies a 20 kW / 28 GHz continuous wave (CW) gyrotron (Fig. 1.7.2) operating in the 2<sup>nd</sup> harmonic TE<sub>1,2</sub> cavity mode has been designed and successfully tested. The primary goal is to evaluate

the performance of so-called Controlled-Porosity Reservoir (CPR) emitters. CPR emitters allow operation with significant higher current density (up to 50 A/cm<sup>2</sup>) and provide much longer life times (typical 10<sup>5</sup> hours) compared to conventional emitter materials. In addition, the azimuthally segmented emitter ring allows the generation of controlled non-uniform helical electron beams. Thus, the effect of non-uniform emission on the gyrotron efficiency can be studied systematically in controlled experiments. The tube is equipped with flanges instead of welded connections for easy exchange of the components.

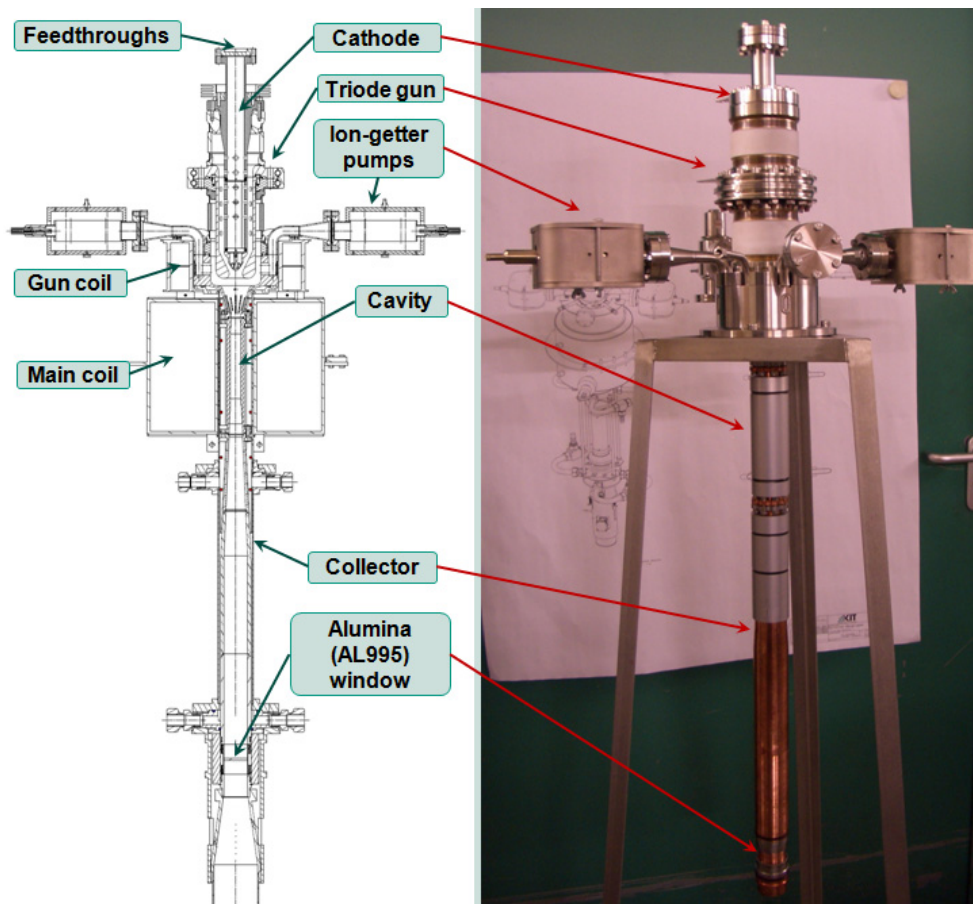


Fig. 1.7.2  
Sketch and photograph of the 15 kW/28 GHz CW gyrotron.

The design of the triode-type electron gun and the collector (non-depressed collector operation) was optimized using the KIT in-house code ESRAY and the three-dimensional code Ariadne. Non-stationary cavity simulations with multi-mode competition with different operating beam parameters have been performed using the self-consistent EURIDICE code.

The CPR type emitter ring is azimuthally subdivided in twelve segments. The emitted current from each segment can be independently controlled using the individual filament heating power. The cathode design with the segmented emitter ring and a drawing of a single segment are shown in Fig. 1.7.3. An individual segment (Fig. 1.7.4) consists of the heater, the barium reservoir and the emitter which is made from sintered tungsten wires. Barium diffuses to the emitter surface through channels which are created during the sintering process.

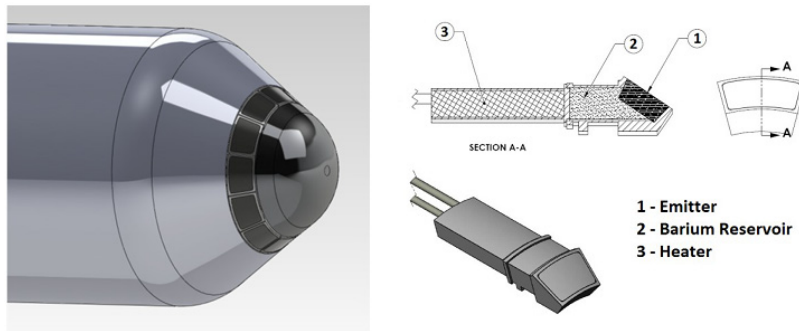


Fig. 1.7.3  
CPR cathode with segmented emitter ring and drawing of an individual segment.

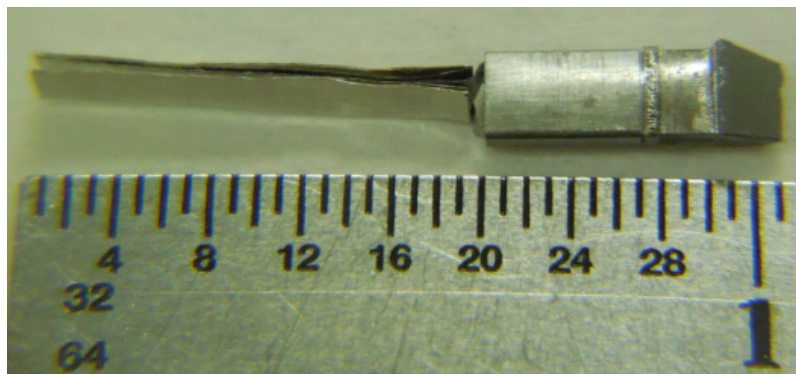


Fig. 1.7.4  
Photograph of a single CPR emitter segment (length=10mm).



Fig. 1.7.5  
Photograph of the 15kW/28GHz CW gyrotron installed at the test stand.

In a first step, for reference, a conventional M-type emitter with a current density of  $J = 2.5 - 3 \text{ A/cm}^2$  has been designed and tested. The test set-up together with the installed gyrotron is shown in Fig. 1.7.5. A triode type magnetron injection gun (MIG) is used, in order to increase the range of operating parameters. Experiments showed stable 2nd harmonic operation in a wide range of electron beam parameters. The competing fundamental TE<sub>1,1</sub>-mode operating as backward wave is well suppressed. The measured frequency  $f = 28.03 \text{ GHz}$  corresponds very well to the theoretical simulations. Stable electron gun operation has been observed in a wide range of beam currents from  $I_b = 0.5 \text{ A}$  to  $I_b = 2.3 \text{ A}$  as well as in a wide range of the modulation anode voltage.

Several CW regimes are listed below:

- 1)  $U=23.4\text{kV}$ ,  $I=2.23\text{A}$ ,  $P=22.5\text{kW}$ ,  $\eta=43\%$  (high efficiency, high voltage operation)
- 2)  $U=21.8\text{kV}$ ,  $I=2.24\text{A}$ ,  $P=19\text{kW}$ ,  $\eta=39\%$  (high current operation)
- 3)  $U=20.6\text{kV}$ ,  $I=1.02\text{A}$ ,  $P=7.6\text{kW}$ ,  $\eta=36\%$  (low current regime ( $j_{\text{emitter}}=1.2\text{A/cm}^2$ ), long lifetime of M-type emitter)

In Fig. 1.7.6 an example of CW beam current, voltage, power and vacuum traces are shown. A world record for the efficiency of 2nd harmonic gyrotrons has been achieved. Additional experiments are planned in 2015 after delivery of the CPR cathode.

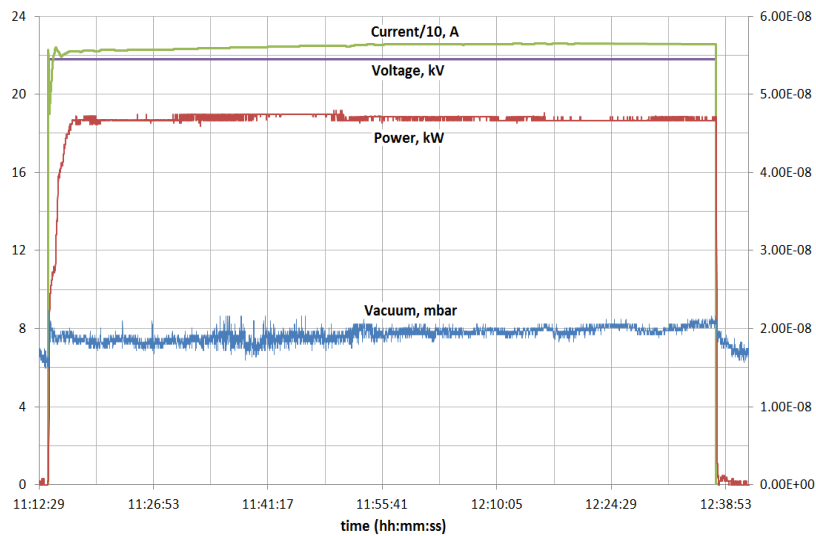


**Fig. 1.7.6**  
Beam current, voltage, power and vacuum traces of a typical CW pulse.

### 1.7.3 Thermo-mechanical studies of gyrotron cavities

Thermo-mechanical modelling of the gyrotron cavity and pertinent studies of existing high-power gyrotrons have been performed, continuing the work initiated in the previous period. For the simulations of the thermal stresses, the multi-physics, finite-element software COMSOL was used. In support to that, the simulations of the gyrotron operation were performed with the in-house code-package EURIDICE. The performed work included: (i) Creation of a MATLAB code (using LiveLink MATLAB) to provide automatic coupling of

EURIDICE and COMSOL, and to implement realistic, axially dependent electrical conductivity of the cavity wall, as well as time-dependent neutralisation of the beam space charge. (ii) Parametric studies on the existing 170 GHz, 2 MW short-pulse coaxial gyrotron with uncooled cavity wall and cooled insert, in order to estimate the maximum pulse length before plastic deformation of the resonator. Examining parametrically the influence of Young's modulus, roughness coefficient and wall thickness, this limit was found to be around 40 ms. (iii) Studies of the 140 GHz, 1 MW CW gyrotron for W7-X and comparison of simulation results with experimental data, in order to get a better estimation of the heat transfer coefficient  $h$  and the surface roughness coefficient  $k$ . The newly obtained estimations  $h = 55 \text{ kW}/(\text{m}^2\text{K})$  and  $k = 1.3$  differ significantly from the previously considered values  $h = 130 \text{ kW}/(\text{m}^2\text{K})$  and  $k = 1.5$ . This requires additional clarification by future, dedicated experiments.

#### 1.7.4 Investigation on Secondary Electron Emission Models

Secondary electrons which are generated during the operation of a gyrotron will decrease the gyrotron efficiency and stability. Bombardment of electrons on the wall of single or multi stage depressed collector will generate secondary electrons which will decrease the collector efficiency. Secondary electrons can also be generated in the magnetron injection gun by the bombardment of back reflected trapped electrons on the cathode surface. These additional electrons from the cathode surface have a bigger probability to be trapped again and the accumulation of the trapped electrons can cause low frequency oscillation (LFO) in the gyrotron. In order to investigate the influence of secondary electrons a secondary electron emission model as is shown in Fig. 1.7.7 has been developed and has been implemented in the KIT in-house codes ESPIC & ESRAY for different kinds of gyrotron-relevant materials. First results are expected in 2015.

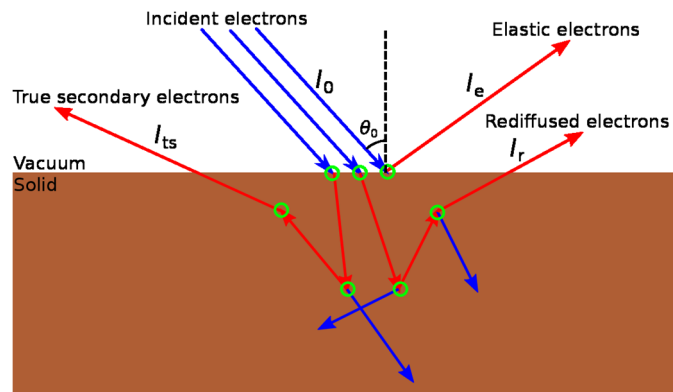


Fig. 1.7.7 Sketch of secondary electron emission showing the different types of secondaries.

#### 1.7.5 Evaluation of Gyrotron Cathode Emission Inhomogeneity

The emission inhomogeneity of the gyrotron emitter will increase the velocity spread of the electron beam and thereby will decrease the gyrotron efficiency. Measurement of the Current-Voltage Characteristics is a simple and fast method to calculate the emission inhomogeneity. As an example, we show in Fig. 1.7.8 and Table 1 measured and calculated results for a 28 GHz / 20 kW gyrotron for materials processing. The values  $W_0$ ,  $T$  and  $\sigma_w$  are the average work function, temperature and standard deviation of the work function distribution of the emitter, obtained from a statistical analysis of the measurement data. Since  $\sigma_w$  is around 0.026 eV the emitter has a nice emission uniformity.

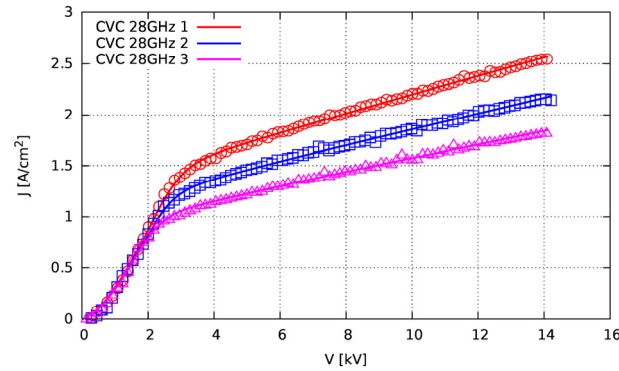


Fig. 1.7.8  
Current-Voltage characteristics of the 28GHz gyrotron, obtained for three different values of the heater power.

<i>Curve</i>	<i><math>W_0</math> [eV]</i>	<i><math>T</math> [°C]</i>	<i><math>\sigma_w</math> [eV]</i>
<i>CVC 28GHz 1</i>	<i>1.85</i>	<i>899.8</i>	<i>0.0248</i>
<i>CVC 28GHz 2</i>	<i>1.85</i>	<i>890.0</i>	<i>0.0261</i>
<i>CVC 28GHz 3</i>	<i>1.85</i>	<i>879.9</i>	<i>0.0294</i>

Table 1.7.1  
Calculated emission parameters obtained from the measured current-voltage characteristics

## 1.8 FULGOR (Fusion Long-Pulse Gyrotron Laboratory)

The existing gyrotron test facility at KIT, which had been designed and built about 30 years ago, plays a worldwide leading role in the development of high-power gyrotrons for nuclear fusion applications. This facility offered the unique opportunity to develop and test the first CW high power series gyrotrons for the stellarator W7-X in collaboration with IPP and Thales Electron Devices as the industrial partner.

The target parameters of the new gyrotron test facility are well beyond the capabilities of the existing one. The new teststand will strongly support KIT's leading role in the development of advanced gyrotrons. It will help to answer the questions regarding the technical limits and new physical designs for future high-power microwave tubes. The key parameters of FULGOR will be:

- Full CW operation with up to 10 MW electrical power, corresponding to  $\geq 4$  MW RF power (assuming an efficiency of the gyrotron  $\geq 40\%$ )
- Support of advanced energy recovery concepts, e.g. multi-stage depressed collector (MSDC)

The high voltage power supply (HVPS) will support an operating voltage of up to 130 kV with up to 120 A beam current. A superconducting magnet which allows operation of gyrotrons at frequencies well above 200 GHz will be a major component of FULGOR. Other significant components of the teststand will be: cooling system, control electronics and interlock system, RF diagnostics including high-power RF absorber loads.

The capabilities of FULGOR will enable the development of gyrotrons for future fusion machines like ITER and DEMO. Fig. 1.8.1 is a simplified CAD view of the complete FULGOR system.

In 2014 the specifications of the HVPS has been defined and an international call for tender has been launched. After careful assessment of the offers a contract was awarded end of 2014.

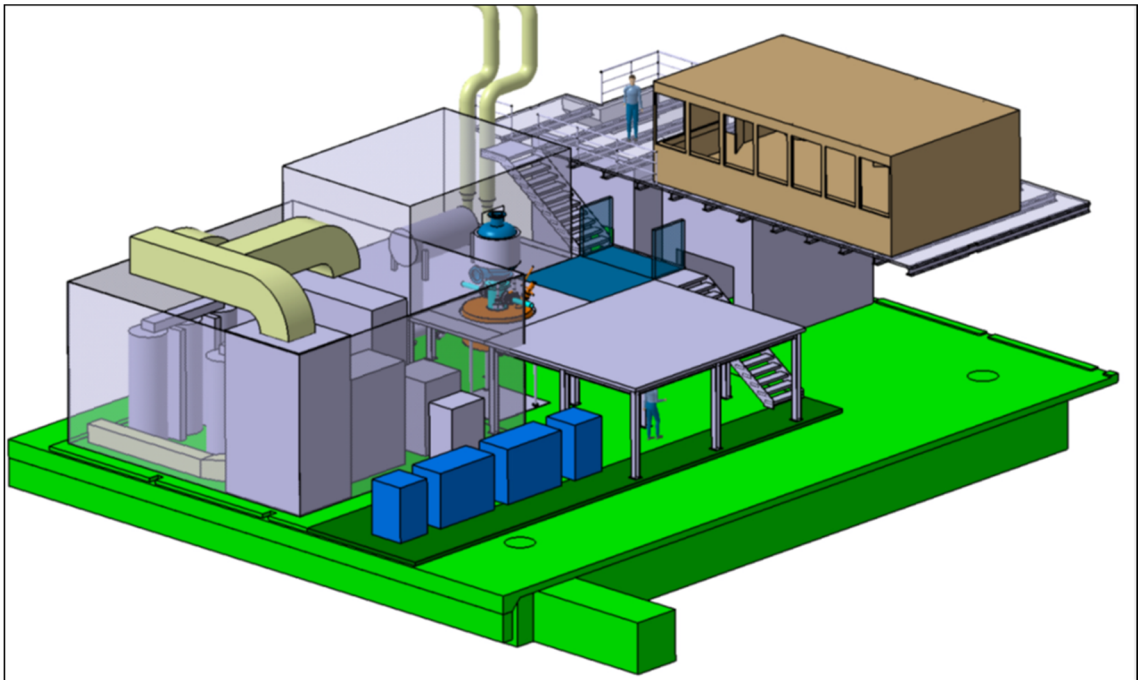


**Fig. 1.8.1**  
CAD view of FULGOR installation including control room.

## 1.9 Launcher Handling and Testing facility LHT

The Launcher Handling and Testing facility for the ITER ECRH Upper Launcher consists of a prototype test bed for the structural launcher components, like single wall, double wall and blanket shield module (BSM - incl. first wall panel (FWP)). It provides a water circuit with a large range of temperatures and pressures up to ITER bake out (max. 240°C at 4.4 MPa) and the ability to apply fast thermal transients. An experimental verification of normal and baking conditions in ITER can be simulated in a real scenario. In the past year the facility was extended significantly in the frame of a BMBF project with a large vacuum vessel, control system and an attached mass spectrometer for high resolution measurements of outgassing properties of tested components depending on their manufacturing route. In its current state the facility is ready for the foreseen Prototyping and Testing (P&T) contracts in the frame of the ITER ECRH Upper Launcher development program with the European domestic agency F4E. Existing prototypes at KIT, mentioned above, are now ready for thermohydraulic measurements. In the vacuum vessel special connection flanges are foreseen for heating and cooling of the launcher components under high vacuum conditions  $p < 10^{-9}$  mbar. To choose the right manufacturing route for that kind of components, the outgassing values have to fulfill the vacuum requirements. A comparison of hipped (hot isostatic pressed) or forged and casted structures will be carried out. To reach the necessary low vacuum pressure, the vacuum vessel can be heated as seen in the right picture to degas the inside surface of the vessel.



Fig. 1.9.1  
 Launcher Handling Test Facility Vacuum System and Prototype Testing (here the single wall prototype)

**Involved Staff:**

**KIT/IHM**

K. Baumann  
 Dr. B. Bazylev  
 Dr. G. Dammertz  
 J. Franck  
 M. Fuchs  
 Dr. G. Gantenbein  
 Dr. H. Hunger  
 Dr. Yu. Igitkhanov  
 Dr. S. Illy  
 Prof. J. Jelonnek  
 Dr. J. Jin  
 Th. Kobarg  
 Dr. I. Landman  
 R. Lang  
 W. Leonhardt  
 M. Losert  
 A. Malygin  
 D. Mellein  
 A. Meier (KIT, IAM-AWP)  
 Dr. I. Pagonakis  
 A. Papenfuß  
 K. Parth  
 Dr. S. Peschanyi  
 Dr. B. Piosczyk  
 S. Ruess (KIT CS)  
 Dr. T. Rzesnicki  
 Dr. A. Samartsev  
 Dr. Theo A. Scherer  
 (KIT, IAM-AWP)  
 A. Schlaich (KIT CS)  
 M. Schmid  
 W. Spiess  
 Dr. D. Strauss (KIT, IAW-AWP)  
 Prof. M. Thumm

S. Wadle  
 J. Weggen  
 Ch. Wu  
 J. Zhang  
 (Diploma/Master students)  
 R. Cubizolles  
 V. Kamra (DAAD)

**IPF (University of Stuttgart)**

Dr. W. Kasperek  
 C. Lechte  
 R. Munk  
 Dr. B. Plaum  
 F. Rempel  
 H. Röhlinger  
 P. Salzmann  
 K.H. Schlüter  
 S. Wolf  
 A. Zeitler

**IPP (Greifswald/Garching)**

B. Berndt  
 Dr. H. Braune  
 Dr. V. Erckmann (PMW)  
 F. Hollmann  
 L. Jonitz  
 Dr. H. Laqua  
 Dr. S. Marsen  
 F. Noke  
 M. Preynas  
 F. Purps  
 A. Reintrog  
 T. Schulz  
 T. Stange  
 P. Uhren  
 M. Weißgerber

## **2 HGF Program: Energy, Topic Renewable Energy**

### **2.1 Overview**

As an important step towards pilot-scale pulsed electric field (PEF) processing, the out-door photobioreactor for microalgae biomass production went into operation. After three initial cultivation runs it can be summarized that the facility fulfills the intended requirements.

With regard to pilot PEF-processing electrode erosion measurements were started which indicate, that long pulses do not increase electrode erosion rate. This allows extending parameter studies to long pulse protocols providing a given treatment energy at lower pulse repetition rates.

It could be demonstrated that nsPEF stimulation of microalgae can trigger Astaxanthin induction in *H. pluvialis*, whereas the effect of nsPEF on lipid production was adverse.

Measurements on the required field strength for membrane permeabilization indicate an exponential decrease of the required electric field strength with increasing pulse duration.

#### **2.1.1 Construction and Operation of the new 1000 l photobioreactor “PBR1000”**

After demolition of the former greenhouse next to building 630 of the IHM in 2013, the construction of the new out-door algae cultivation facility, called PBR1000, was completed in summer 2014. The primary objectives to be obtained with this installation are to produce sufficient biomass for pilot-scale PEF-processing and to optimize cultivation protocols with regard to improve processability by pulsed electric fields aiming to lower energy demand and increased product extraction yields.

The photobioreactor exhibits a total cultivation volume of 1000 liters and is composed of 5 independent flat panels, each 6 meters long and 1 m high. The algae grow in transparent plastic sacks, supported on both sides by metallic fences. Aeration through a porous tube at the bottom of each panel supplies the algae with CO<sub>2</sub> and prevents them from sedimentation. Each panel allows independent control of temperature, pH and foam-formation. In front of the 5 main panels, a smaller panel was added, which is used for the production of microalgae as starter-culture for the large panels. A container was placed next to the bioreactor. It houses the control and acquisition systems for temperature, pH, foam formation and total radiation. All parameters are computer-controlled via software based on LabView and can be accessed by internet.



Fig. 2.1.1

Out-door photobioreactor "PBR 1000" in operation. Five cultivation panels can be controlled and operated separately. The small panel is for cultivation of the starter culture for the larger panels. Measurement and control equipment is installed in the blue container behind the panels. Auxillary equipment, e.g. centrifuge, water tanks, compressor unit are stored in the fenced rear area.

In cooperation with the Institute of Process Engineering in Life Sciences, Section III Bioprocess Engineering, three different cultivations of the microalgae *Chlorella vulgaris* were carried out starting in August 2014. The goal of the first cultivation was the characterization of typical parameters and the validation of the whole system. During the first cultivation, specific values as gassing rate (0,05 vvm), mixing time (9 minutes), and settings for the pH-control were determined. An average photoconversion efficiency of 2,89% (PAR-spectrum) and an average biomass productivity of 0,33 g/l/d could be achieved.

A second cultivation was performed to test different temperature control strategies with regard to productivity and growth. It could be shown that cooling of the photobioreactor system did not have a significant effect on the microalgae growth for this year's weather conditions in late summer time.

The last cultivation was run to analyze the influence of reflecting and absorbing sheetings on the facility's ground on growth. Covering the facility's ground between the panels by reflecting foils lead to a higher value of productivity and photoconversion efficiency compared to a reference reactor which was operated without changes on ground reflexion.

The biomass from the new reactor was used for the cell disintegration experiments with the PEF treatment. The harvest of the large amount of microalgae biomass emerged to be difficult. The existing centrifuge was – in contrast to the manufacturers specifications - unable to cope with the volume of algae suspension. As continuous harvesting was impossible under the given conditions, the harvest had to be done in steps of 25 liters – a very time consuming procedure. The intended use of the produced biomass is the upscale from laboratory to pilot scale of PEF treatment procedures. This requires several hundreds of liters of concentrated suspension. So the harvest equipment definitely needs to be optimized in the near future.

An important parameter in PEF-processing of biomass is the conductivity of the treated suspension. As the applied electrical energy is directly correlated to the conductivity of the samples, the content of salts in the

algae media should be kept low. Currently, the automatic pH-setting is done with NaOH as set-up agent. This leads to typical conductivity values of 4 mS/cm at the end of the cultivation period. The replacement of NaOH by NH<sub>3</sub> could result in lower conductivity and reduce energy consumption during PEF treatment.

### 2.1.2 Correlation between electrode erosion and pulse duration due to Pulsed Electric Field (PEF) treatment

In Pulsed Electric Field (PEF) - applications electrode wear needs to be investigated, particularly, when long term operation is objected. In literature it is stated, that the loss of electrode mass correlates with the impulse duration. For longer pulses a higher electrode erosion rate was predicted. To study the electrode abrasion as a function of pulse duration ( $t_{imp}$ ) different values of  $t_{imp}=1 / 10 / 100 \mu s$  were investigated. Disk-shaped stainless steel electrodes, embedded into a polycarbonate continuous-flow cell were used with a CaCl<sub>2</sub>-electrolyte medium adjusted to an electrical conductivity of 1350  $\mu S/cm$ , corresponding to the electrical conductivity of common microalgae suspensions.

The chosen specific energy input,  $W_{spec}=50kJ/kg$  and flow-rate  $Q=0.1 \times 10^{-3} kg/s$  were kept constant for almost all experiments. For an additional parameter set, the treatment energy was doubled to  $W_{spec}=100kJ/kg$ . Rectangular pulses were supplied by an IGBT-switched single stage pulse generator. The process parameters and erosion rates are summarized in Table 2.1.1.

$W_{spec} [kJ/kg]$	50	50	50	100
$U [V]$	1000	800	500	500
$E_{cell} [kV/cm]$	5	4	2.5	2.5
$t_{imp} [10^{-6}s]$	1	10	100	100
$f_{rep} [1/s]$	357	56	14.3	28.6
$\Delta m_{electrode} [10^{-3}kg]$	0.0544	0.0611	0.0415	0.0733

**Table 2.1.1**  
Pulse parameter and electrode erosion during PEF-treatment.

It was found, that electrode erosion caused by PEF treatment doesn't increase with pulse duration, when specific energy input is kept constant. Furthermore, it was shown that the erosion rate scales linearly with treatment energy, Fig. 2.1.2.

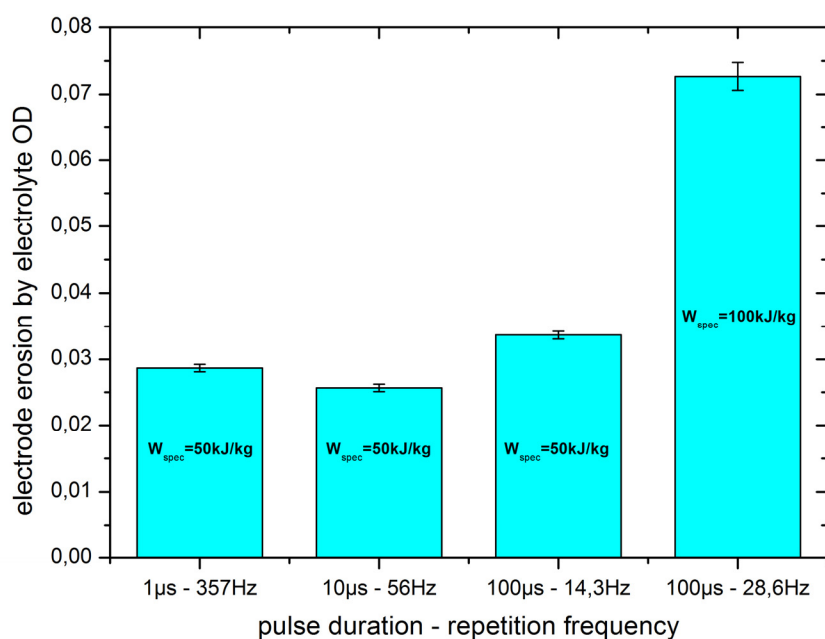


Fig. 2.1.2  
Electrode erosion by PEF-treatment with changing pulse duration, evaluated by optical density (OD) of the treated process electrolyte.

### 2.1.3 Stimulation of algae growth by nanosecond pulsed electric fields

The aim of this study, which is supported by the Baden-Württemberg Foundation, was to stimulate microalgae proliferation by using nanosecond pulsed electric field (nsPEF) treatment to increase the productivity of microalgae cultivation. In our previous study it was demonstrated phenomenologically that nsPEF treatment of seedlings of *Arabidopsis thaliana* induces growth stimulation on plants. Main objective of this project was to develop a procedure on a bench scale, which demonstrates the increased productivity of microalgae cultivation by combining the optimal nsPEF treatment protocol with the best cultivation strategy. In the first part of this study an accelerated growth of *Chlamydomonas reinhardtii* when cultivated in combination with a plant growth hormone and stimulated by nsPEF treatment was found. In the course of the project the focus of our study switched on identification and testing of further additives (phytohormone) which enhance algae proliferation and are environmentally acceptable. The mode of action of plant hormone on algae growth was investigated in collaboration with Botanical Institute I. at Campus South while the effect of nsPEF treatment with and without additives was verified experimentally at IHM. To complement the results obtained with *C. reinhardtii* at Botanical Institute, the effect of the selected additives on *Chlorella vulgaris* growth was examined. For this second microalgae species, it was found that both nsPEF treatment, as well as the simple addition of active compounds has a slight effect on cell growth after three day of cultivation.

#### Verification of the growth stimulation effect by nsPEF treatment on *C. vulgaris* cultivated in 1-liter-photobioreactor

In order to investigate the effect of nsPEF on algae growth under bioprocess cultivation conditions a 1-liter-photo bioreactor with LED illumination and pH control was designed by BVT during the last part of the project. For the same purpose a mobile pulse generator was designed and tested for continuous operation at IHM. The ns-pulse generator delivers pulses with durations of 25 ns, 50 ns and 100 ns with a repetition

frequency up to 10 Hz. The pulse generator was designed to be operated in combination with a 1-liter-photo bioreactor in order to prove the effect of nsPEF treatment on algae growth on an upscale system, see Fig. 2.1.3. Two 1-liter-photobioreactors were operated in parallel. One reactor was connected to a continuous flow nsPEF treatment chamber whereas the second reactor served for control cultivation without nsPEF treatment. *C. vulgaris* was cultivated under controlled conditions by adjusting CO<sub>2</sub> concentration, pH and illumination.

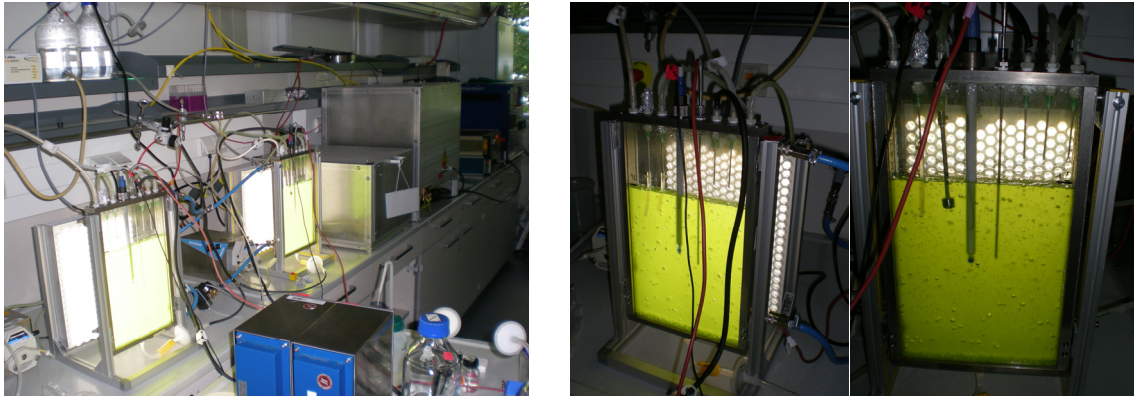


Fig. 2.1.3  
Experimental setup of 1-liter-photo bioreactor with integrated pulse generator

The nsPEF treatments with a specific energy input of 100 J·kg<sup>-1</sup> were performed daily. The course of the dry biomass (BTM) of both suspensions and the time of medium exchange and nsPEF treatment (tagged by asterisks) are shown in Fig. 2.1.4. The growth rates of both suspensions behave similar until the 3<sup>rd</sup> day of cultivation. A slight increase of the optical density and dry biomass could be observed after this time.

In summary, the specific energy input of 1 J·g<sup>-1</sup> necessary to induce an increased biomass yield by nsPEF treatment was rather low. Furthermore, the required minimum growth rate of 3.5%, which compensate the energy consumption, could be exceeded. From a technical point of view, the nsPEF method is able to influence the balance of the overall process positively. However, the operating efficiency is reduced dramatically if the investment and operating costs of a PEF unit are considered.

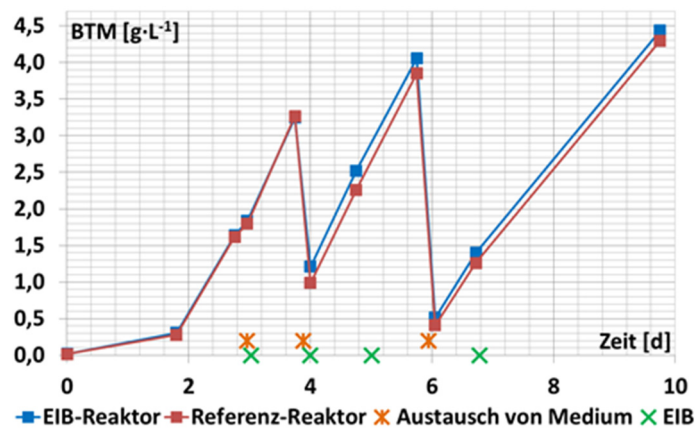


Fig. 2.1.4  
The dry biomass for nsPEF treated microalgae suspension (blue) and reference suspension (red) over the course of time. The time of medium exchange and nsPEF treatment are indicated by yellow and green asterisks, respectively.

### Effect of nsPEF treatment on algal oil and astaxanthin accumulation

The effect of nsPEF treatment on algal oil and astaxanthin accumulation was examined in a master thesis. It is a fact that some algae under abiotic stress exposure, such as nitrogen starvation, are accumulating lipids, typically triglycerides, as an energy reserve. The aim of this study was to replace the typical abiotic stress by nsPEF treatment. The advantage of the nsPEF treatment is that the intensity and the starting point of the exposure can be controlled. Primarily the cultivation time until the oil peak is reached was determined. This is considered the main parameter necessary to investigate whether or not the nsPEF treatment influences the algal oil accumulation. For this purpose, a fluorescence method based on the dye Nile red, which stains intracellular lipid droplets, was used.

In summary, it can be stated that the oil accumulation started during the exponential growth phase, 48 h after inoculation and reached the maximum of oil content after 3-4 days. In general, during the first 4 d, the treated and untreated algae culture grew similar. However, during the following days the cell number of the reference samples started to progressively increase more than PEF treatment samples while the OD-curves were rather superimposed. Both samples reached the stationary growth phase after 5 d of cultivation. In contrast, the growth rate of the cell density of the PEF treatment samples was higher than reference sample. As we observed from the fluorescence intensity of Nile red emission over 11 d, the oil accumulation in the PEF-treated samples was slightly inhibited. Within the tested parameter range an increase of oil accumulation by nsPEF-treatment could not be ascertained.

Besides the algal oil accumulation, the possibility to trigger the transition of *Haematococcus pluvialis* algae from the green stage (vegetative stage) to red stage (astaxanthin rich aplanospores) was examined. During exposure to adverse environmental conditions, such as high light intensity, salinity or nutrient deficiency the cell morphology of *H. pluvialis* change considerably. These morphological changes can be identified by microscopically analysis. The following microscopically images (Fig. 2.1.5) shows the reference and nsPEF treated samples of *H. pluvialis* 7 d and 8 d after cell inoculation. The nsPEF treatment was performed after the 6<sup>th</sup> d, during the exponential growth phase of *H. pluvialis*. The microscopic images of *H. pluvialis* captured 24 h and 48 h after nsPEF treatment show modified organelles and a slight color switch toward red on. Considering this observations we can conclude that the nsPEF treatment caused an abiotic stress, which is able to initiate the transition of *H. pluvialis* from the green stage to an astaxanthin production stage. This effect will be further investigated in the course of a PhD thesis in collaboration with Botanic Institute I. at Campus South.

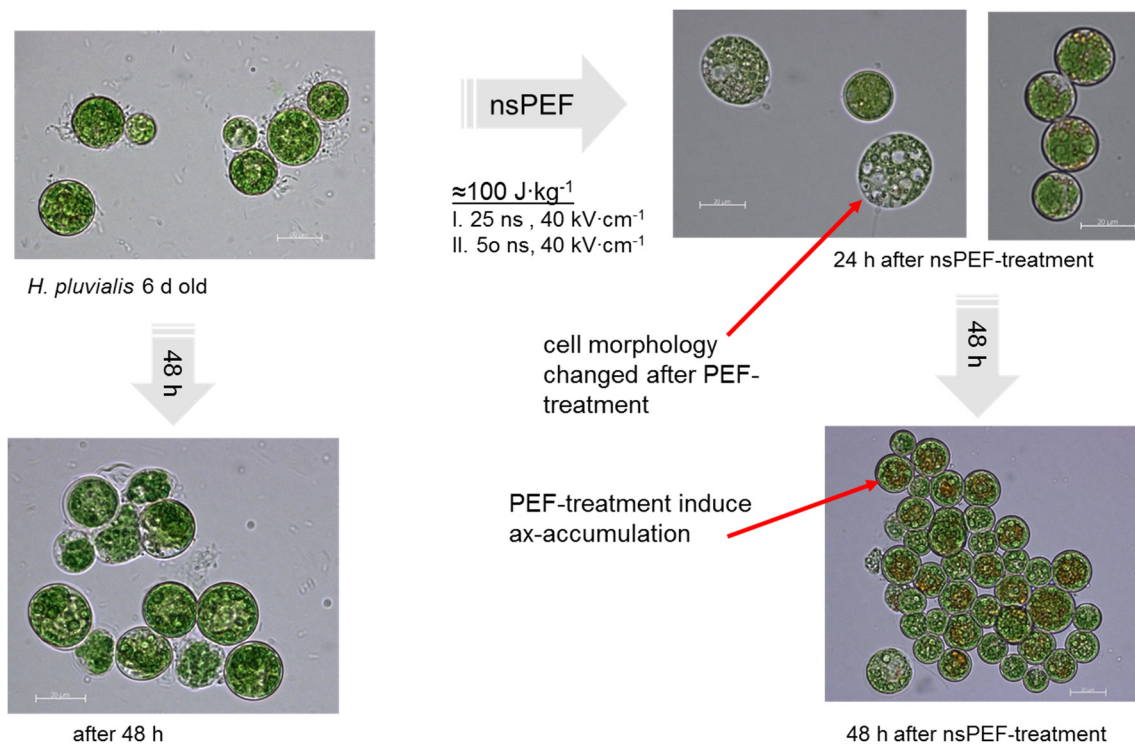


Fig. 2.1.5 Images of *H. pluvialis* algae during cultivation with and without nsPEF treatment: left reference sample and right nsPEF treated sample.

#### 2.1.4 Measurements of the cellular membrane conductance reflect the dynamics and voltage dependence of electric-field-induced pore formation

Exposure of cells and tissues to pulsed electric fields leads to a transient or persistent permeabilisation of the cellular membrane, an effect that is exploited in many ways in biotechnology and biomedicine. Membrane permeabilisation is most sensitively and precisely monitored by measuring the membrane conductance. Under physiological conditions, the membrane is a very low-conductive diffusion barrier ( $<1 \text{ mS cm}^{-2}$ ) that keeps valuable molecules inside the cells while potentially harmful substances at the cell surface are excluded from uptake. However, when the membrane is polarized beyond certain threshold voltages (about  $-250\text{mV}$  and  $+200\text{mV}$ , respectively), the trans-membrane electric current increases in a highly non-linear manner, most likely due to the spontaneous formation of aqueous membrane pores that facilitate the passage of ions. Usually, the pores start to close once the voltage difference across the membrane,  $U_M$ , is returned to a less extreme value that does not support pore formation. This is most conveniently studied by applying the whole cell configuration of the patch clamp technique. A fine-tipped glass microcapillary filled with electrolyte solution and containing an Ag/AgCl electrode is used to establish a relatively low-resistance access to the cell interior. Using a sophisticated patch clamp amplifier, a defined, homogenous voltage can be imposed on the membrane artificially, and the current elicited by this voltage pulse can be monitored. An typical example for such a recording is shown in the Fig. 2.1.6. An 5-ms positive-going voltage step from 0 mV to 293 mV imposed on a DC-3F culture cell (a cell line commonly used in electroporation research that was originally derived from hamster lung cells) elicited a characteristic current response comprising of a capacitive current spike and, upon the decay of this transient, a subsequent, slow current increase until the end of the pulse which was apparently due to aqueous pore formation. Subsequently, the

low-conductance state of the membrane was recovered by stepping the membrane voltage to a much lower level (146 mV) for 100 ms. Pore closure was directly reflected by the kinetics of trans-membrane current relaxation. The time course was well described by an exponential function of the form  $I = I_0 \cdot \exp(-t/\tau)$ . Best fit rendered a time constant  $\tau$  of 19.9 ms, indicating that the pores closed within about 100 ms, and the initial, low conductance state of the membrane was recovered. This time course is roughly in agreement with experimental data found in the literature, whereas molecular dynamics simulations predicted a much faster pore closure. The reason for this discrepancy remains unknown. When pulses of various amplitudes and polarity are successively applied, a current-voltage relation of the membrane can be assessed by plotting the current level at the end of each pulse against the corresponding trans-membrane voltage difference. An example obtained on a protoplast (a plant cell, in this case a ,bright yellow 2' (BY-2) tobacco culture cell, after removal of the cell wall matrix) is shown in Fig. 2.1.6. The current-voltage curve allows to infer the membrane conductance as a function of voltage. However, in principle there are two ways of doing so (known from the literature on the analysis of voltage-gated ion channels): The so-called *slope conductance* represents the first derivative of the current-voltage curve,  $dI/dU_M$ . This parameter contains little information on the underlying process of pore formation and the physical mechanisms involved. A more useful parameter is the so-called *chord conductance* ( $G_{\text{chord}}$ ). For every point on the current-voltage curve, the current level is divided by the respective membrane voltage. Zero voltage is set to the potential at which no current passes through the pores (reversal potential,  $E_{\text{rev}}$ ; note that  $E_{\text{rev}}$  deviates from zero voltage when the pores possess a change towards cations or anions):

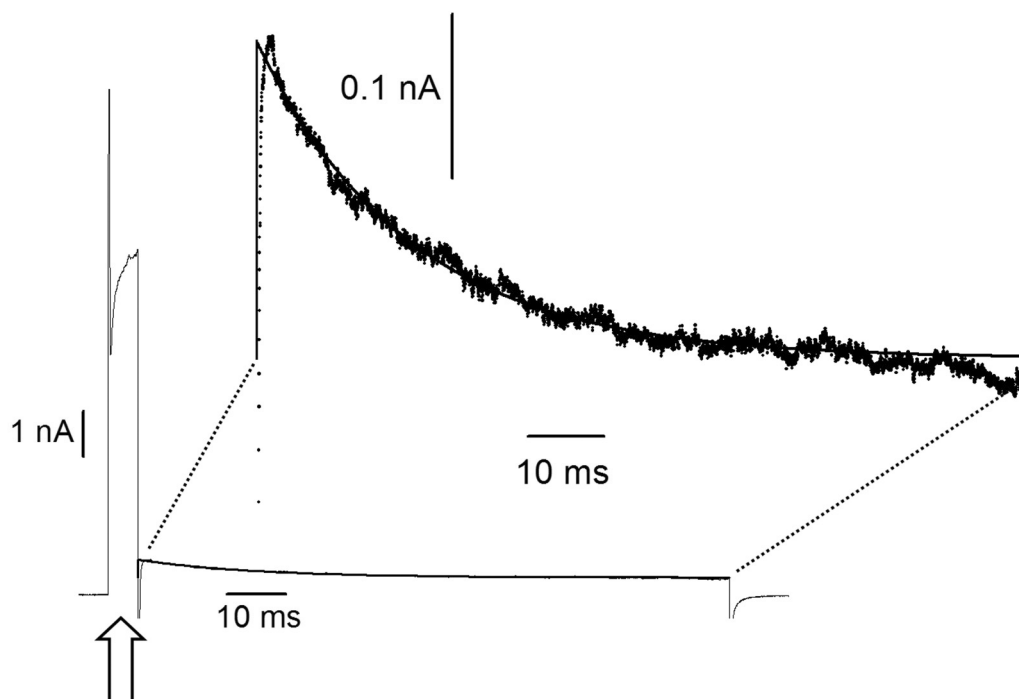


Fig. 2.1.6

Fig. 6: Current response to a 5-ms porating pulse from 0 to 293 mV (arrow). Subsequent return to a moderate voltage (146 mV) for 100 ms allowed to monitor current relaxation reflecting the time course of pore closure (reproduced at an enlarged scale) The data could be fitted with an exponential equation (continuous line superimposed on current trace, see text). Finally, zero voltage was re-established.

dynamics simulations predicted a much faster pore closure. The reason for this discrepancy remains unknown. When pulses of various amplitudes and polarity are successively applied, a current-voltage relation of the membrane can be assessed by plotting the current level at the end of each pulse against the corresponding trans-membrane voltage difference. An example obtained on a protoplast (a plant cell, in this case a 'bright yellow 2' (BY-2) tobacco culture cell, after removal of the cell wall matrix) is shown in Fig. 2.1.6. The current-voltage curve allows to infer the membrane conductance as a function of voltage. However, in principle there are two ways of doing so (known from the literature on the analysis of voltage-gated ion channels): The so-called *slope conductance* represents the first derivative of the current-voltage curve,  $dI/dU_M$ . This parameter contains little information on the underlying process of pore formation and the physical mechanisms involved. A more useful parameter is the so-called *chord conductance* ( $G_{chord}$ ). For every point on the current-voltage curve, the current level is divided by the respective membrane voltage. Zero voltage is set to the potential at which no current passes through the pores (reversal potential,  $E_{rev}$ ; note that  $E_{rev}$  deviates from zero voltage when the pores possess a change towards cations or anions):

$$G_{chord}(U) = \frac{I(U)}{U_M - E_{rev}}$$

The chord conductance is open to interpretations in terms of a variable, electrical field-dependent number of nanopores. An example for the plot of  $G_{chord}$  (reflecting membrane pore formation) against membrane voltage is depicted in Figure 1.2. Following Neumann et al. 1999, the conductance increase with de- and hyperpolarization can be fitted with a Boltzmann function of the following form:

$$G_{chord}(U) = \frac{G_{chord,max}}{1 + \exp((U_{0.5} - U_M)S)}$$

$$\text{With the slope factor } S = \frac{M}{RTd} \quad (\text{in mV}^{-1}).$$

( $G_{chord,max}$  is the maximum chord conductance,  $U_{0.5}$  is the voltage at which the conductance attains 50% of the maximum value,  $M$  is the increase in membrane dipole moment,  $R$  is the gas constant,  $T$  the absolute temperature and  $d$  the membrane thickness). The equation describes the field-induced transition between two states: a physiological, non-porated state of the membrane, and a porated state corresponding to an optimum pore size and density. A key parameter describing the transition between these states is the increase in membrane dipole moment by a progressive intrusion of water into the membrane. The dipoles of the water molecules are aligned, following the direction of the field. When switching from hyper- to depolarization (and vice versa), the water molecules are re-oriented, and the sign of  $M$  (and, in turn, of the slope factor  $S$ ) changes. In the future, this interpretation of the data, that is still largely phenomenological, will be modified to arrive at a more refined model based on molecular physics of pore formation (in cooperation with Drs Clair Poinard, INRIA, and David Dean, University of Bordeaux, France).

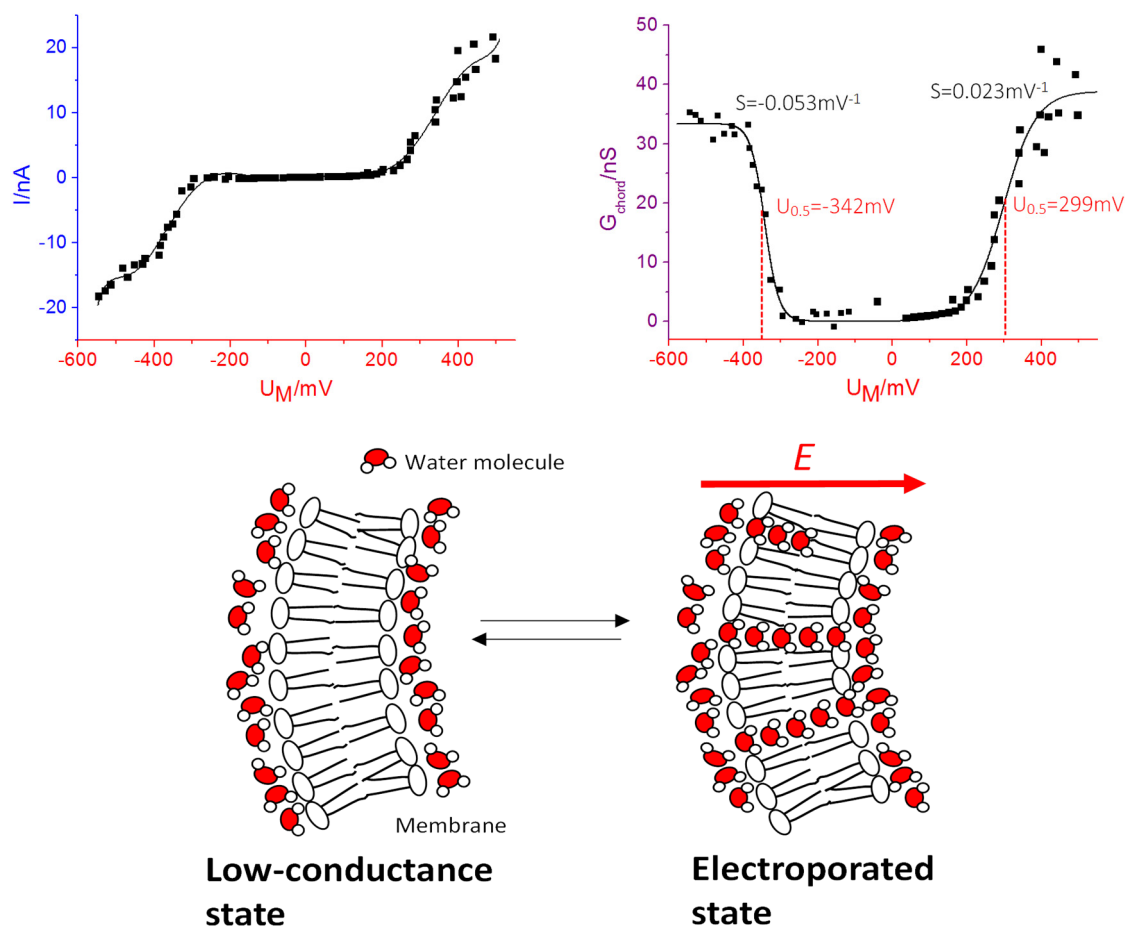


Fig. 2.1.7 Current-voltage curve (top, left) and plot of the chord conductance against membrane voltage (top, right) for a BY-2 protoplast. Voltage dependence of conductance was described with the Boltzmann equation given in the text (negative and positive voltage range fitted separately, best fit parameters given in figure). Bottom, left: Sketch of the model underlying quantitative treatment of conductance data. Membrane polarisation induces a progressive transition from a low-conductance to an electroporated state. For more details,

### 2.1.5 New models to describe the electroporation phenomena

When biological cells are submitted to intense pulsed electric field, a voltage is induced on their external membrane. This voltage, so called transmembrane voltage (TMV) is what triggers the electroporation phenomena: the membrane loses its integrity; it becomes partially permeable and also highly conductive. In collaboration with Clair Pognard from INRIA in Bordeaux (France) and Lluís Mir from the IGR in Villejuif (France) we are developing theoretical models to describe the whole electroporation phenomena. Equations are based on classical electromagnetic equations for the electric aspects and phenomenological equations for the permeabilisation aspects. The main breakthrough of the model that we recently published is that it separates the conductivity and the permeability of the membrane. High conductivity increase is mainly attributed to pores and described with fast dynamics of creation and of recovery. Permeabilisation on the other hand is attributed to chemical changes, a process with much slower recovery time constant. The model is much more complex than the ordinary differential equation since it also includes surface diffusion of the altered part of the membrane, which enable to describe the effect of pulse repetition and

of pulse repetition rate. The model still requires full calibration of all parameters but preliminary studies confirm that such an approach can finally efficiently reproduce the experimentally observed behaviors.

### 2.1.6 Study of the dynamics of the transmembrane voltage

The models presented above require calibration of the different parameters. Our group is therefore providing the required quantitative data on the TMV and especially on its dynamics. Data can be obtained using a fluorescent dye (ANNINE-6) which is sensitive to local electric field. Once the dye is inserted in the membrane of the cells, images of the fluorescent signal can be obtained with a temporal resolution of 5 ns, using a microscope with a pulsed laser illumination setup. The analysis of the fluorescence signals provides us information on the TMV. The figure below displays experimental results obtained on the cathodic hemisphere of a cell. It represents fluorescence signal as a function of electric field intensity. Data were obtained 100  $\mu\text{s}$  after the onset of an electric pulse and can be compared to the results obtained 1  $\mu\text{s}$  after the onset of the electric pulse (Fig. 2.1.8, blue line). The electric field above which the 100  $\mu\text{s}$  data deviate from the 1  $\mu\text{s}$  data is considered as the 100  $\mu\text{s}$  breakdown electric field.

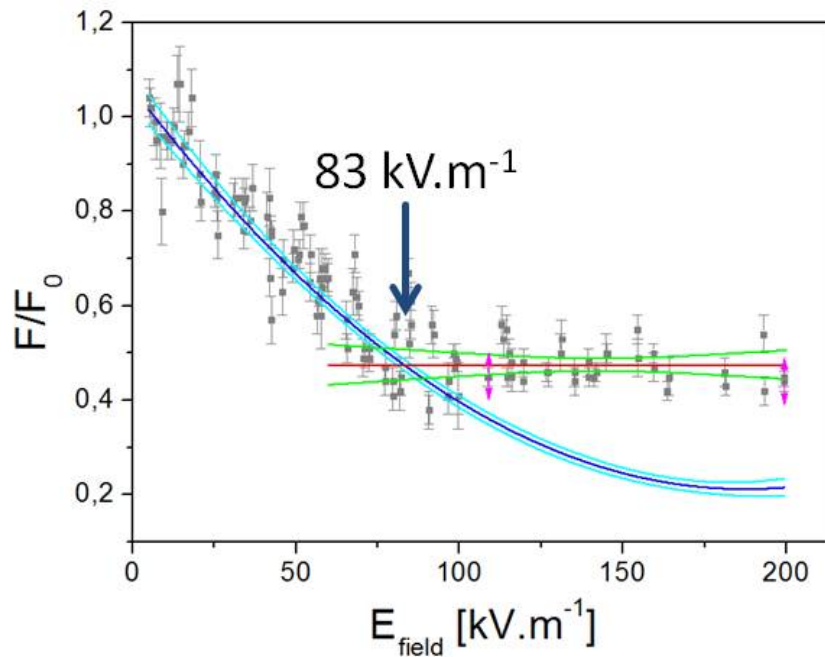


Fig. 2.1.8

Fluorescence signal variations on the cathodic side of a cell as a function of field intensity. Data were obtained 100  $\mu\text{s}$  after the onset of the external electric field. For comparison, data obtained 1  $\mu\text{s}$  after the onset if the electric fields are described by the blue line. The electric field of breakdown is evaluated at 83  $\text{kV.m}^{-1}$ .

Breakdown electric field can be evaluated at different time during electric pulses. The values extracted have been reported on the following graph, Fig. 2.1.9. For each of these data points, the membrane reaches the critical stage when the membrane will start to discharge due to too high conductivity. We can therefore precisely define the electric pulse parameters were the membrane conductivity is high enough to have external charging currents strictly compensating the discharge currents through the membrane. According to our simulations, the surface conductivity at this point is in the order of 1000  $\text{S/m}^2$ . Above the electric field of breakdown, we observe continuous discharge of TMV over time.

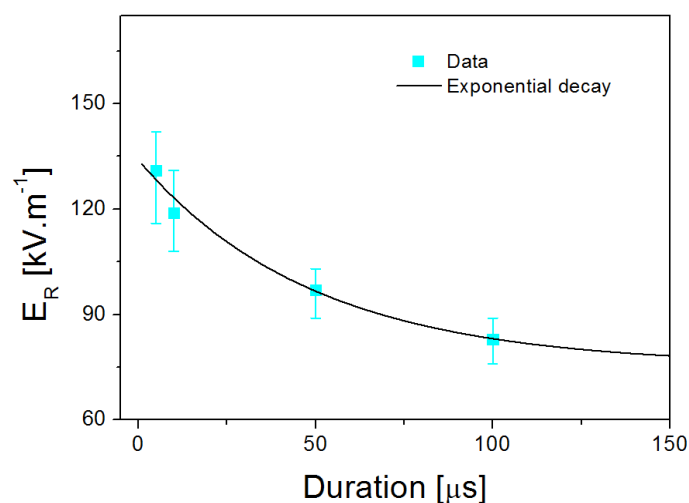


Fig. 2.1.9

Membrane breakdown field strength at different times during rectangular pulses. With increasing pulse duration the required external field for membrane permeabilization exponentially decreases.

### 2.1.7 Organization of the 2014 Bioelectrochemistry Gordon Research Seminar

In June 2014, Aude Silve has chaired the Gordon Research Seminar which was held in conjunction with the 2014 Gordon Research Conference on Bioelectrochemistry. This two days event, took place in University of New England, Biddeford in the US. Effects of both endogenous and exogenous electric fields were discussed. Part of the seminar was focused on understanding the basic effects of these electric fields at the biophysical, biochemical, biomolecular and biocellular levels. Additional emphasis was given to the related applications that emerge or that are being consolidated, especially in the field of medicine.



Fig. 2.1.10

Participants of the Gordon Research Seminar 2014 on Bioelectrochemistry in Biddeford (US).

The Gordon Research Seminar brought together experts of several disciplines including biology, medicine, electrical engineering, biochemistry and biophysics. It successfully boosted interactions between all students, post docs and young investigators working in the field of bioelectrochemistry.

### 2.1.8 Fast MOSFET-Based High-Voltage Switch for a Cable Pulse Generator

For continuous treatment of algae for growth stimulation a fast stacked MOSFET switch has been set up. It is for use with a Blumlein-type cable pulse generator. Using an 12-stage switch an rise time of 8 ns has been achieved at a voltage of 9.6 kV. The design of the switch has been described in the IHM annual report 2013. This year, the switch has been operated successfully in a long-term experiment, lasting for for several days so far.

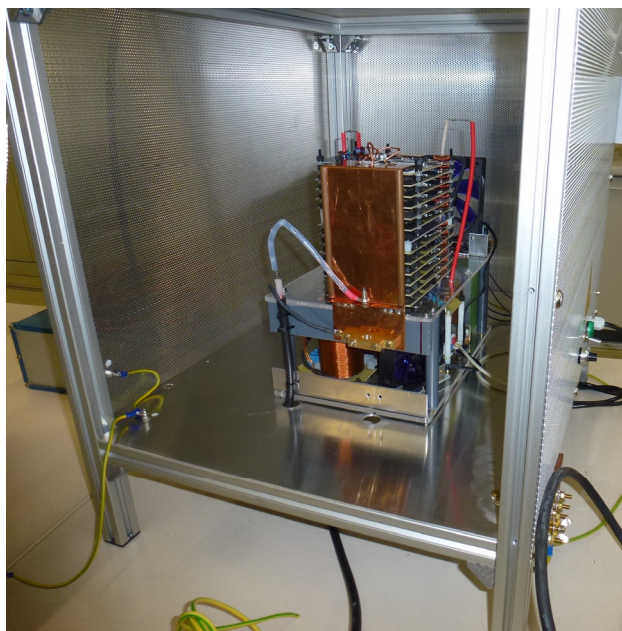
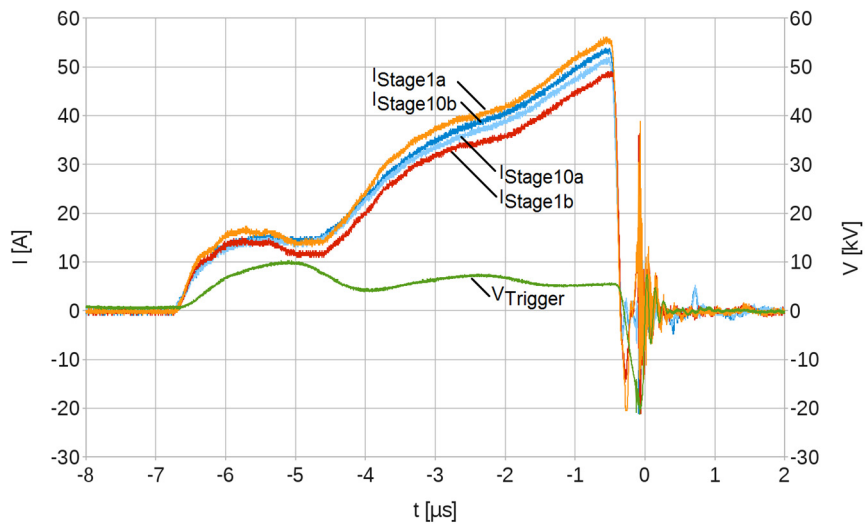


Fig. 2.1.11  
12-stage MOSFET switch in a housing for a long-term experiment.

### 2.1.9 Modular Trigger Generator for Over-voltage Triggering of Marx Generators

The modular 20-stage over-voltage trigger device described in the IHM annual report 2013 has been tested successfully in an 7-stage Marx generator. The trigger device is based on an air-core transformer. Each stage comprises a part of the transformer's secondary winding, two separate primary windings, each connected to one IGBT-switch for pulse generation, a parallel configuration of capacitors providing the pulse energy, and the related driving- and control circuitry. Although the coupling factors between primary and secondary windings differ with the stages, almost equal primary currents have been achieved by appropriate adjustment of individual capacitor charging voltages for the stages. Fig. 2.1.12 shows the measured primary currents of the first and 10<sup>th</sup> stage.



**Fig. 2.1.12**  
 Currents in the low-voltage side windings of stage 1 and stage 10 and voltage across trigger device during pulse generation with the Marx generator's 2<sup>nd</sup> stage shorted.

For triggering a spark gap the trigger device is capable of delivering approximately 10 A in combination with the high-voltage side charging coil for charging the stray capacitances of the Marx generator and the spark gap. According to measurements the voltage across the trigger device and, hence, the spark gap rises from 0 V to its negative peak of -16 kV within 172 ns resulting in a steepness of the trigger voltage of 9.3 kV/100ns. The effective stray capacitance can be estimated to approximately 107 pF. Fig. 2.1.13 shows the voltage across the trigger device and the current through the load resistor of the main pulse circuit.

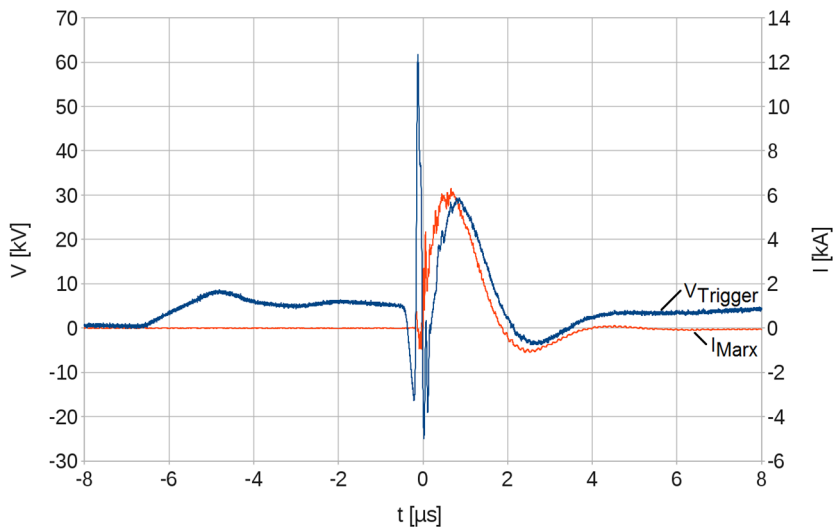


**Fig. 2.1.13**  
 Voltage across the trigger device and current through the load resistor of the main pulse circuit.

### 2.1.10 Design of a semiconductor-based Marx generator

For parameter studies on the electroporation of plant cells a pulse source enabling a waveform generation within a wide parameter range is required. Hence, a semiconductor-based Marx generator for the generation of bipolar pulses is currently being developed. The design consists of a series connection of IGBT bridges, which can be controlled individually in order to generate a stepwise arbitrary waveform. Fig. 2.1.14 shows the principle schematic of a Marx-type modulator with  $n$  stages and  $n$  capacitors.

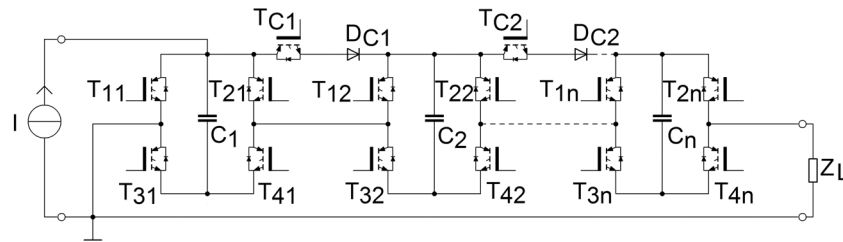


Fig. 2.1.14 Principle schematic of a Marx-type modulator with  $n$  stages and  $n$  capacitors.

In order to protect the IGBTs against induced over-voltage caused by the inductance of the stage capacitor and its connecting leads, a snubber circuit as shown on Fig. 2.1.15 has been implemented across each switch.

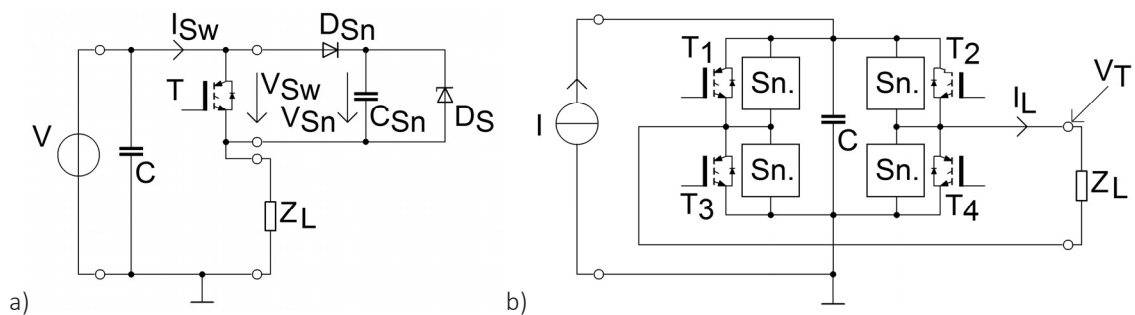
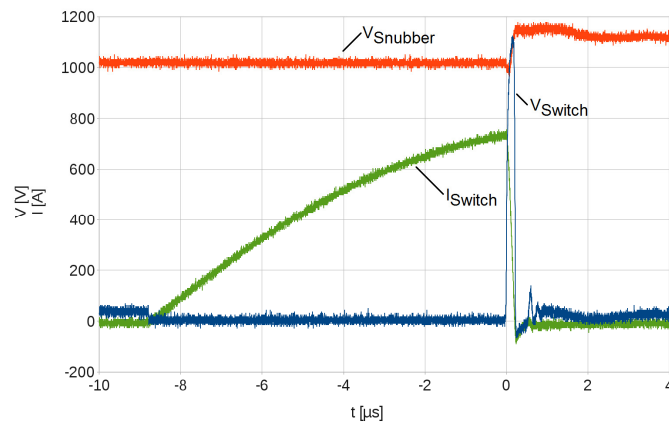


Fig. 2.1.15 Snubber circuit: a) snubber circuit consisting of a diode, a capacitor and an avalanche diode and b) implementation of the snubber circuit across each switch.

When switching off one switch, inductive energy is transferred across the diode  $D_{Sn}$  to the capacitor  $C_{Sn}$  of the snubber circuit causing an increase of the voltage across this capacitor. In order to allow for fast voltage rise across the switch the voltage across  $C_{Sn}$  is kept above the maximum operating voltage of the switch which is lower than the maximum allowable voltage across the switching element. Hence, the capacitor is discharged across an avalanche diode  $D_S$  defining the lower limit for discharge. The voltage span between this lower limit for discharge and the maximum allowable voltage across the switching element defines the amount of energy to be stored in the snubber capacitor for limiting the voltage across the switch.



**Fig. 2.1.16**  
 Measured voltage across the capacitor of the snubber network, together with the voltage and current through the switch when switching 750 A peak current.

Fig. 2.1.16 shows measurements of the current through the switch  $I_{\text{Switch}}$ , the voltage across the switch  $V_{\text{Switch}}$  and the voltage across the snubber capacitor  $V_{\text{Snubber}}$  when switching off a current of 750 A. One stage of the Marx generator has been set up and tested successfully. Fig. 2.1.17 shows the measured voltage at the output terminal of one stage and current through the load when switching a combined resistive and inductive load.

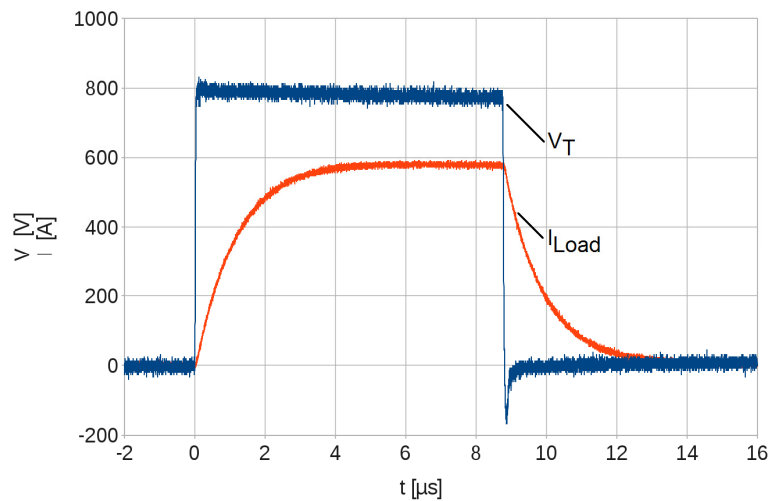


**Fig. 2.1.17**  
 Voltage at the output terminal of one stage and current through the load when switching a combined resistive and inductive load.

**Involved Staff:**

H. Brüsemeister, Dr. C. Eing, J. Fleig, **Dr. W. Frey**, Dr. C. Gusbeth, Frau DI M. Göttel, D. Herzog, M. Hochberg, S. Keipert, K. Leber, E. Menesklou, Prof. G. Müller, K. Paulus, D. Quattrocchi, Frau S. Rocke, **Dr. M. Sack**, Frau Dr. A. Silve, DI R. Sträßner, R. Wüstner

# 3 HGF Program: Nuclear: Safety Research for Nuclear Reactors

## 3.1 32-30-02 Cross Cutting activities

### 3.1.1 Corrosion and Wear Protection for New Reactor Technologies

During the past, the development of new types of nuclear reactors investigated in the frame of GEN IV was the major objective of this target agreement. The development of technologies required for the safety of fast heavy metal cooled reactors like the Lead Fast Reactor (LFR) was the core area of the work performed at KIT. Especially the development of advanced materials e.g. ODS steel and the investigation and improvements of their compatibility with the proposed coolants were in the focus of this work.

Based on this expertise and in consideration of the future involvement in non-nuclear fields like CSP (concentrating solar power) and others the main activities in this reporting period were: the use of liquid metals for direct methane reformation, with associated issues like catalysts for the gas phase; continuation and finalizing the project with BMW to improve the embrittlement of steel in hydrogen atmosphere; GESA beam target interaction. All activities are embedded in "nuclear" and co-financed by the BMW bilateral project and the joint IASS-KIT project for methane reforming.

The most important results obtained in the reporting period are briefly presented:

### 3.1.2 Oxygen free methane reforming in liquid metals

The final aim of the joint IASS-KIT project on oxygen free methane reforming is to develop an experimental reactor for continuous hydrogen production by thermal decomposition of methane in liquid metals. In the past the principal feasibility of this process has been shown using lead (Pb) or tin (Sn) as heat transfer medium. However, at the desired temperatures (up to 950°C) the liquid metals contribute significantly to the corrosion of the reactor materials due to the high solubility of the steel alloying elements. Beside that, the high carbon content in the facility can lead to metal dusting or material embrittlement. The latter might be accelerated due to the likely diffusion of the produced hydrogen into the bulk material. Therefore material compatibility tests in liquid tin are one of the focus points of our work. In tests at 900°C for 46 h tungsten and graphite showed no attack, while a slight corrosion attack was visible at Mo. Based on these results a concept for a methane reactor using graphite as Sn contact material at the high temperatures and Mo as structural materials in the intermediate temperature range (< 550°C) was created. Therefore, Mo was tested in a long-term test (840h) at three different temperatures: 442°C, 559°C and 621°C. At 442°C and 559°C no corrosion attack was visible, as shown in the left picture of Fig. 3.1.1. At 621°C Mo was dissolved and Mo-Sn precipitations were formed at the surface of the Mo bulk and tin penetrated into the bulk material, see picture on the right side of Fig. 3.1.1.



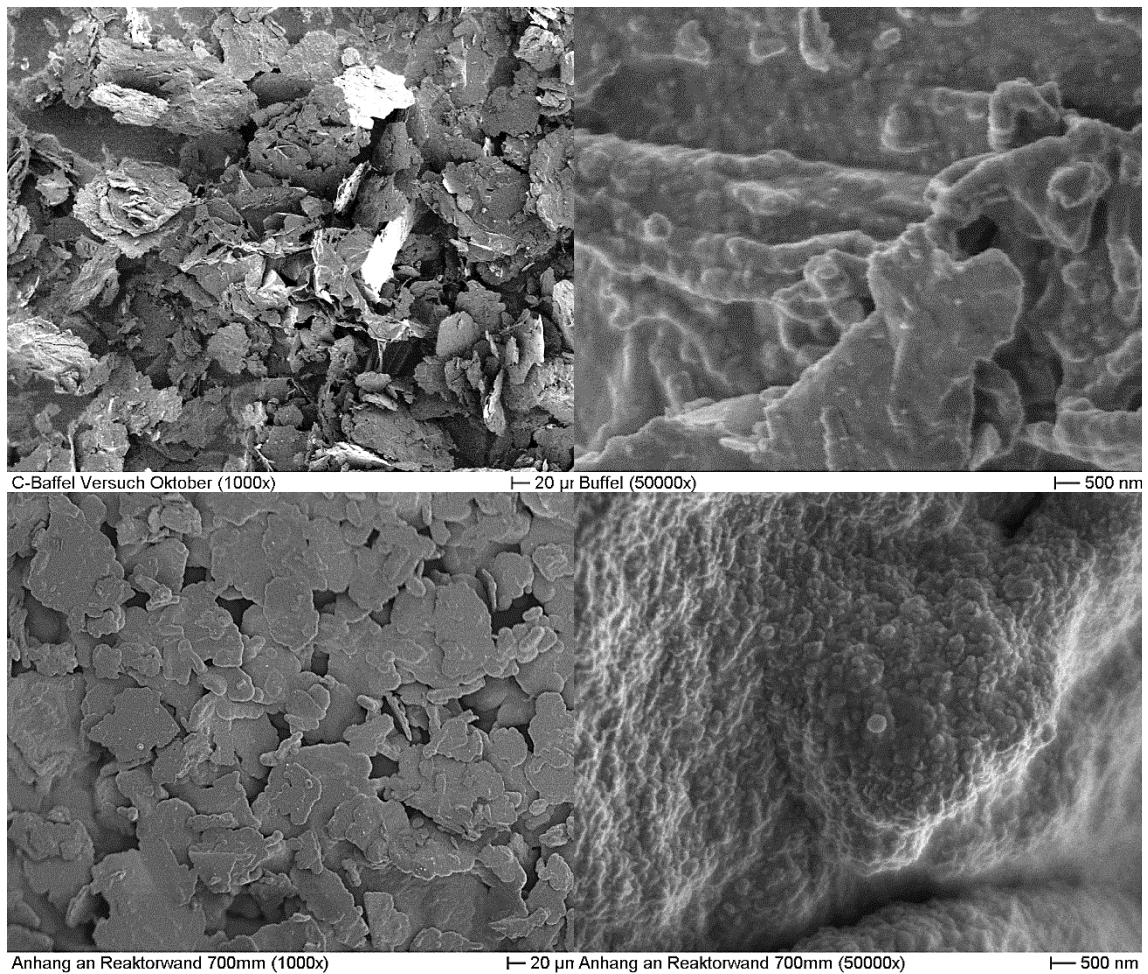


**Fig. 3.1.2**  
**Carbon from the reactor; top: from the gas phase, bottom: from the area with the tin filling**

To clarify if the powder has a catalytic effect for the methane hydrogen reformation, tests with a thermogravimeter (TG) and an attached mass spectrometer were conducted using the carbon from the reactor. The heating rate was 50 K/min up to 850°C, then temperature was hold for 3 h and afterwards it was cooled down again with 50 K/min. During the experiment a gas stream of 40 sccm Methan2.5 and 65 sccm Ar 99.9999 was purged through the TG. A possible carbon formation can be determined by an increasing weight of the samples and additionally the H<sub>2</sub> formation can be measured with the mass spectrometer.

Beside the carbon, which was formed in the gas atmosphere in the reactor and inside of liquid metal part, tin and the black pearl 2000 (BP2000) from the company CABOT were examined. BP2000 has a very high specific surface of 1500 m<sup>2</sup>/g and its catalytic properties are described in literature.

The results of the TG measurements can be seen in Fig. 3.1.3. Only BP2000 showed a significant increasing weight due to the formation of carbon by methane cracking. This is confirmed by the H<sub>2</sub> content measured using the Mass spectrometer (dotted lines). Only the BP2000 show a distinct increase in signal during the dwell time at 850°C. Neither the produced carbon nor the tin showed a significant catalytic ability.

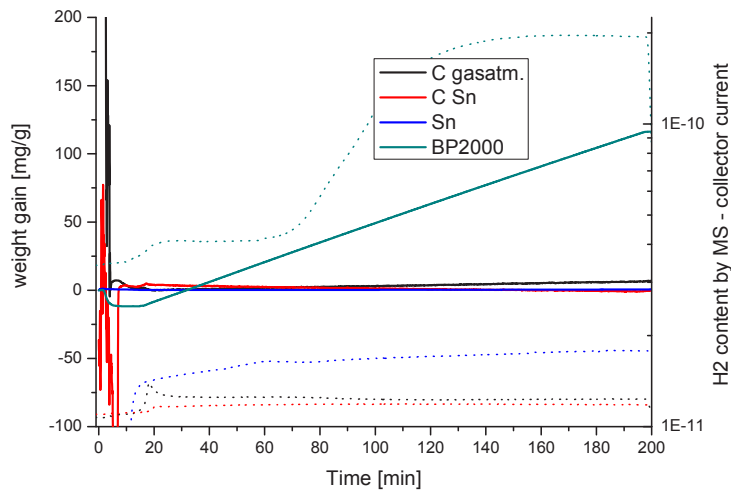


**Fig. 3.1.3**  
TG measurements showing a comparison between the carbon formed in the gas atmosphere of the reactor, carbon formed in the tin, tin itself, and an industrial produced carbon named BP2000 which only revealed a weight gain due to cracking of methane and the formation of carbon.

In the previous report the design of an experiment to measure the maximum allowable pore size was presented which avoid liquid metal penetration. A ceramic or metallic spacer having small pores should allow the generation of tiny methane bubbles that are required for sufficient methane to hydrogen conversion. The set-up was now constructed, ceramic discs with varying pore sizes purchased and measurements were performed by increasing the pressure in liquid metal located above the ceramic membrane and detecting the closing of the connection between liquid metal and the metallic support directly located underneath the membrane.

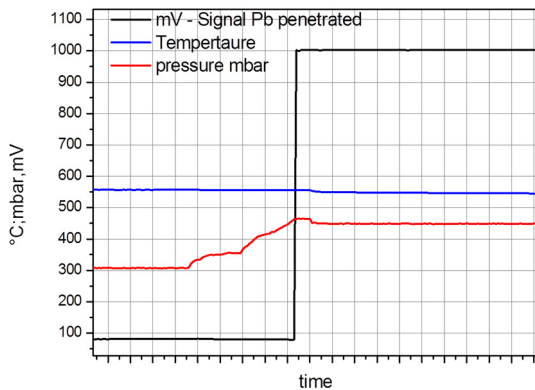


**Fig. 3.1.4**  
Experiment performed with membrane having nominal pore size of 50-60µm at a temperature of 556°C.

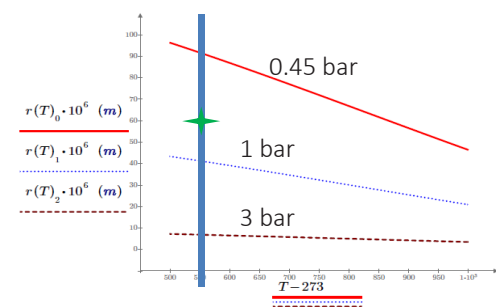


**Fig. 3.1.5**  
Calculated pore size at which PbBi will penetrate as function of temperature and pressure. Experimental data point implemented.

The increase of pressure from 300 mbar to 450 mbar results in the penetration of the PbBi and the voltage rise at the metallic support. A calculation based on the Washburn equation used for mercury intrusion porosimetry yielded a pores size for this pressure (450 mbar) and temperature of about 90  $\mu\text{m}$ . The difference between the nominal pore size of 50 to 60  $\mu\text{m}$  and one obtained in the experiment of 90  $\mu\text{m}$  is most likely related to the “real” pore size of the membrane that was not measured experimentally.

### 3.1.3 GESA optimization - Metal Surface Layers after Pulsed Electron Beam Treatment

The GESA remelting process, when performed with high energy density electron beams, results in a wave-like topography after treatment. In order to minimize the surface undulations, usually additional pulses with lower energy density are applied after the initial treatment. In the reporting period, the effect of repetitive treatment on the topography of stainless steel SS 304 and aluminum (AlMg3) targets was investigated. Two different cases were considered, (i) consecutive high energy density pulses of about 60-80  $\text{J}/\text{cm}^2$  per pulse, denoted by ‘H’, and (ii) one high energy density pulse (H) followed by consecutive low energy density pulses with 29-33  $\text{J}/\text{cm}^2$  each, denoted by ‘L’.

After repetitive treatment with high energy density pulses, case (i), the surface of stainless steel is continuously covered with features of different length scales. In contrast to this surface pattern, after low energy density pulses, case (ii), stainless steel exhibits a ‘crater landscape’ with individual crater-like structures distributed randomly over the sample. The surface between craters is more and more smoothed the higher the pulse number is.

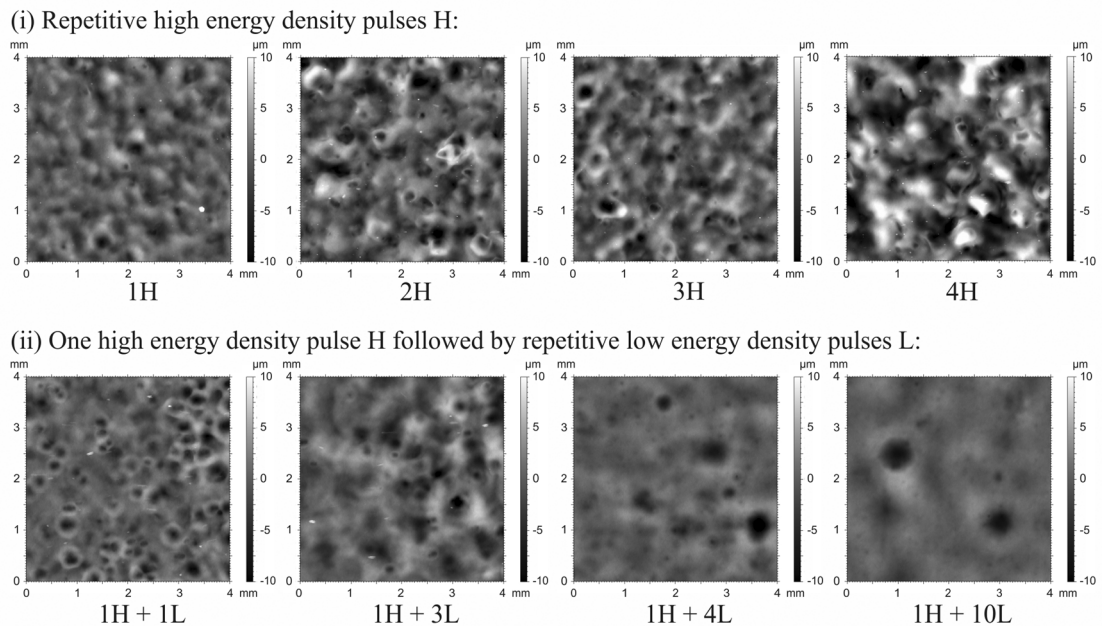
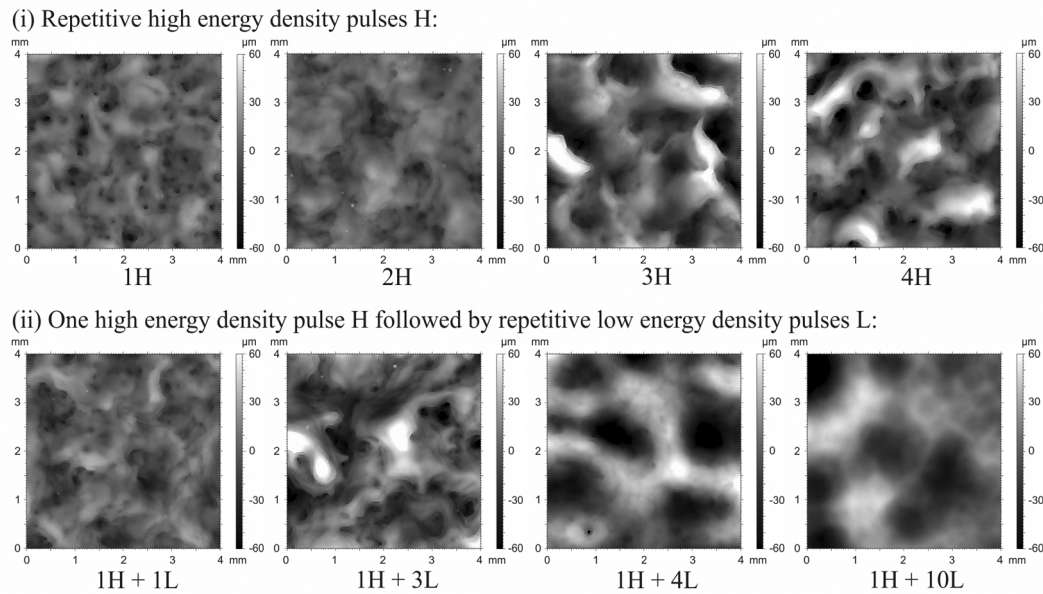


Fig. 3.1.6  
 Profilometer images ( $4 \times 4 \text{ mm}^2$ ) of stainless steel targets after repetitive treatment. The height range of the linear gray-scale is 20  $\mu\text{m}$  for all images.

Due to the high target surface temperatures during treatment, a substantial amount of target material is lost by evaporation, splashing of liquid droplets, and due to eruptions caused by locally overheated regions at material inhomogeneities and inclusions. These eruptions lead to crater formation on the one hand and purification of the target surface layer on the other hand, followed by surface smoothing in subsequent treatment.



**Fig. 3.1.7**  
**Profilometer images ( $4 \times 4 \text{ mm}^2$ ) of Al targets after repetitive treatment. The height range of the linear grayscale is  $120 \text{ }\mu\text{m}$  for all images.**

Repetitive high energy density pulses, case (i), applied to aluminum targets result in a ‘cauliflower’-like structure. With increasing pulse number, the features grow laterally and in height. When treated with low energy density pulses, cases (ii), the aluminum surface topography experiences a substantial change in character after 4 pulses: short scale features vanish completely and long scale waviness develops (wavelength in the mm range).

In case of Al, where melted layers are  $60\text{--}80 \text{ }\mu\text{m}$  thick, ejection of impurities from such large depths is unlikely. Instead, dissolution of the impurities into the surrounding melt, facilitated by the rather long lifetime of the melt ( $\sim 300 \text{ }\mu\text{s}$ ), leads to some degree of material homogenization. Although the target surface layer is apparently homogenized and surface oxides and contaminants are removed by the treatment, repetitive pulses with low energy density do not result in smooth surfaces. The reason might be that, although inclusions are dissolved, the concentration in the matrix is not uniform after the treatments. This can be seen in cross sections (see figure below), where different shades in the micrograph of the melted layer indicate a non-uniform composition and a turbulent flow pattern. Local variations in material composition induce temperature variations and surface tension gradients during subsequent irradiation. Unlike intense evaporation, which was discussed previously as possible cause of the wave-like topography after treatment and which ceases shortly after beam termination, the inhomogeneous composition and related melt motion persist till solidification. It also explains the observation that repetitive treatment with low energy density pulses does not generate smooth surfaces.

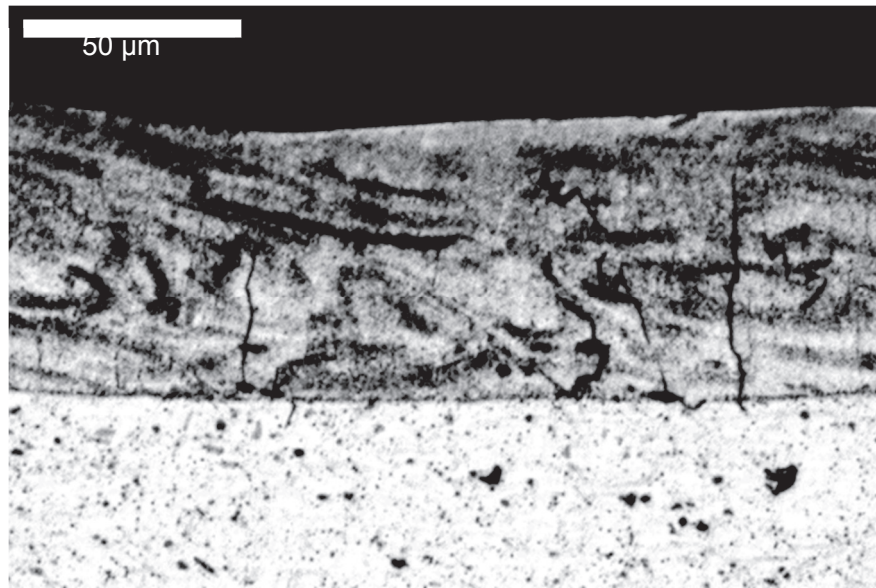


Fig. 3.1.8  
Optical micrograph of Al cross section after treatment with high energy density pulse.

## 3.2 32-24-03 Transmutation – Liquid Metal Technology

### 3.2.1 Materials and oxygen transport and control in heavy liquid metal cooled subcritical systems (MYRRHA)

Long-living high-level radioactive waste from existing nuclear power reactors should be transmuted in short-living radio nuclides using fast neutrons provided by a spallation target in an accelerator driven subcritical system or by a fast nuclear reactor. The objective is to reduce the final disposal time of high-level radioactive waste (plutonium, minor actinides) from some  $10^6$  years down to about 1000 years. Lead (Pb) and lead-bismuth (PbBi) are foreseen as spallation-target and coolant of such devices.

The aim of the institute's contribution is the development of a suitable corrosion protection especially for parts under high loads like fuel claddings or pump materials in contact with liquid Pb or PbBi. Pulsed large area electron beams (GESA) are used to modify the surface of steels such that they fulfill the requirements of their surrounding environment. Corrosion test stands for exposure of specimens under relevant conditions are developed and operated. Test facilities for combined loads like erosion and corrosion and fretting corrosion were developed, built and operated. Conditioning the Pb with regard to its oxygen concentration and the transport of oxygen in PbBi are additional aspects of the work.

All tasks are embedded in European and international projects and cooperations like e.g. MATTER, SEARCH, ESNIIplus and MaTISSE.

The most relevant results obtained in the reporting period are briefly presented:

### 3.2.2 Erosion-tests of promising materials for liquid metal pumps (MATISSE)

In MATISSE so called MAXPHASE materials (ternary carbides) are explored for their use in Pb alloy cooled nuclear systems. One objective beside the production of new types of such materials including CERMETS is the testing of their stability against erosion/corrosion in the CORELLA facility. Two tests including MAXPHASE materials were performed. Test conditions of both tests were: liquid metal - PbBi at temperature of 300°C, duration of 500 h, PbBi velocity of  $v \sim 8$  m/s (700 rpm) – highly turbulent flow and a target oxygen content of  $O \sim 10^{-7}$  wt%. The samples tested were: 316L with and without surface polishing,  $Ti_2AlC$  (MAXTHAL 211®) and  $Ti_3SiC_2$  (MAXTHAL 312®) and graphite. The second test was a continuation of the first test for another 500h at the exact same conditions.

A typical course of the most relevant experimental data is shown in the Fig. 3.2.1. The temperature was, like the other values, nearly constant. The oxygen content was slightly higher than targeted.

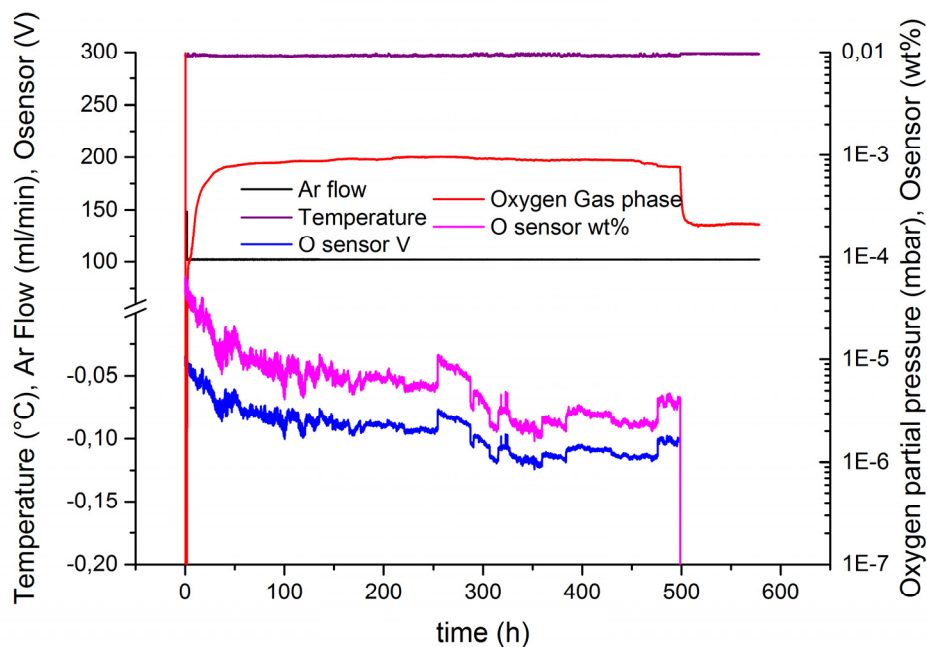


Fig. 3.2.1  
Course of measured experimental parameters during typical CORELLA test

A visual inspection accompanied by white light profilometry showed the absence of erosion interaction at most specimens. Only the MAXPHASE  $Ti_2AlC$  showed erosion corrosion attack, which is clearly depicted in the surface profile of the samples before and after the first test. Whether this material loss is attributed to erosion or just to usual corrosion is still not absolutely clear. In comparison the basically unchanged surface profile of the  $Ti_3SiC_2$  - MAXPHASE material is shown.

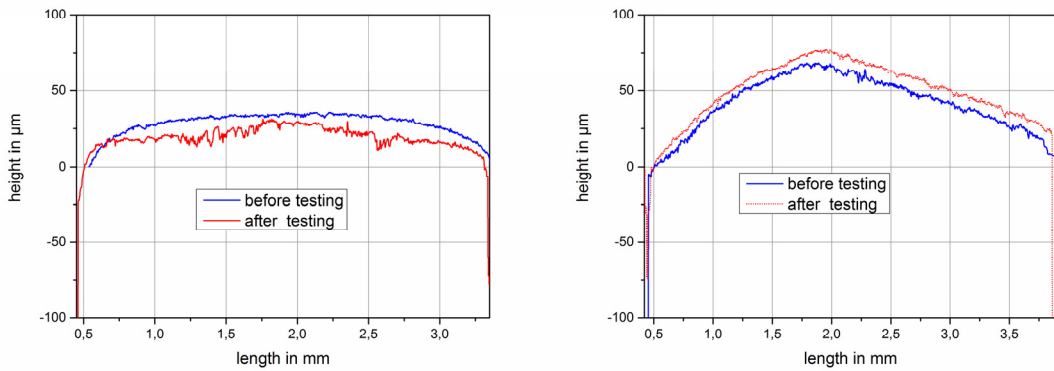


Fig. 3.2.2  
Surface profiles of  $\text{Ti}_2\text{AlC}$  (left) and  $\text{Ti}_3\text{SiC}_2$  (right) before (blue) and after (red) the first 500h test

### 3.2.3 Manufacturing of MAXPHASE materials (MATISSE)

The MAX phases are a series of layered carbides or nitrides with the general formula  $\text{M}_{n+1}\text{AX}_n$  (where M is an early transition metal, A is an A group element, X is C or N and  $n = 1-3$ ). Showing high electrical and thermal conductivities, machinability, damage tolerance and thermal shock resistance these compounds are very promising for applications in advanced energy systems working at high temperatures.

The research activities were focused on synthesis and structural/microstructural characterization of the V-based MAX phases. As a first step, in 2014,  $\text{V}_2\text{AlC}$  compound was synthesis and structural/micro-structural characterized.

The phase formation and their evolution in the mixed powders were analyzed using differential thermal analysis combined with XRD-structural analysis (Fig. 3.2.1). Based on this evaluation the heating rate and sintering temperature for synthesis and densification of the  $\text{V}_2\text{AlC}$  compound were established.

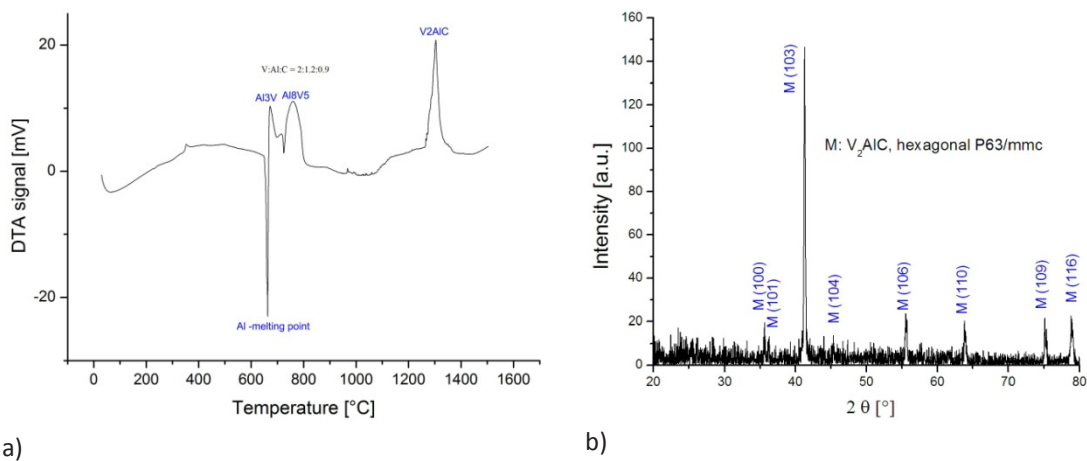
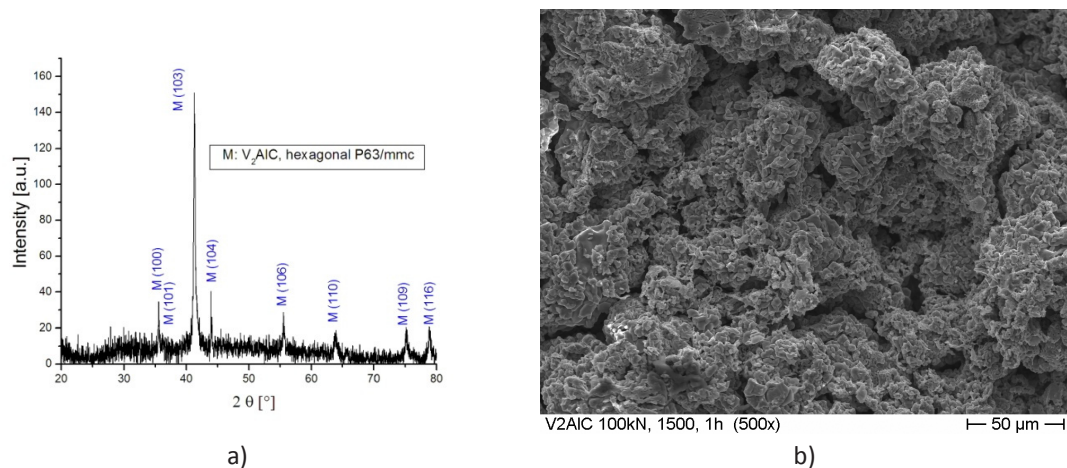


Fig. 3.2.3  
Fig.3: DTA curve obtained on mixed powder with molar ratio of V:Al:C = 2:1.2:0.9 (a) and the corresponding XRD pattern showing the formation of  $\text{V}_2\text{AlC}$  single-phase sample (b)

The synthesis of pure  $V_2AlC$  compound with hexagonal structure (MAX phase, as concluded from the X-ray diffraction patterns) was carried out, starting from mixed powders with a molar ratio  $V:Al:C = 2:1.2:0.9$ , using pressureless furnace heating (heating rate  $5^\circ\text{C}/\text{min}$ , synthesis temperature  $1500^\circ\text{C}$ , holding time 1 h,  $10^{-5}$  mbar vacuum) (Fig. 3.2.2).



**Fig. 3.2.4**  
XRD pattern (a) and morphology (b) of sample synthesis at  $1500^\circ\text{C}$ , one hour holding time, containing  $V_2AlC$  Max-phase

Samples with around 90%  $V_2AlC$  hexagonal phase were also produced using microwave-assisted heating with the following parameters: sintering temperature  $1500^\circ\text{C}$ , holding time 20 min and flowing argon atmosphere.

Almost fully densified sample (Fig. 3.2.3) with around 90%  $V_2AlC$  MAX phase were obtained by one step approach (synthesis/densification in one step) using spark plasma sintering method (heating rate  $20^\circ\text{C}/\text{min}$ , sintering temperature  $1400^\circ\text{C}$ , holding time 30 min, pressure 10 MPa,  $10^{-2}$  mbar vacuum) (Fig. 3.2.3).

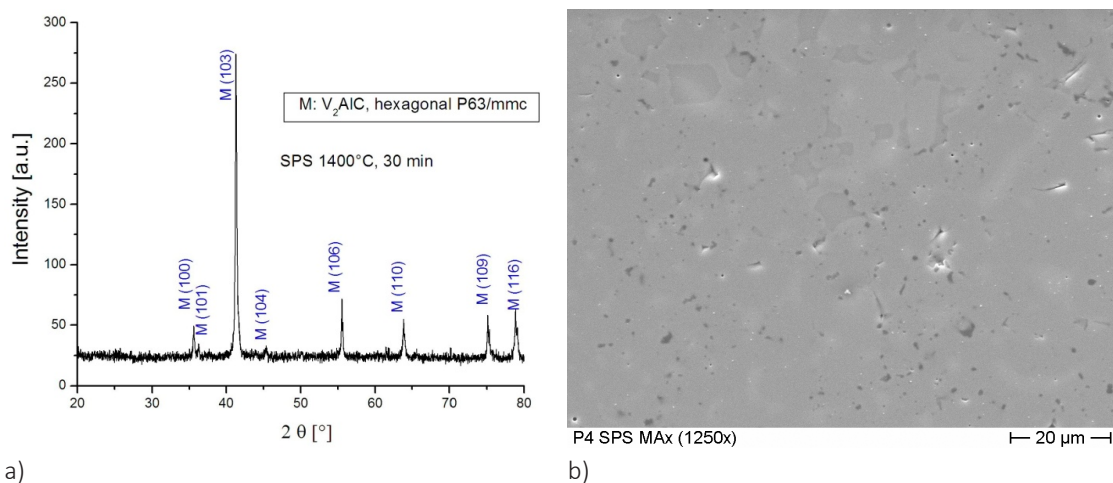


**Fig. 3.2.5**  
XRD pattern (a) and SEM—secondary electron image (b) of the  $V_2AlC$  Max phase sample produced by one step approach (synthesis/densification in one step) using spark plasma sintering method.

### 3.2.4 Oxygen Transport in liquid metals (SEARCH)

In the previous report, the design and setting-up of the MINIPOT device for oxygen transport measurements were presented. The device was used in the last year to explore the oxygen transport in flowing and stagnant PbBi using 5 oxygen sensors located at different dedicated positions in the PbBi.

The conditioning and preparation phase of the experiments were done all in a similar way. The PbBi was conditioned in the conditioning chamber. The  $H_2/H_2O$  ratio was about 0.0166, which corresponds to an oxygen content in the melt at 400°C of about  $2.6 \times 10^{-8}$  wt% and an oxygen partial pressure at 750°C according to a Zirox reading of  $\sim 3.5 \times 10^{-17}$  bar. The gas from the oxygen control system is continuously purged over the liquid metal interface. When the oxygen sensor located in the conditioning vessel shows the expected value the PbBi is pumped at a temperature of 300°C via gas overpressure into the main vessel, which was purged beforehand with Ar+5% $H_2$ .

Experiments are performed the following way: at constant oxygen partial pressure in the gas phase the temperature of the liquid PbBi was changed or at constant temperature the oxygen partial pressure in the gas phase was changed. To understand the time scale of the response of the oxygen sensors after changes in the gas phase one has to consider the volume of the gas phase (about 7l) and the flow rate of the gas (100cm<sup>3</sup>/min). One full exchange of the cover gas volume requires about 70min (4200s).

Typical measured data of the 5 oxygen sensors and of two of the thermocouples are depicted in Fig. 3.2.6. On the left abscissa the voltage reading of the oxygen sensors and on the right abscissa the temperature reading of the thermocouple in °C and the oxygen partial pressure at 750°C (Zirox reading) in mV are given. The temperature signals of both sensors are overlapping indicating that the temperature distribution in the main container is very homogenous. The signals of the 5 oxygen sensors are, except the one of sensor number 2, also pretty close to each other after about 20000 s at a temperature of 390°C.

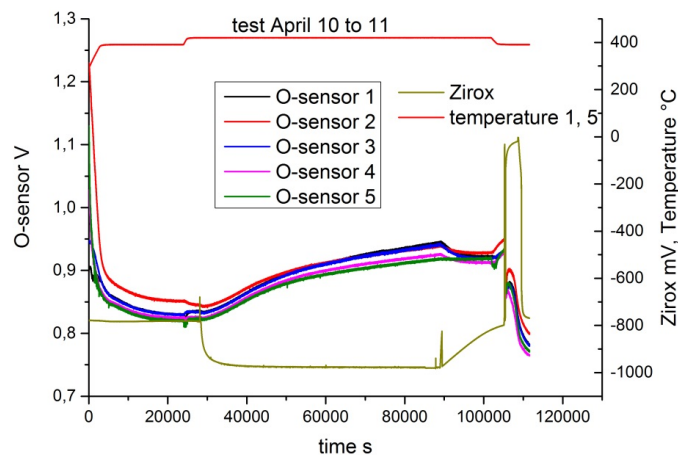


Fig. 3.2.6  
Typical measured data of a test done using the MINIPOT facility

A further increase of temperature to 420°C at time 25000 s results in some behaviour which has not yet been understood completely. Some sensors show an increase, others show no changes or a decreasing voltage. A sudden reduction of the oxygen partial pressure (Zirox reading is dropping to -977mV at time 30000 s) is followed by a slow increase of the oxygen sensor voltage. After ~85000 s the gas phase composition was changed back to the initial value and the sensor response is at least qualitatively as expected.

A more detailed investigation of the oxygen sensor response on the increasing oxygen content in the gas phase is depicted in Fig. 3.2.7.

The oxygen sensors 1 to 4 show an almost immediate response to the increase of the oxygen partial pressure. All 4 sensors react with decreasing voltage. Instead, the sensor no. 5 that is located in the quasi stagnant zone of the PbBi flow does show an increasing voltage. Such behaviour clearly indicates the differences in convective and diffusion transport of oxygen and the necessity to understand and quantify both transport processes.

One very specific course of the oxygen sensor signal is depicted in Fig. 3.2.8. Here at constant temperature an air ingress was simulated.

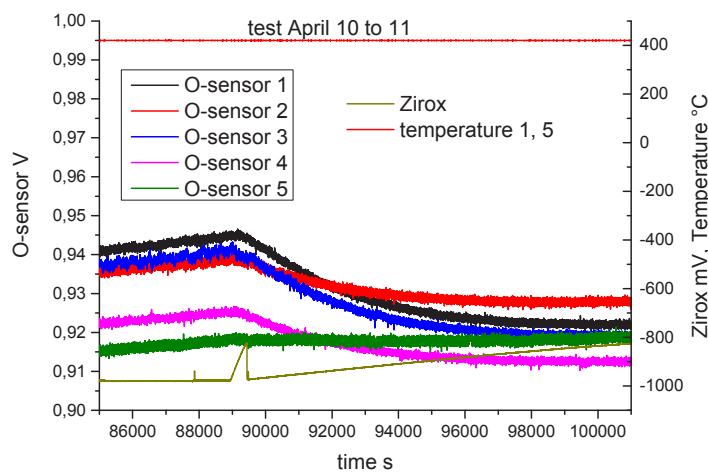


Fig. 3.2.7  
Details of Fig. 6 at time when oxygen content of gas phase was increased again

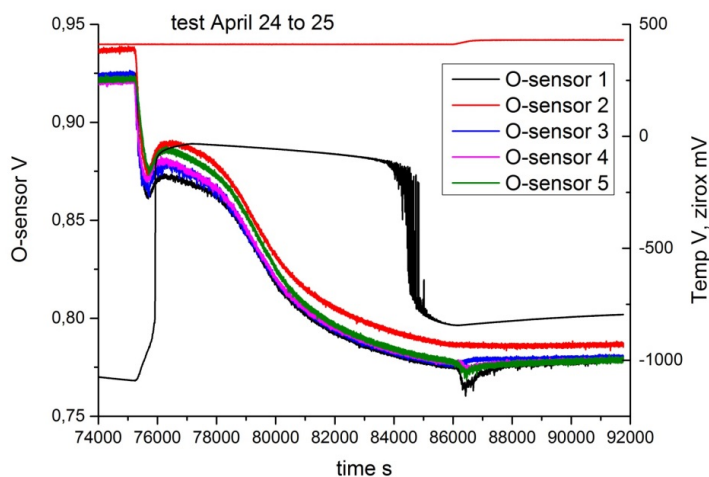
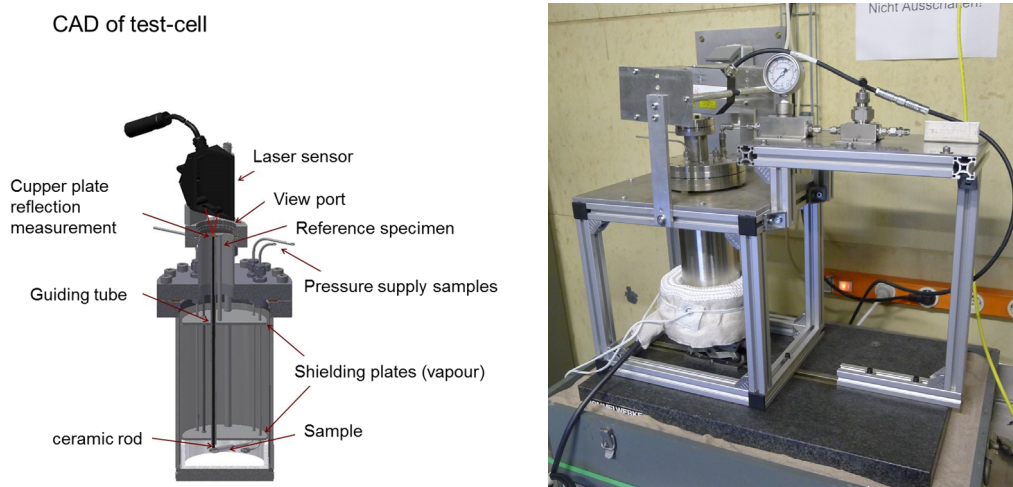


Fig. 3.2.8  
Oxygen sensor response on an air ingress in the cover gas

All the sensors react almost immediately on the increased oxygen content and show a sharp drop in voltage. At 76000 s a sudden increase of the voltage is observed that is reversed after some time and the expected drop of voltage continues. No temperature effect and flow differences can be considered for this behaviour. One possible explanation is the oxidation of dissolved impurities. One can assume that dissolved metallic impurities like Fe, Cr, Ni getter the increasing amount of oxygen and then, after all impurities are oxidized, the dissolving of oxygen in the PbBi continuous. At this oxygen activity most likely Ni is oxidized.

### 3.2.5 Pressurized tube experiment (MATTER)

To evaluate the influence of stress on corrosion and the stability of fuel cladding materials a dedicated experimental set-up was design and constructed. The CAD drawing depicted in the figure below shows the working principal of the set-up. The sample (fuel cladding tube) is attached via 3mm stainless steel tubes to a pressurized cylinder and placed in an  $\text{Al}_2\text{O}_3$  crucible containing PbBi. The alumina crucible is placed in a stainless steel container that can be heated from outside and allows a dedicated control of the oxygen content in the gas phase. The oxygen activity in the liquid PbBi is measured using an oxygen sensor. The strain of the tube is transferred via a ceramic rod to a copper plate placed below the transparent window. The change in position (reflecting the strain of the tube) of this Cu- plate is measured using LASER triangulation set-up with an accuracy in the nm range. The assembled system is depicted in the figure below as well. The device is able to operate at pressures of up to 560 bar and temperatures of  $< 600^\circ\text{C}$ . The pressure will be continuously monitored during the experiment. The manometer is located at room temperature and therefore a detailed analysis of interacting volumes regarding their temperature was performed.



**Fig. 3.2.9**  
Scheme and photography of the pressurized tube experimental set-up

A typical experiment is performed as follows: the pressure cylinder will be pressurized and attached to test cell. After pressurizing the sample the temperature of the system will be increased and the laser measures the position of copper plate continuously to detect the radial strain of tube. The first test experiment was done using samples made of 15Ti15 (1.4970) that was provided from SCK-CEN. The sample was pressurized to 200 bar and the system was heated up to  $450^\circ\text{C}$ . The expected pressure increase from 200 bar at room temperature (pressurizing of the tube) to  $450^\circ\text{C}$  was not observed. Only an increase to about 230 bar was

seen. Re-evaluation of all volumina at room temperature clearly showed that the final pressure at experimental conditions will be dominated by the volumina that stay at room temperature during the experiment. There are two ways to achieve the high pressures needed, either just to increase the pressure for pressurizing at room temperature or to minimize further the volume located at room temperature and to heat up the entire system to at least 100°C. Both options are currently under evaluation.

### 3.2.6 GESA Beam Dynamics

For optimization of the GESA treatment of metal targets, not only the processes involved in the interaction between pulsed electron beam and target are relevant, but also the quality and stability of the beam itself. In order to tune beam parameters and control the beam homogeneity and stability in a reliable way, sound understanding of all related plasma physics processes and their effects on the beam is necessary. This includes the interactions between charged particles, electromagnetic fields, and structural materials. In the reporting period, the commercially available code MAGIC 3D by ATK, USA, was installed and first results were achieved. MAGIC is an electromagnetic particle-in-cell (PIC) finite-difference, time-domain software suitable to perform the required task.

First, the GESA facility needed to be composed of various objects: conductor and dielectric parts, magnetic coils, and grids. Grids can be conveniently generated by the FOIL command, where material, thickness and transparency (or pitch and width) are input parameters. However, for objects generated by this command the inner structure is ignored in the electromagnetic field calculation. Further, FOILs are transparent to electrons only, that is, ions cannot penetrate. For GESA operation, one major problem seems to be that ions generated at the target are accelerated towards the cathode, pass through the grid, penetrate into the gap between cathode and grid, and thus disturb and destabilize the emission process. For valuable information on this process, the foil command cannot be used in the simulation and alternatives are required.

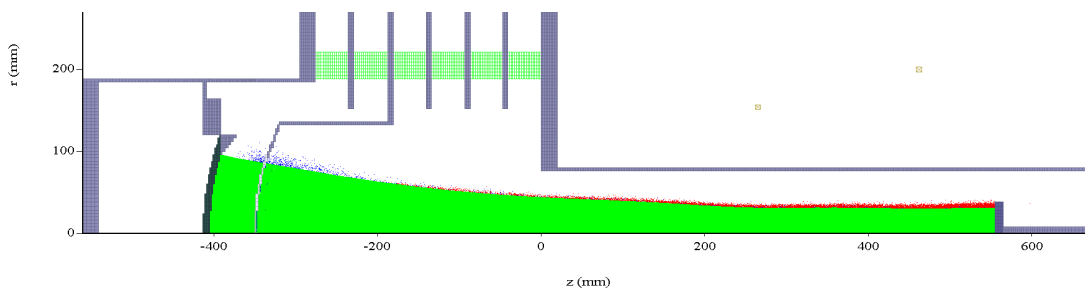


**Fig. 3.2.10**  
GESA I geometry with electron beam. Abscissa shows axial coordinate  $z$  and ordinate shows radial coordinate  $r$ .

Voltage drops between different conducting structures are applied via ports. These are open boundaries of the simulation volume, at which the electric field is specified. Full time-dependent Maxwell equations are solved to compute the evolution of electromagnetic fields on the nodes of the calculation mesh. Various algorithms with specific advantages and disadvantages are available for this task. Simulations of the empty GESA IV facility (cylindrical geometry with radially converging electron beam) without any electrons showed that some numerical damping is necessary to keep the electric field distribution stable on a microsecond time scale, i.e. the time scale of ion dynamics. When introducing an electron beam in the simulation of GESA IV, numerical damping cannot suppress electric field oscillations completely. It needs to be clarified whether this instability is physical or numerical in nature.

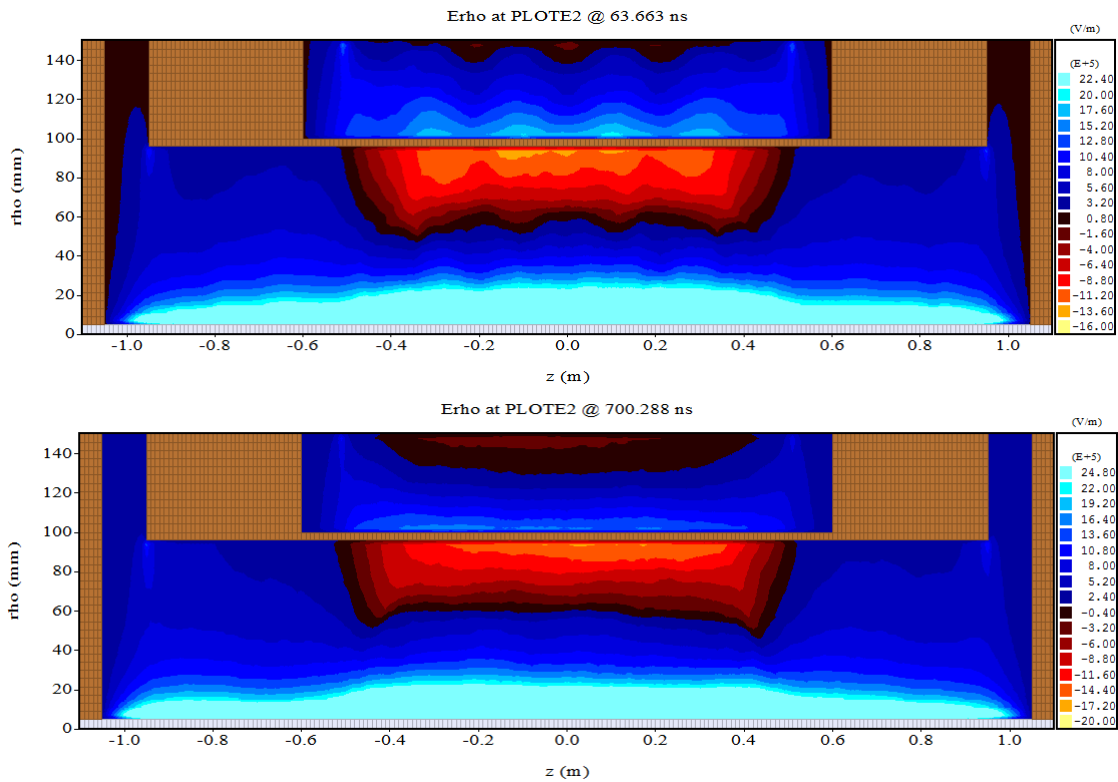


**Fig. 3.2.11**  
 Radial component of electric field in cylindrical GESA IV at two different times, 64 and 700 ns. Oscillations are observed between cathode ( $r = 150$  mm) and grid ( $r = 100$  mm).

The charged particle dynamics is calculated by an explicit (respectively implicit) algorithm solving relativistic (Lorentz) equations of motion. For typical GESA operation with 120 kV accelerating voltage, electrons reach velocities of  $0.6c$  ( $c$  speed of light) and a relativistic factor of  $\gamma = 1.23$ . For the particle advance simulation step, electromagnetic fields are interpolated from the mesh nodes to the positions of the individual macroparticles, each of which represents a large number of physical particles. The size (mass and charge) of macroparticles is determined by the emission process, where either the charge of generated macroparticles or the frequency of macroparticle generation is specified.

MAGIC offers various emission commands to account for field emission, thermionic emission, explosive emission, photoelectric emission, or secondary emission. The algorithm for explosive emission, the type of emission taking place at the GESA cathode, is based on a phenomenological approach. Some quantities such as plasma formation rate, threshold field or residual field, can be specified. Via the plasma temperature, the angular velocity spread at emission can be controlled. Simulations showed that the azimuthal velocity spread in the beam of GESA IV increases over a time scale of 100 ns to about the same level for any plasma temperature below  $\sim 100$  eV. The main drawback of the phenomenological explosive emission routine is that the plasma dynamics (e.g. its expansion) is not considered. In case of GESA with pulse duration of several tens of microseconds, it is therefore necessary to simulate the moving emission area by other means.

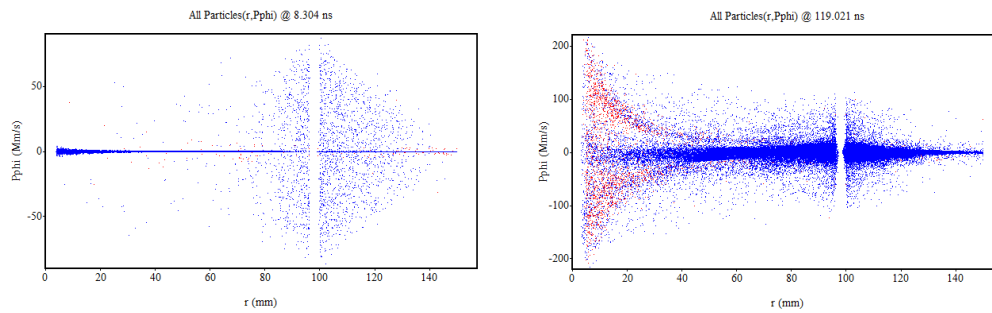


**Fig. 3.2.12**  
Azimuthal momentum versus radial position for two different times, 8 and 120 ns, for emission plasma temperature zero. Blue points represent primary, red points secondary electrons generated at the target.

Finally, the interaction of charged particles and matter is taken into account. Electrons are scattered and backscattered at grid and target; deposited charge is conducted along the materials, whereat the electric current induces a magnetic field; ions are generated at the target, which take part in the complex dynamics of pulsed electron beams. Among the other tasks mentioned so far, the influence of ions on the GESA performance will be investigated in 2015.

### 3.2.7 Optimization of FeCrAl to be used as corrosion barrier in liquid metals

Different system concept designs with HLM as working fluids for energy-related applications are currently under evaluation and development. FeCrAl coatings that are able to form an alumina layer are of great interest due to their good corrosion resistance in liquid metals

In two parallel studies, the corrosion behaviour of twelve Fe-Cr-Al-based model bulk alloys, and eight GESA-modified surface layers exposed to oxygen-containing liquid lead at temperatures between 400°C and 600°C, was investigated. The chemical compositions of the samples were:

- alloys: P1 (Fe-6Cr-6Al), P2 (Fe-8Cr-6Al), P3 (Fe-10Cr-5Al), P4 (Fe-14Cr-4Al), P5 (Fe-16Cr-4Al), P6 (V), P7 (Fe-10Cr-7Al), P8 (Fe-12Cr-7Al), P9 (Fe-16Cr-6Al), P10 (Fe-12Cr-5Al), P11 (Fe-12Cr-8Al), P12 (Fe-16Cr-8Al)
- surface modified layers: A1 (Fe-14Cr-11Al-0.3Y), A2 (Fe-14.5Cr-10Al-0.3Y), A3 (Fe-14.5Cr-10Al-0.3Y), A4 (Fe-13.5Cr-9Al-0.4Y), B1 (Fe-9.5Cr-10Al-0.3Y), B2 (Fe-9.5Cr-9Al-0.3Y), B3 (Fe-9.5Cr-10Al-0.3Y), B4 (Fe-9.5Cr-8.5Al-0.4Y)

Fig. 3.2.12 shows the evolution of the  $\text{Fe}(\text{Cr},\text{Al})_2\text{O}_4$  sub-layer thickness over the tested exposure temperatures of some of the samples P1 to P7, P10 and the modified surface layer B2 (450 °C). One can note that the sub-layer thickness increases with temperature. However, for P5 bulk alloy (Fe-16Cr-4Al), the oxide scale thickness increase with temperature is much lower (from 0.5  $\mu\text{m}$  at 400°C to 1.6  $\mu\text{m}$  at 600°C) than in case of the other specimens. Previous studies showed that a concentration of 4 wt.% Al is sufficient, in synergy with Cr content, to reduce the growth rate of  $\text{Fe}(\text{Cr},\text{Al})_2\text{O}_4$  oxide scale, with spinel structure, on Al-containing ODS alloys after exposure to flowing LBE.

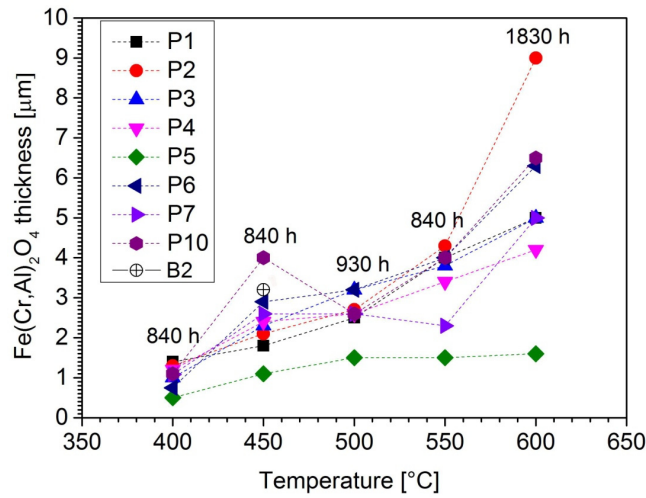


Fig. 3.2.13

The thickness of Fe(Cr,Al)<sub>2</sub>O<sub>4</sub> sub-layer formed at different temperatures on P1-P7, P10 bulk samples, during exposure in oxygen-containing molten lead (10<sup>-6</sup> wt. %). The graph shows also the thickness of Fe(Cr,Al)<sub>2</sub>O<sub>4</sub> sub-layer grown on B2 modified surface layer after 900h exposure time.

The experiments performed in this study have shown that the protective scales grown on P8 (partially) and P9 samples, exposed at 450 and 550°C, as well as on P11 and P12 samples, exposed at 400, 450, 500, 550 and 600°C, in oxygen-containing liquid lead were alumina polymorphs  $\kappa$ -Al<sub>2</sub>O<sub>3</sub> and  $\theta$ -Al<sub>2</sub>O<sub>3</sub>. This is in agreement with previous results obtained for P8 and P9 samples exposed at 400, 500 and 600°C. No area with detached scale was observed and no trace of  $\alpha$  - alumina was detected. These transient polymorphs are highly protective under current experimental conditions.

For the temperature range, oxygen concentration and exposure time considered in the current evaluation, the growth rate of alumina scales was rather low and the thickness could not be evaluated using SEM. However, in case of P9 sample, the average thickness of the alumina layers was estimated based on (i) a semi-quantitative procedure, which was applied to new XPS-SDP experimental data (450 and 550 °C) and to previous XPS-SDP experimental data (400 °C and 500°C) and on (ii) TEM evaluation of the samples exposed at 450 and 600°C.

A sharp increase of the alumina scale average thickness was observed on the sample exposed to oxygen-containing molten lead at 600°C (Fig. 3.2.14 (a)). Besides the higher exposure temperature, two additional factors could be responsible for this behaviour: (i) exposure time increase and (ii) formation of  $\theta$  - alumina polymorph, which was observed only at this temperature and was reported as having a very high growth rate.

The growth of the alumina scale on Fe-16Cr-6Al (P9) samples was approximated by a parabolic rate law of diffusion-controlled oxidation:

$$d^2 = k_p \cdot t \quad (1)$$

where  $d$  is the average thickness of the oxide scale,  $k_p$  the parabolic rate constant (which is a measure for the oxidation rate), and  $t$  the oxidation time.

Values of the parabolic rate constants  $k_p$  related to P9 samples were calculated for all exposure temperatures and, for comparative purpose, their temperature dependence was presented in the Arrhenius plot (Fig. 3.2.14). Calculated data at 400 °C, 450 °C, 500 °C and 550°C correspond to  $\kappa$ -Al<sub>2</sub>O<sub>3</sub> polymorph grown at these temperatures and fit a single regression line. The oxide growth at these temperatures is thermally activated with an activation energy, calculated from the slope of the fitting line, of about 82 kJ/mol, lower than the value reported for  $\alpha$ -Al<sub>2</sub>O<sub>3</sub> (200 kJ/mol), which is reasonable. At 600°C the growth rate is much higher than the rate extrapolated from the Arrhenius plot (dot-line). This deviation of the parabolic rate constant, corresponding to the sample exposed to oxygen-containing molten lead at 600°C, can be attributed to the formation of  $\theta$ -Al<sub>2</sub>O<sub>3</sub> with a higher growth rate than  $\kappa$ -Al<sub>2</sub>O<sub>3</sub>.

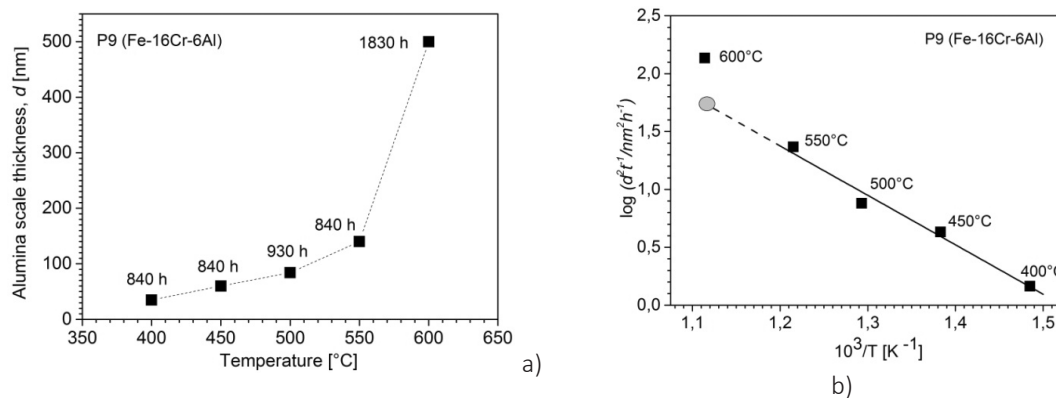


Fig. 3.2.14

(a) Thickness of alumina scale “ $d$ ” grown on P9 bulk alloys (Fe-16Cr-6Al) during exposure in oxygen-containing molten lead (10<sup>-6</sup> wt. %) at 400°C, 450°C, 500°C, 550°C and 600°C; (b) Arrhenius-plot of oxidation rate constant  $k_p$  corresponding to alumina scale on P9 samples versus reciprocal temperature.

#### Involved Staff:

DP W. An, Dr. R. Fetzner, Dr. A. Heinzl, Dr. A. Jianu, DI (Fh) F. Lang, Prof. G. Müller, Dr. G. Schumacher (Gast), A. Sivkovich, **Dr. A. Weisenburger**, DI (Fh) F. Zimmermann

## 4 HGF Program: Rationelle Energieumwandlung und Nutzung (REUN)

### 4.1 Dielectric Characterization, Concepts and Results

#### 4.1.1 In-situ characterization and modelling of polymer composites curing

A test-set for dielectric analysis at 2.45 GHz for monitoring of curing has been developed. The system bases on the transmission and reflection method in a standard rectangular waveguide. It has been used for measurements of the temperature and time dependent dielectric characteristics of polymer composites during curing. Flexible temperature and time schemes which are close to the real curing can be investigated using the developed system. Both dielectric constant and dielectric loss factor can be monitored online during the curing process as shown in Fig. 4.1.1 for an epoxy resin.

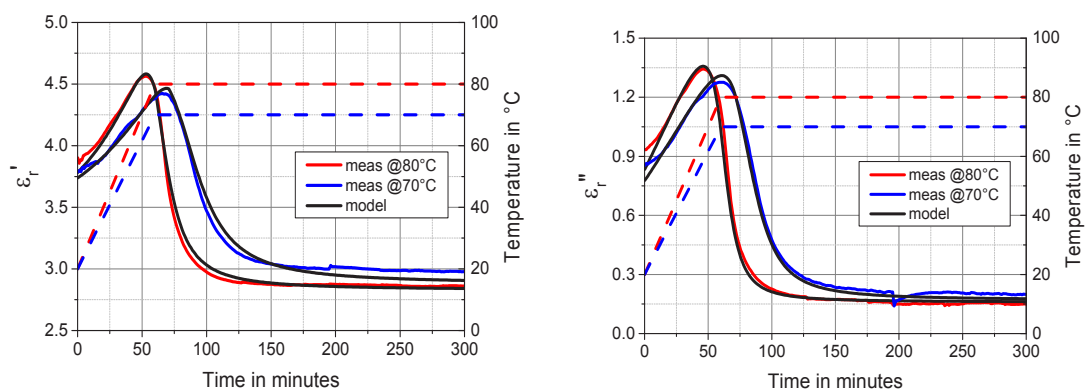


Fig. 4.1.1 Dielectric constant (left) and dielectric loss factor (right) of DGEBA-IPDA measured at 2.45 GHz during curing at 80°C (red) and 70°C (blue).

The temperature was increased from room temperature to curing temperature within 60 minutes and then kept constant. Both dielectric constant and dielectric loss factor raises up with increasing temperature and start decreasing as soon as curing begins after reaching a certain temperature. The fast decrease of the dielectric properties reflects a spontaneous curing reaction. The dielectric properties show an asymptotic behavior at the end of the curing process. The present system has been used for investigation of various mixtures of resin, hardener and filler and the effect on reaction kinetics. A model including the reaction kinetics and appropriate mixing rules has been developed to describe the measured data (see Fig. 4.1.1). Furthermore this model allows estimating the degree of polymerization  $\alpha$ , with variation of temperature and time as shown in Fig. 4.1.2.

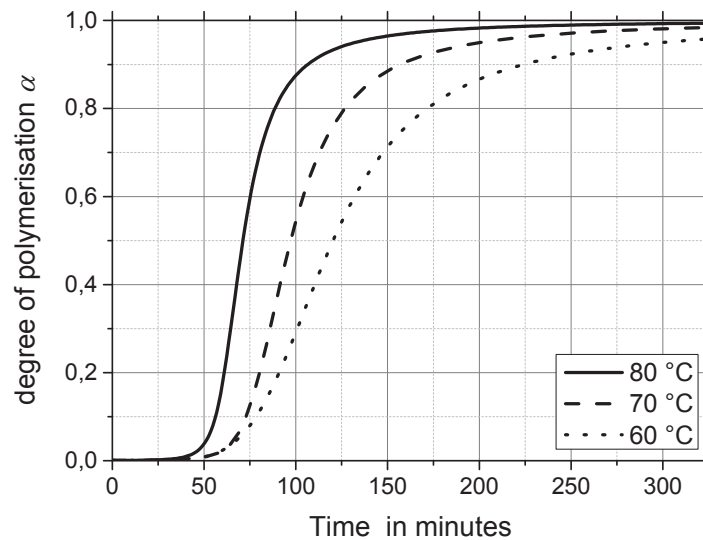


Fig. 4.1.2  
Degree of polymerization of DGEBA-PEA D230 estimated on the basis of measured permittivities at 2.45 GHz

#### 4.1.2 Dielectric characterization using the cavity perturbation method

The set-up based on the  $TE_{104}$  mode WR340 rectangular waveguide resonator allows the characterization at a frequency of 2.45 GHz and for temperatures ranging from 25°C to 1100°C. In perspective of possible development of human implantants by use of microwave sintered hydroxyapatite as bone scaffolds, the dielectric properties both bone and hydroxylapatite samples were measured within 25...1050 °C. The measured permittivity (see Figuer 1.3) as well as the results obtaine by systematic sintering studies (see Chapter 0 look encouraging for possible microwave applications.

Possible application of microwave technology in the process of terephthalate (PET), e.g. drying and recycling, may reduce the energy consumption in the process. The dielectric properties of PET were investigated within 25...250 °C temperature range. Loss factor being quite low at room temperatures increases exponentially with the temperature thus providing higher and higher coupling of microwave.

With the attempt to extend the reliability of the measurement set-up towards high loss materials and to meet the needs of current and coming projects the operational limits and accuracy were explored. Therefore the extended full-wave simulations of the experimental set-up for an extended range of material permittivities were performed and results were cross-checked with corresponding results of the cylindrical cavity set-up described in the Chapter before.

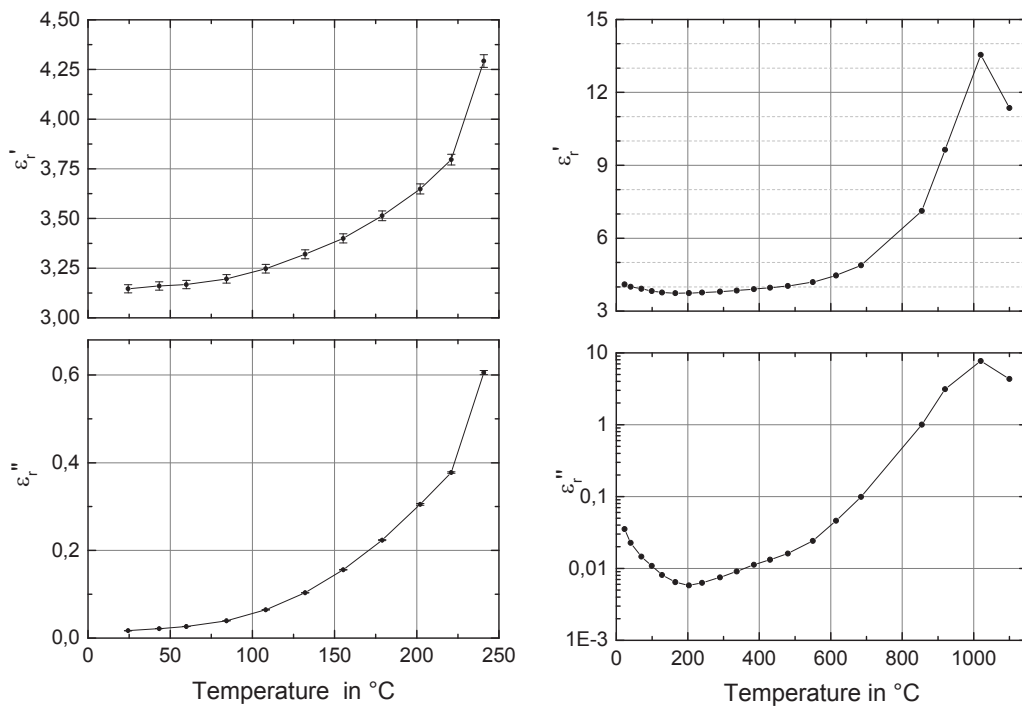


Fig. 4.1.3 Dielectric properties of polyethylene terephthalate (PET) (left) and hydroxylapatite (right).

### 4.1.3 In-situ monitoring of the dielectric and the calorimetric properties

A system for in-situ monitoring of the dielectric and the calorimetric properties during the microwave heating of materials at 2.45 GHz was developed. The dielectric characterization of the materials under test is based on the cavity perturbation technique. This test set enables the dielectric characterization of dielectric materials with low and medium loss factor. The overall design of the developed measurement system is shown in Fig. 4.1.4.

A key element is the tunable power amplifier ISYS245 from Embian Microwave which provides up to 50 dBm output power and an amplification of an input signal by 55 dB. The vector network analyzer (NWA) AgilentN5224A is used for both the measurement of the transmission factor  $S_{21}$  and as an input source for the power amplifier. The output power of the amplifier is coupled into the resonant cavity. An Anritsu ML2488B power meter is used to measure the incident and the reflected power as well. The isolation of the incident and reflected signals is realized by using a WR340 waveguide circulator and a waveguide directional coupler. For accurate power measurements the NWA and the power meter need a proper synchronization. For measurement of sample temperatures a pyrometer type CellaTemp PA10AF1 is used.

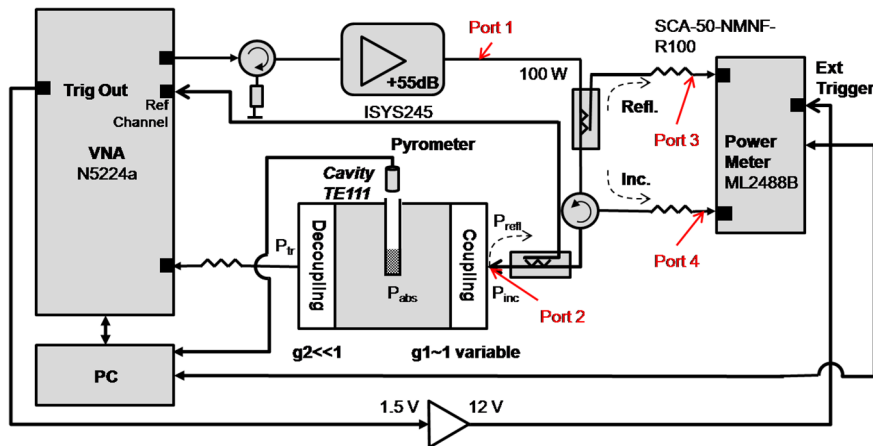


Fig. 4.1.4  
Block diagram of the developed system.

The calibration of the dielectric measurement is done with a full-wave modeling (with CST Microwave Studio) within the range of the expected dielectric properties. And the power calibration is based on the measured S-Parameter matrix of that part of the system between the two power sensors (Port 3 & 4), the power amplifier output (Port 1) and the cavity input (Port 2) (see Fig. 4.1.4).

Finally a MATLAB code has been used for temperature and time depending dielectric and calorimetric characterization of various dielectric materials. Key part of this code is a PID control algorithm, which enables an accurate control of the sample temperature along any preset temperature scenario. The software allows a loop controlled operation including heating and data acquisition. An excellent control time of 0.5 s has been achieved.

This test-set has been used for characterization of various dielectric materials as for example for permittivity measurements during microwave curing of epoxy resins at different heating rates. As soon as polymerization starts dielectric constant as well as dielectric loss factor decrease till the curing process is completed.

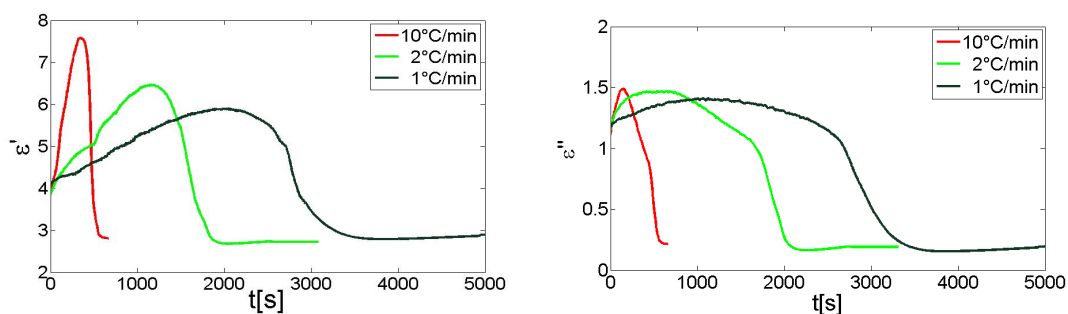


Fig. 4.1.5  
Permittivity of an epoxy resin as a function of time for different heating rates

Analysis of the calorimetric data reveals the exothermic character of the curing process which is more pronounced for fast heating as can be seen in the following graph.

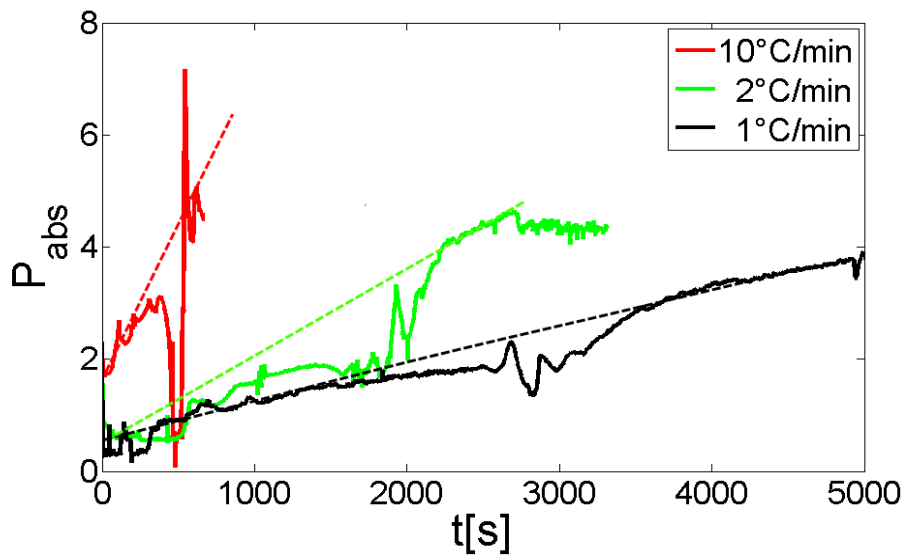


Fig. 4.1.6  
Qualitative calorimetry studies of epoxy resin during curing at different heating rates.

## 4.2 Collaboration Projects

### MACOS

The BMBF funded project MACOS (Microwave Ablation of Concrete Surface; funding code 02S8719) aims to develop a high power microwave applicator to speed up the decontamination of concrete surfaces from nuclear power plants. After some successful experimental results in microwave ablation of concrete blocks with an optimized waveguide antenna used in 2013 and 2014, a drying model based on an Arrhenius energy function and heat and mass diffusion equations has been developed. The aim was to better understand the mechanism of explosive spalling and to estimate thermal stress and pore pressure by use of COMSOL Multiphysics simulations. The model shows that the thermal stress is the dominant effect for explosive spalling and that concrete grades with higher water content result in higher power density because of a higher loss factor of the material. As a consequence, the temperature, thermal stress and pore pressure are also higher and so the probability of explosive spalling increases drastically for wet concrete. This conclusion was supported experimentally, where it was shown that the volume of ablation increase with the water content. The Fig. 4.2.2 below shows regular and controlled surface ablation of the concrete block. The total time of ablation for one block is about 150 s and the average ablation rate is about 7g/s. Surface temperature in the range of 150 to 250 °C have been measured with a thermo camera (see Fig. 4.2.2).

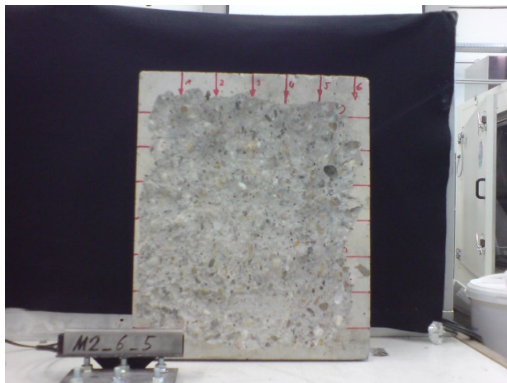


Fig. 4.2.1  
Ablation depth 2 to 3 cm with P = 10 kW

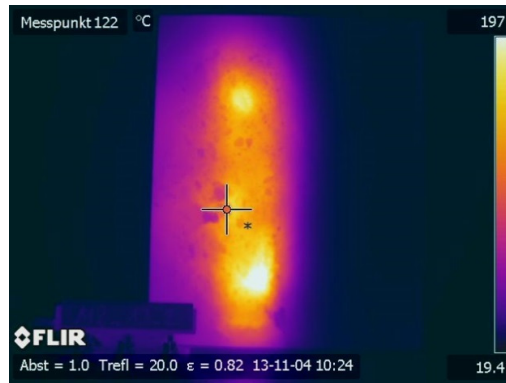


Fig. 4.2.2  
Thermo picture of the surface after ablation

## DER

In subcontract to the BMBF-fundet DER Project (Deutsches Energie und Rohstoffzentrum) which was coordinated by the TU Bergakademie Freiberg, a compact high power microwave applicator was developed. This applicator is designed for pre-heating and contactless weakening or demolition of lignite briquettes before been launched into a pressurized gasification reactor. The compact 10 kW microwave applicator as shown in Fig. 4.2.2 has been successfully designed, built and tested. The integration of a high strength silicon nitride tube with low dielectric loss allows its use at nominal pressures up to 65 bar. In order to get a certification of conformity with the pressure equipment directives "97/23/EG a" pressure tests at 325 bar, 5 times the nominal pressure had to be done. In operation, this applicator has demonstrated the volumetric heating of the briquettes and a large increase of lignite briquette friability because of thermal cracking as can be seen in Fig. 4.2.4. The weakening of lignite briquettes is beneficial for later gasification process of the briquettes. A theoretical study of the thermal stress and pore pressure has also been performed together with dielectric measurements. The dielectric permittivity of brown coal versus temperature was measured in real time during microwave heating with a recently developed apparatus based on the cavity perturbation method for a cylindrical geometry (see Chapter 4.1.3). In addition, the thermal expansion coefficient of dry lignite was measured in order to perform the multiphysics simulation necessary to compare the computed thermal stress and pore pressure.

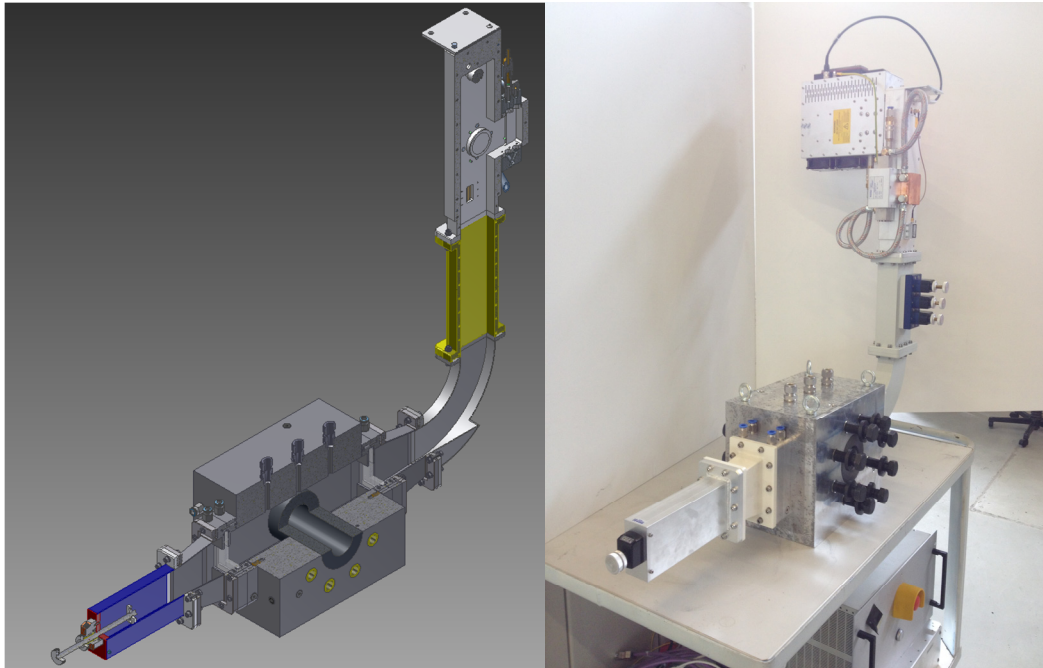


Fig. 4.2.3  
10 kW compact high pressure microwave applicator

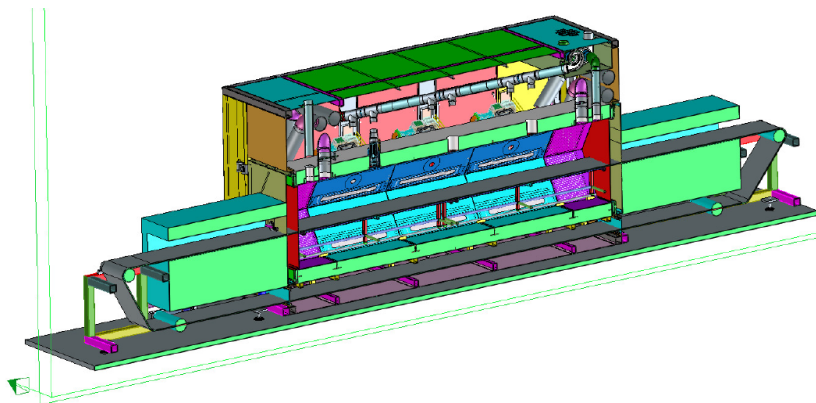


Fig. 4.2.4  
Briquette before (left) and after microwave treatment (right), both passed through a specific fall test from 2 m height.

## FLAME

The BMBF funded project FLAME (funding code 02PJ2130), which is coordinated by KIT, is about to investigate the utilization of microwave heating for the production of fiber lightweight construction with its main focus on carbon fiber composites. The purpose of the microwave is to heat and cure the resin. Due to the direct and volumetric heating there is potential to save energy and speed up the process.

One important part of this project is the enhancement of the well established HEPHAISTOS technology. That technology bases on microwave ovens developed together with the industrial partner Vötsch Industrietechnik. The microwave ovens provide a very homogeneous field distribution. A complete new HEPHAISTOS prototype that combines microwave heating with convection heating has been designed and built up (see Fig. 4.2.5). This allows combining the advantages of microwave heating and conventional heating, thereby overcoming the weakness of any pure microwave heating process that surfaces may be heated insufficiently as there is no thermal equilibrium between the workpiece and the oven walls. This oven is also equipped with a new choke at the doors that avoid microwave leakage and also with a new microwave approved multiport swivel. With this setup some sophisticated high precision winding forms of carbon fiber composite have been successfully produced. In the future this technology will be expanded to support continuous flow operation which involves the development of dedicated microwave filters for the material flow openings. The system including conveyorbelt modules is already built and brought into operation. The system will be delivered and installed at KIT in March 2015.



**Fig. 4.2.5**  
Hybrid HEPHAISTOS system-

For further enhancement of the temperature homogeneity a new high-sophisticated MPC controller has been implemented for HEPHAISTOS to replace the conventional PID controller. Compared to conventional ovens, there is no key temperature required to serve as actuating variable for the controller, at least not in the general case. Instead the input of the new controller is a temperature vector representing the complete volumetric temperature distribution. This is achieved by comprehensive in situ monitoring of the surface temperature with an IR camera. Based on adaptive online system identification algorithms and the model predictive control (MPC) principle, the new controller is able to calculate the power level of individual magnetrons of the HEPHAISTOS spatially distributed feeding system to achieve the desired temperature profile or homogeneity inside the workpiece (see Fig. 4.2.6). To allow this the existing CA3 oven has undergone a complete revision of the microwave system including a retrofit of the magnetrons and power supplies. With this setup the virtue of the new controller has been successfully demonstrated for flat 2D workpieces. Future development will include support for thicker 3D-structures.

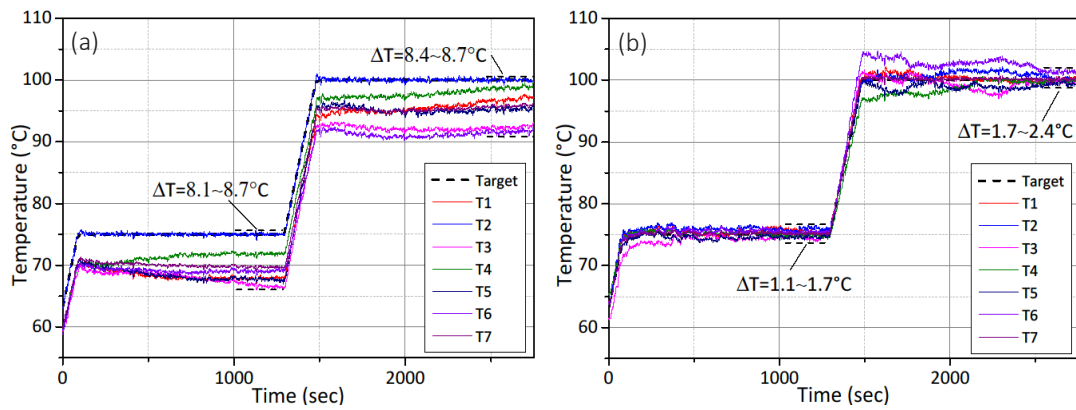


Fig. 4.2.6 Performance comparison of conventional PID (a) and new MPC (b).

## ZIM

In the frame of the Central Innovation Programm SME (ZIM) the potential of a thermosteective microwave assisted glueing of textile leather to plastic base has been investigated (funding code KF3158002CJ3). In a first approach the set of project relevant materials were characterized. Dielectric properties of different sorts of textile leather (texture, color, composition) and plastic bases (ABS, PC, PP) were investigated within process relevant temperatures 25...120 °C. First experiments in HEPHAISTOS proved the selective (predominant) heating of glue filled with carbon based susceptors and demonstrate successfully glueing of artificial leather to the base. Multiphysics models have been developed for estimation of achievable temperature gradients in dependence of applied microwave power density and the distinctive microwave absorption of the materials used.

The R & D project involves the development of a technological process for permanent and nondestructive joining of different textile or leather-like fabrics with a hard substrate material using innovative microwave technology. The innovative idea of the proposed solution is to use the potential of microwaves to directly connect top and bottom material of a workpiece with unsolvable adhesives. Therefore a primarily and selective heating of the adhesive and potentially the upper and lower surfaces of the workpieces is intended by exposure to a uniformly distributed microwave radiation. Based on preliminary investigation this can be achieved by an appropriate choice of the materials to be bonded. Therefore all potential materials for such a process need to be characterized with respect to temperature dependent dielectric properties.

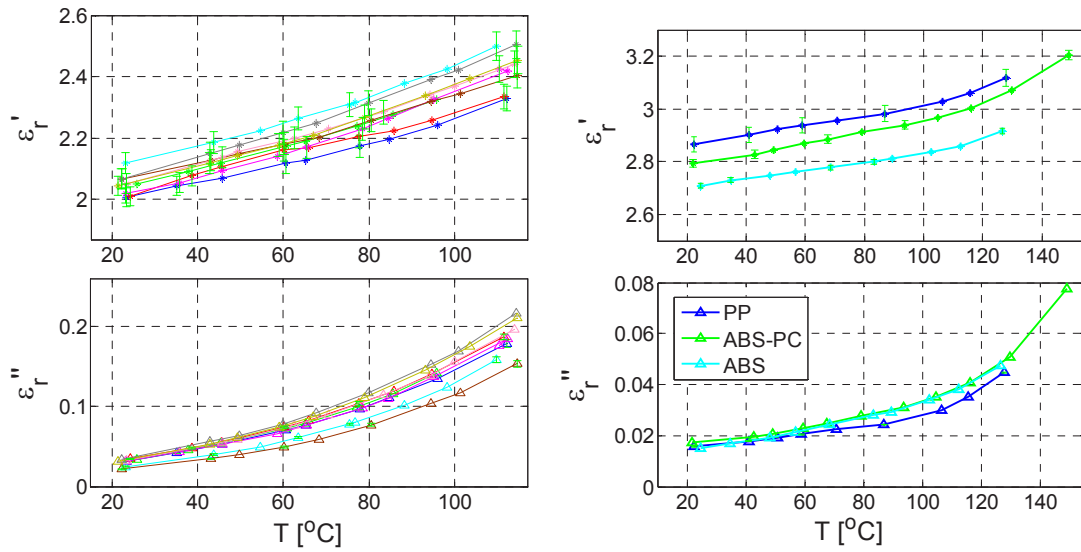


Fig. 4.2.7 Permittivities of different grades of PVC based synthetic leather (left) and different polymer blends used as substrate materials (right).

#### 4.2.1 Dielectric study on microwave assisted desorption of soil

Within the framework of an Erasmus fellowship in collaboration with the Prague University of Chemical Technology, Czech Republic, investigations on in-situ dielectric characterization during microwave desorption of moisture and organic contents in various soils were performed. This was motivated by the possibility to analyze the potential of microwave technology for such an application. Since desorption is a temperature and time dependent process, the progress of desorption and its influence on dielectric properties and microwave penetration depth, respectively can only be analysed by in-situ dielectric characterization. Therefore the test-set described in section 4.1.3, which allows dielectric measurements during dielectric heating, was utilized. Samples from different types of soil like sandy, clayey and loamy soils were prepared and characterized. Fig. 4.2.8 reveals the dielectric loss factor of sandy and clayey soil samples in different mix ratios as a function of temperature.

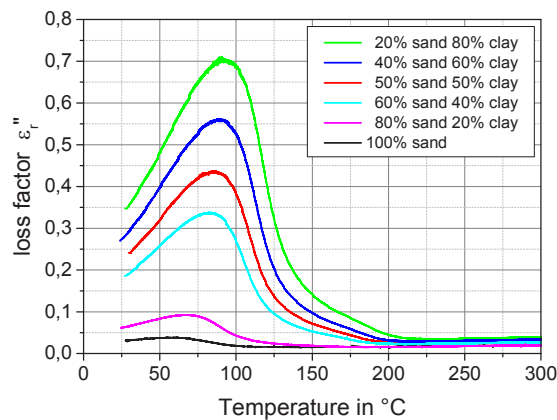


Fig. 4.2.8 Permittivity of samples with different mix ratios of sandy and clayey soil.

## 5 HGF Program: NANOMIKRO

### 5.1 Microwave synthesis and sintering of Mullite and Alumina-Mullite composites

In collaboration with the Federal University of Sao Carlos, Brazil systematic studies on microwave sintering of alumina-mullite composites were performed. Those materials are characterized by excellent chemical, physical and mechanical properties. The outcome of its low thermal expansion coefficient is high temperature stability and excellent thermal shock resistance. Therefore it is an ideal refractory material with unique properties.

This project aims to study the process of thermal synthesis of mullite and alumina-mullite composites using high frequency (30 GHz) microwave technology and compare it with results obtained by processing at 2.45 GHz. The raw materials used are kaolin and reactive alumina, which were grounded and pressed into pellets of 12 mm diameter and of 3 mm thickness. The proposed compositions are pure kaolin, which is expected to form mullite and amorphous silica, and three compositions containing kaolin and alumina, which is expected to transform into pure mullite, mullite with 10% alumina and 50% alumina. The samples are characterized for their apparent density, microstructure (SEM), phase composition using X-ray diffraction (XRD) and their mechanical strengths. Dilatometric tests at 30 GHz are made to collect data about sintering and phase transformation.

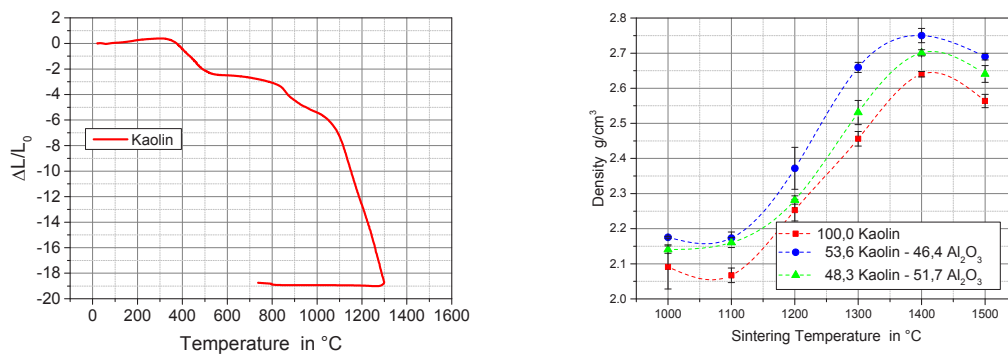


Fig. 5.1.1  
Densification behaviour of powder compacts of Kaolin, Mullite and mixed powder achieved by microwave sintering

## 5.2 Microwave sintering of Hydroxyapatite

Calcium phosphate-based biomaterials have frequently been used as bone substitutes and osteoconductive scaffolds due to their chemical similarity to the inorganic phase of bone. In addition, studies have indicated that a highly porous structure with interconnected porosity is highly desirable for bone tissue engineering applications. Hydroxyapatite (HA) is a calcium phosphate based biomaterial that could be prepared from natural sources or synthesized via several processes.

In the framework of a DAAD fellowship in collaboration with Alexandria University, Egypt systematic and comparative studies on microwave and conventional sintering of natural HA scaffolds were performed. As a result HA scaffolds sintered by microwave revealed high mechanical properties and higher porosity in a shorter processing time. In addition, the study explored the thermal, morphological and phase transition of the prepared scaffolds during sintering.

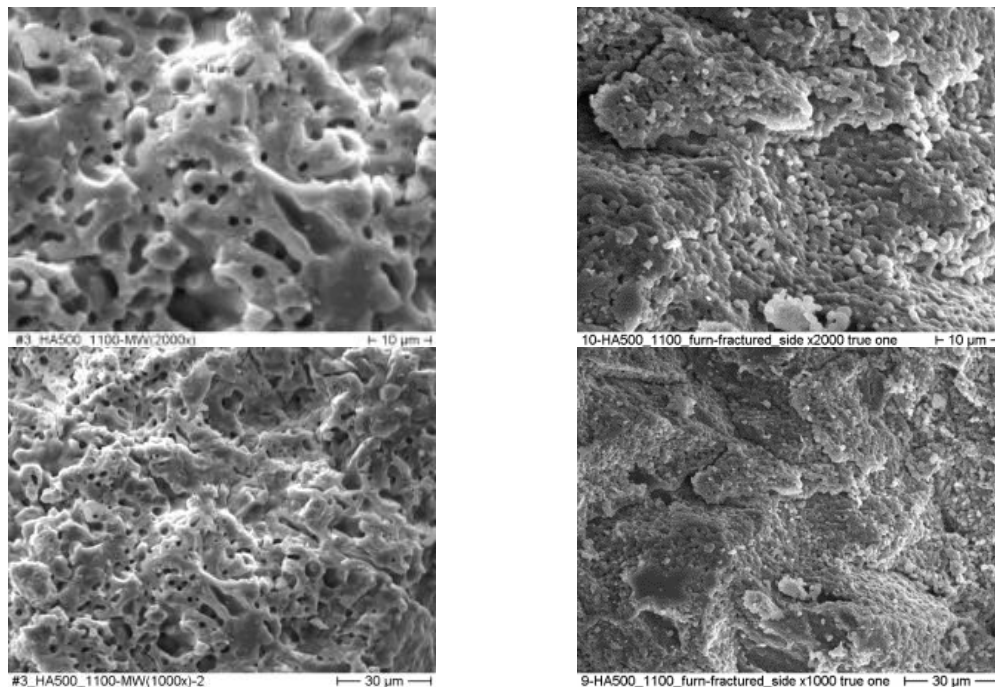


Fig. 5.2.1 SEM Micrographs for MW-30GHz sintered (left) and conventionally sintered (right) natural HA powder sample at 1100°C. Note the presence of interconnected porosity due to MW sintering which is not present in the conventionally sintered samples.

### Involved Staff:

#### KIT-IHM

K. Ayhan, Frau J. Dossinger, Prof. J. Jelonnek, Dr. T. Kayser, S. Layer, Dr. B. Lepers, **Dr. G. Link**, V. Nuss, D. Prastiyanto, V. Ramopoulos, T. Seitz, S. Soldatov, Y. Sun, Frau S. Wadle

#### KIT-IMB

Dr. M. Haist, Prof. H.S. Müller, M. Umminger

## HGF Program: FUSION

### Publications at cross-referenced journals:

I. Igitkhanov, B. Bazylev, R. Fetzner, L. Boccaccini, (2014), Effect of thermal loads on different modules of DEMO PFCs, *Fusion Science & Technology*, Vol. 66, pp. 100-105.

Y. Igitkhanov, B. Bazylev, R. Fetzner, (2014), Design Strategy for the PFC in DEMO Reactor, *Fusion Engineering and Design*.

I.E. Garkusha, V.A. Makhlay, N.N. Aksenov, B. Bazylev, I. Landman, M. Sadowski, E. Skladnik-Sadowska, (2014), Tungsten melt losses under QSPA Kh-50 plasma exposures simulating ITER ELMs and disruptions, *Fusion Science and Technology*, Vol. 65, pp. 186-193.

S. Pestchanyi, B. Bazylev, I. Landmann, (2014), Simulation of W diaphragm efficiency for mitigation of RE beam in ITER, *Journal of Nuclear Materials*.

Chr. Day, Gleason-Gonzalez, V. Hauer, Y. Igitkhanov, D. Kalupin, S. Varoutis, (2014), Towards a physics-integrated view on divertor pumping, *Fusion Engineering and Design*, Vol. 89, pp. 1505-1509.

Y. Igitkhanov, B. Bazylev, (2014), Modeling of DEMO PFC erosion due to ELM impact, *IEEE Transactions on Plasma Science*, Vol. 42, pp. 2284-2290.

S. Pestchanyi, V. Makhlay, I. Landman, (2014), Specific features of mechanism for dust production from tungsten armor under action of ELMs, *Fusion Science and Technology*, Vol. 66, pp. 150-156.

S. Pestchanyi, A. Boboc, B. Bazylev, I. Landman, (2014), Optimization of MGI in JET using TOKES code and mitigation of RE damage for the first wall, *Fusion Engineering Design*, Vol. 89, pp. 2159-2163.

J. Jelonnek, F. Albajar, S. Alberti, K. Avramidis, P. Benin, T. Bonicelli, F. Cismonti, V. Erckmann, G. Ganterbein, K. Hesck, J.-P. Hogge, S. Illy, Z.C. Ioannidis, J. Jin, H. Laqua, G.P. Latsas, F. Legrand, G. Michel, I.G. Pagonakis, B. Piosczyk, Y. Rozier, T. Rzesnicki, I. Tigelis, M. Thumm, (2014), From series production of gyrotrons for W7-X toward EU-1 MW gyrotrons for ITER, *IEEE Transactions on Plasma Science*, Vol. 42, pp. 1135-1144.

J. Jin, G. Ganteinbein, J. Jelonnek, M. Thumm, T. Rzesnicki, (2014), A new method for synthesis of beam-shaping mirrors for off-axis incident gaussian beams, *IEEE Transactions on Plasma Science*, Vol. 42, pp. 1380-1384.

O. Dumbrajs, K. Avramidis, J. Franck, J. Jelonnek, (2014), On the dependence of the efficiency of a 240 GHz high-power gyrotron on the displacement of the electron beam and on the azimuthal index, *Physics of Plasmas*, Vol. 21, pp. 013104-6.

P.C. Kalaria, M.V. Kartikeyan, M. Thumm, (2014), Design of 170 GHz, 1.5-MW conventional cavity gyrotron for plasma heating, *IEEE Transactions on Plasma Science*, Vol. 42, pp. 1522-1528.

M. Damyanova, S. Kern, S. Illy, M. Thumm, S. Sabchevski, I. Zhelyazkov, E. Vasileva, (2014), Modelling and simulation of gyrotrons for ITER, *Journal of Physics: Conference Series*, Vol. 516, pp. 012028/1-6.

M. Thumm, (2014), Recent advances in the worldwide fusion gyrotron development, *IEEE Transactions on Plasma Science*, Vol. 42, pp. 590-599.

G.S. Nusinovich, M. Thumm, M. Petelin, (2014), The gyrotron at 50: historical overview, *Journal of Infrared, Millimeter, and Terahertz Waves*, Vol. 35, pp. 325-381.

M. Thumm, A.V. Arzhannikov, V.T. Astrelin, A.V. Burdakov, I.A. Ivanov, P.V. Kalinin, I.V. Kandaurov, V.V. Kurkucheko, S.A. Kuznetsov, M.A. Makarov, K.I. Mekler, S.V. Polosatkin, S.A. Popov, V.V. Postupaev, A.F. Rovenskikh, S.L. Sinitzky, V.F. Sklyarov, V.D. Stepanov, Yu.A. Trunev, I.V. Timofeev, L.N. Vyacheslavov, (2014), Generation of high-power sub-THz waves in magnetized turbulent electron beam plasmas, *Journal of Infrared, Millimeter, and Terahertz Waves*, Vol. 35, pp. 81-90.

G. Gantenbein, A. Samartsev, G. Aiello, G. Dammertz, J. Jelonnek, M. Losert, A. Schlaich, T. Scherer, D. Strauss, M. Thumm, D. Wagner, (2014), First operation of a step-frequency tunable 1 MW gyrotron with a diamond brewster angle output window, *IEEE Transactions on Electron Devices*, Vol. 61, pp. 1806-1811.

M. Thumm, (2014), Effective cavity length of gyrotrons, *Journal of Infrared, Millimeter, and Terahertz Waves*, Vol. 35, pp. 1011-1017.

## Books

V. Girka, I. Girka, M. Thumm, "Surface flute waves in plasmas: theory and applications," *Springer Series in Atomic, Optical and Plasma Physics*, Vol. 79, 2014.

## Scientific Reports

Y. Igitkhanov, B. Bazylev, R. Fetzer, "The quantification of the key physics parameters for the DEMO fusion power reactor and analysis of the reactor relevant physics issues," in *KIT Scientific Report*, No. 7661, 2014.

J. Jelonnek, (2014), Annual Report 2013, IHM, *KIT Scientific Report*.

M. Thumm, "State-of-the-Art of high power gyro-devices and free electron masers (Update 2013)," in *KIT Scientific Report* 7662, 2014.

## HGF Program: NUSAFE

### Publications at cross-referenced journals:

A. Heinzl, A. Weisenburger, G. Müller, (2014), Corrosion behavior of austenitic steels in liquid lead bismut containing 10-6 wt% and 10-8 wt% oxygen at 400-500 oC, *Journal of Nuclear Materials*, Vol. 448, pp. 163-171.

M. DelGiaccio, A. Weisenburger, G. Müller, (2014), Freeing of fuel cladding materials for Pb cooled fast reactors -approach to long term prediction using fretting maps, *Nuclear Engineering and Design*, Vol. 280, pp. 697-703.

A. Weisenburger, L. Mansani, G. Schumacher, G. Müller, (2014), Oxygen for protective oxide scale formation on pins and structural material surfaces in lead-alloy cooled reactors, *Nuclear Engineering and Design*, Vol. 273, pp. 584-594.

M. DelGiaccio, A. Weisenburger, G. Müller, (2013), Fretting corrosion for lead alloy cooled ADS, *Journal of Nucl. Mat.*, Vol. 450, 225-236.

## HGF Program: REUN

### Publications at cross-referenced journals:

B. Lepers, Putranto, M. Umminger, G. Link, J. Jelonnek, (2014), A drying and thermoelastic model for fast microwave heating of concrete, *Frontiers in Heat and Mass Transfer*, Vol. 5, p. 41944.

## HGF Program: EE

### Publications at cross-referenced journals:

M. Rebersek, D. Miklavcic, C. Bertacchini, M. Sack, (2014), Cell membrane electroporation - Part 3: The equipment, *IEEE Electrical Insulation Magazine*, Vol. 30, pp. 8-18.

L. Wegner, (2014), Root pressure and beyond: energetically uphill water transport into xylem vessels, *The Journal of Experimental Botany*, Vol. 65, pp. 381-393.

L. Wegner, (2014), The conductance of cellular membranes at supra-physiological voltages, *Bioelectrochemistry*.

A. Silve, B. Al-Sakere, A. Ivorra, L.M. Mir, (2014), Comparison of the effects of the repetition rate between microsecond and nanosecond pulses:, *Biochimica et Biophysica Acta*, Vol. 1840, pp. 2139-2151.

T. Wetzel, J. Pacio, L. Marocco, A. Weisenburger, A. Heinzl, W. Hering, C. Schroer, G. Müller, J. Konys, R. Stieglitz, J. Fuchs, J. Knebel, C. Fazio, M. Daubner, F. Fellmoser, (2014), Liquid metal technology for concentrated solar power systems: contributions by the German research program, *AIMS Energy*, Vol. 2, pp. 89-98.

M. Leguebe, A. Silve, L.M. Mir, C. Poignard, (2014), Conducting and permeable states of cell membrane submitted to high voltage pulses: Mathematical and numerical studies validated by the experiments, *Journal of Theoretical Biology*, 360, pp.83-94.

## HGF Program: NANOMIKRO

### Publications at cross-referenced journals:

M.J. Akhtar, N.K. Tiwari, J. Devi, M. Morsi, G. Link, M. Thumm, (2014), Determination of effective constitutive properties of metal powders at 2.45 GHz for microwave processing applications, *Frequenz*, Vol. 68, pp. 69-81.

F. Paul, W. Menesklo, G. Link, X. Zhou, J. Haußelt, J.R. Binder, (2014), Impact of microwave sintering on dielectric properties of screen printed Ba<sub>0.6</sub>Sr<sub>0.4</sub>TiO<sub>3</sub> thick films, *Journal of the European Ceramic Society*, Vol. 34.



# Appendix

## Equipment, Teaching Activities and Staff

IHM is equipped with a workstation cluster and a large number of experimental installations: KEA, KEA-ZAR, three GESA machines, eight COSTA devices, one abrasion and one erosion teststand, two gyrotron test facilities with one common power supply and microwave-tight measurement chamber, one compact technology gyrotron (30 GHz, 15 kW, continuous wave (CW)), several 2.45 GHz applicators of the HEPHAISTOS series, one 0,915 GHz, 60 kW magnetron system, one 5.8 GHz, 3 kW klystron installation and a low power microwave laboratory with several vectorial network analysers.

The project FULGOR, targeting for a renewal of the KIT gyrotron teststand is progressing. In 2013, an agreement on the project structure including the involvement of the KIT project and quality management has been achieved. The final start of the procurement of the equipment is planned for 2014.

Prof. John Jelonnek has continued to teach the new lecture course entitled "High Power Microwave Technologies (Hochleistungsmikrowellentechnik)" for Master students at KIT. Prof. Georg Müller has started to teach a new lecture on "Pulsed Power Technologies and Applications" at KIT. Dr. Gerd Gantenbein has been teaching the part "heating and current drive" of the lecture "Fusionstechnologie B" by Prof. R. Stieglitz, IFRT. Dr.-Ing. Martin Sack hold the lecture course "Elektronische Systeme und EMV" at KIT.

At the turn of the year 2014/2015 the total staff with regular positions amounted to 38 (18 academic staff members, 4 engineers and 16 technical staff member and others).

In addition 10 academic staff members and 12 technical staff members (and others) were financed by acquired third party budget.

In course of 2014, 5 guest scientists, 9 PhD students (2 of KIT-Campus South, 4 of KIT-Campus North, 3 Scholarship), 3 DHBW student and 3 trainees in the mechanical and electronics workshops worked in the IHM. 8 Master students have been hosted at IHM (4 of ETIT faculty, 2 DAAD-IIT scholarship, 1 of University of Bordeaux, France). 1 Erasmus student and 1 Bachelor student has been at IHM during 2014.

## Strategical Events, Scientific Honors and Awards

Dr. Wolfgang Frey received the "Frank Reidy Award for Outstanding Achievements in Bioelectrics".

## Longlasting Co-operations with Industries, Universities and Research Institutes

- Basics of the interaction between electrical fields and cells (Bioelectrics) in the frame of the International Bioelectrics Consortium with Old Dominion University Norfolk, USA; Kumamoto University, Japan; University of Missouri Columbia, USA; Institute Gustave-Roussy and University of Paris XI, Villejuif, France; University of Toulouse, Toulouse, France, Leibniz Institute for Plasma Science and Technology, Greifswald, Germany.
- Desinfection of hospital wastewater by pulsed electric field treatment in cooperation with University of Mainz and Eisenmann AG.
- Integration of the electroporation process for sugar production with SÜDZUCKER AG.
- Development of protection against corrosion in liquid metal cooled reactor systems in the following EU-Projectes: LEADER, GETMAT, MATTER, SEARCH (Partner: CEA, ENEA, SCK-CEN, CIEMAT).
- Development of large area pulsed electron beam devices in collaboration with the Efremov Institute, St. Petersburg, Russia.
- Experiments on liquid Pb and PbBi-cooling of reactor systems with the Institute for Physics and Power Engineering (IPPE), Obninsk, Russia.
- Development, installation and test of the complete 10 MW, 140 GHz ECRH Systems for continuous wave operation at the stellarator Wendelstein W7-X in collaboration with the Max-Planck-Institute for Plasmaphysics (IPP) Greifswald and the Institute of Interfacial Process Engineering and Plasma Technology (Institut für Grenzflächenverfahrenstechnik und Plasmatechnologie, IGVP) of the University of Stuttgart.
- Development of the European ITER Gyrotrons in the frame of the European Gyrotron Consortium (EGYC) and coordinated by Fusion for Energy (F4E). The other members of the Consortium are CRPP, EPFL Lausanne, Switzerland, CNR Milano, Italy, ENEA, Frascati, Italy, HELLAS-Assoc. EURATOM (NTUA/NKUA Athens), Greece. The industrial partner is the microwave tube company Thales Electron Devices (TED) in Paris, France.
- Development of new diagnostic systems for improvement of electron guns for gyrotrons and cavity interaction calculations in collaboration with the St. Petersburg Polytechnical University, Russia and the University of Latvia, Latvia.
- Basic investigations of plasma-wall interaction in fusion reactors in collaboration with the State Research Center of Russian Federation Troitsk Institute for Innovation and Fusion Research (TRINITI), Troitsk, Russia and the Institute of Plasma Physics, Kharkov, Ukraine.
- Fundamentals of application of gyrotrons for microwave materials processing in collaboration with the National Institute for Fusion Science (NIFS) in Toki, Japan and the University of Fukui, Japan.
- Development of Microwave Systems of the HEPHAISTOS Series for materials processing with microwaves with the Company Vötsch Industrietechnik GmbH, Reiskirchen.





The Institute for Pulsed Power and Microwave Technology (Institut für Hochleistungsimpuls- und Mikrowellentechnik (IHM)) is doing research in the areas of pulsed power and high power microwave technologies. Both, research and development of high power sources as well as related applications are in the focus. Applications for pulsed power technologies are ranging from material processing to bioelectrics. High power microwave technologies are focusing on RF sources (gyrotrons) for electron cyclotron resonance heating of magnetically confined plasmas and on applications for material processing at microwave frequencies.

IHM is doing research, development, academic education, and, in collaboration with the KIT Division IMA and industrial partners, the technology transfer. IHM is part of the Helmholtz Association (HGF). During ongoing HGF POF2 period (2009 – 2014), projects are running within following six HGF programs: Renewable Energies (EE), FUSION, NUKLEAR, NANOMIKRO, Efficient Energy Conversion and Use (REUN) and Technology-Innovation and Society (TIG).

R&D work has been done in the following topics: fundamental theoretical and experimental research on the generation of intense electron beams, strong electromagnetic fields and their interaction with biomass, materials and plasmas; application of those methods in the areas of energy production through controlled thermonuclear fusion in magnetically confined plasmas, in material processing and in energy technology.